Title
Development of Nitrogen Vacancy Diamond Centers for Nanoscale Sensing of Physical and Biological Materials

Author
Lake, Michael

Publication Date
2018

Peer reviewed|Thesis/dissertation

UNIVERSITY OF CALIFORNIA

Los Angeles

Development of Nitrogen Vacancy Diamond Centers for Nanoscale Sensing of Physical and Biological Materials

A dissertation submitted in partial satisfaction
of the requirements for the degree
Doctor of Philosophy in Chemistry

by

Michael Preston Lake

2018

ABSTRACT OF THE DISSERTATION

Development of Nitrogen Vacancy Diamond Centers for Nanoscale Sensing of Physical and Biological Materials

by

Michael Preston Lake
Doctor of Philosophy in Chemistry
University of California, Los Angeles, 2018
Professor Louis-Serge Bouchard, Chair

The NV defect center in diamond forms a pseudo-atomic quantum system with discreet optically excitable transitions between ground and excited states in the gap between valence and conduction bands, making the NV center a deep-level defect center in diamond. For the negatively charged NV center (NV^-), both the ground and excited states are spin triplets (S=1) and coupling between optical and spin states provides unique opportunities for optical detection of magnetic resonance (ODMR) and quantum metrology under ambient conditions. As an atomically sized point defect that is stable in single nanodiamonds as small as a few nanometers, the NV center enables spin based imaging of temperature, electric fields, magnetic fields and mechanical strain with nanoscale spatial resolution. Made of carbon, nanodiamonds are also ideal nanoparticles for use in biological systems, exhibiting extremely low cytotoxicity, no photo bleaching and exceptional contrast in transmission electron and light microscopy. With the ability to act as both a passive, non-perturbing sensor (e.g. a diamagnetic material used for sensing magnetic fields) and a connection point for two way, direct coupling of far field optics to NV^- spins and indirectly to the highly localized neighborhood of atoms, electronic states and phonon modes in the local vicinity, NV diamond provides a route to nanoscale field sensing and spin based optical microscopy. These sensors are also stable in nanodiamonds. For nanoparticles, the reduction in particle diameter dramatically enhances the proportion of the material that is surface exposed, enhancing any surface related properties. Nitrogen Vacancy centers in nanodiamonds provide

another example of material properties that vary with particle size. In Chapter 5, evidence that modulation of nanodiamonds fluorescent emissions by electrical perturbations in their surrouding environment allows transduction of local electrodynamics into a far field optical signal capable of mapping action potentials in cardiomyocytes in presented. The unifying theme for all of the work presented in this dissertation is to enable the use of magnetic resonance signals and interactions for imaging and sensing in previously inaccessible regimes. The specific focus is on methods and techniques to enable nanoscale physical sensing and functional imaging in live tissues, with the ultimate aim to lay the predicate for the combination of both without compromise.

The dissertation of Michael Preston Lake is approved.

Dean Ho

William M. Gelbart

Louis-Serge Bouchard, Committee Chair

University of California, Los Angeles

2018

This dissertation is dedicated to my father Ralph, who's lifelong support made this opportunity possible, to my mother Janis, who's support carried me all the way through it, to my uncle, Jeff Birdwell, the eagle in my own battle of five armies, and to my wife, Erica Lake, heart of my heart and my unfaltering partner through all of these efforts.

Table of Contents

List of Figures

Acknowledgments

I woulds like to thank my advisor Louis Bouchard, who gave me (almost) all of the challenges and all of the opportunities worth getting past them. I would also like to thank all of the members of our lab, the members of the department and the broader UCLA community that made these incredible thrusts possible.

Vita

2006	B.S. Physics and Cybernetics University of California, Los Angeles
2010	M.S. Microbiology, Immunology, and Molecular Genetics University of California, Los Angeles
2013	Silver Prize Poster Session Seaborg Symposium University of California, Los Angeles
2014	M.S. Chemistry University of California, Los Angeles
2017-2018	Dissertation Year Fellowship University of California, Los Angeles
2018	Ph.D. Chemistry University of California, Los Angeles (expected)

Publications

Lake, M. P., Bouchard, L. S. "All Optical Imaging of Action Potentials in hESC Cardiomyocytes with Electrically Modulated Fluorescence from Nitrogen Vacancy Centers in Internalized Nanodiamonds" *Manuscript in Preparation for Submission* (2018)

Lake, M. P., Bouchard, L. S. "Targeted Nanodiamonds for Identification of Subcellular Protein Assemblies in Mammalian Cells." *PLoS ONE.* (2017). 12(6)

Chen J, Lourette S, Rezai K, Hoelzer T, Lake M, Nesladek M, Bouchard LS, Hemmer P, Budker D. "Optical quenching and recovery of photoconductivity in single-crystal diamond" *Appl. Phys. Lett.* 110, 011108 (2017).

Zurbuchen M.A., Lake M. P., et al. "Nanodiamond Landmarks for Subcellular Multimodal Optical and Electron Imaging." *(co-first author) Sci. Rep.* 3, Article number: 266 (2013).

Mack, J. J.; Youssef, K.; Noel, O. D. V.; Lake, M. P.; et al. "Real-Time Maps of Fluid Flow Fields in Porous Biomaterials." *Biomaterials* 34(8), 19801986. doi:10.1016/j.biomaterials.2012.11.030 (2013).

Taylor R, Alkan F, Koumoulis D, Lake M, King D, Dybowski C, Bouchard LS. "A combined NMR and DFT study of narrow gap semiconductors: The case of PbTe, J. Phys. Chem. C 117, 8959-8967 2013" *J. Mag. Res. Imaging* 34, 1822-1829 (2015).

Koumoulis, D.; Chasapis, T. C.; Taylor, R. E.; Lake, M.P. et al. "NMR Probe of Metallic States in Nanoscale Topological Insulators." *Phys. Rev. Lett.* 110, 026602 (2013).

Taylor RE, Leung B, Lake MP, Bouchard LS. "Spin-lattice relaxation in bismuth chalcogenides." *J. Phys. Chem. C* 116, 17300-17305 (2013).

Lake, M. P. "Discovery of live nipah virus inhibitors using reduced-risk surrogate assays adapted to high throughput screening." *University of California, Los Angeles* Masters Thesis, (2011).

Wang YE, Park A, Lake M, et al. "Ubiquitin-Regulated Nuclear-Cytoplasmic Trafficking of the Nipah Virus Matrix Protein Is Important for Viral Budding." *PLoS Pathog.* 6(11) (2010).

CHAPTER 1

Introduction: Theory of the NV Center in Diamond

1.1 Context of NV Centers in Research

From Pieter Zeeman's discovery of spectral line splittings due to magnetic fields, (Nobel Prize in Physics in 1902) a clear trajectory can be drawn through the development of quantum mechanics with the Stern-Gerlach experiment (Nobel Prize in Physics 1943), through Isidor Rabi's first resonant mesaurements of the magnetic fields of atomic nuclei (Nobel Prize in Physics 1944), to Norman Ramsey's separated oscillatory field method (Nobel Prize in Physics 1989) that precisely revealed the effects of external electric and magnetic fields on the hyperfine splitting in atomic spectra, enabling the hydrogen maser and atomic clocks. The continued refinement of techniques to measure and manipulate atomic spectra enabled the development of controllable quantum systems and some of the earliest quantum computing proof-of-concepts and protocols. Great interest in materials with high resolution, manipulable atomic spectra that can operate at room temperature has grown with the interest in extending these technologies out of research and into applications, especially for quantum computing, and interest in the nitrogen vacancy (NV) defect center in diamond has been increasing since the start of this century. This work does not concern quantum computing, however the research presented in this dissertation is properly contextualized by this perspective. Early reasearch into defect centers in silicon formed the basis for traditional computing, and the precisely understood, highly developed industrial infrastructure surrounding silicon that grew out of the semiconductor industry paved the way for microelectronic mechanical systems, or MEMS. As the growing quantum computing industry begins to invest heavily in improving quantum coherence and developing improved spin-photon and spin-spin interaction protocols, a new generation of diverse building blocks with exceptional performance will become available for applications beyond computing. Just as NV^- is a more developed

building block in the early quantum computing field, this research is best contextualized as contributing to a practical framework to extend the NV diamond quantum sensing protocols to imaging and sensing applications in novel environments, escpecially living cells.

The trajectory described above is mirrored in the trajectory of the research presented in this dissertation and starts with traditional traditional magnetic resonance equipment and moves in a straight line to extension of magnetic resonance sensing and imaging to the nanoscale. After a brief discussion of NV center physical properties, a laboratory experiment developed to allow undergraduates to perform optically detected magnetic resonance mesurements with NV^- centers is presented. This instructional manual gives detailed technical descriptions on the measurement and interpretation of NV^- center magnetic resonance spectra. The following two chapters detail experiments on detection of nanodiamonds using light and electron microscopy and methods for the precise placement of nanodiamonds onto specific macromolecular structures. While these experiments do not contain measurements with NV centers, the lack of methods to detect and place nanodiamonds at the nanometer scale in cells was a major barrier to translating NV based quantum sensing protocols into a living cellular environment. Additionally, visualizing the immediate environment around a nanodiamond is highly valuable for interpretation of nanoscale data in a complex environment. The last chapter details the development of NV centers in nanodiamonds as an optical reporter of local electrochemical potential in cells. Recently, substantial excitement has grown about modulation of the NV charge state into 3 stable configurations (NV^-, NV^0 and NV^+), and the implications and oportunities of the charge state with regard to spin based magnetic resonance techniques. In the last chapter, recent work is presented demonstrating that electrically driven effects, likely including charge state modulation, in NV centers in nanodiamonds function allows them to act as optical reporters of action potentials in beating of human embryonic stem cell derived cardiomyocytes, bridging the delivery and placement of nanodiamonds with a novel demonstration of funtional imaging in live tissues.

1.2 Physical Properties of NV Centers in Diamond

Diamond is a crystalline solid composed of sp^3-hybridized carbon. Within the crystal lattice, defects or color centers are either naturally occurring or can be introduced artificially. One such color center, the NV center, is the most widely characterized. The yellow coloration of natural diamonds, undesirable in jewelry, comes from nitrogen impurities, however, nitrogen can be intentionally doped into synthetically grown diamonds during high pressure high temperature (HPHT) or chemical vapor deposition (CVD) driven crystal growth. Nitrogen ions can also be doped into an existing crystal via ion implantation, a common method for doping silicon to produce semiconductors.

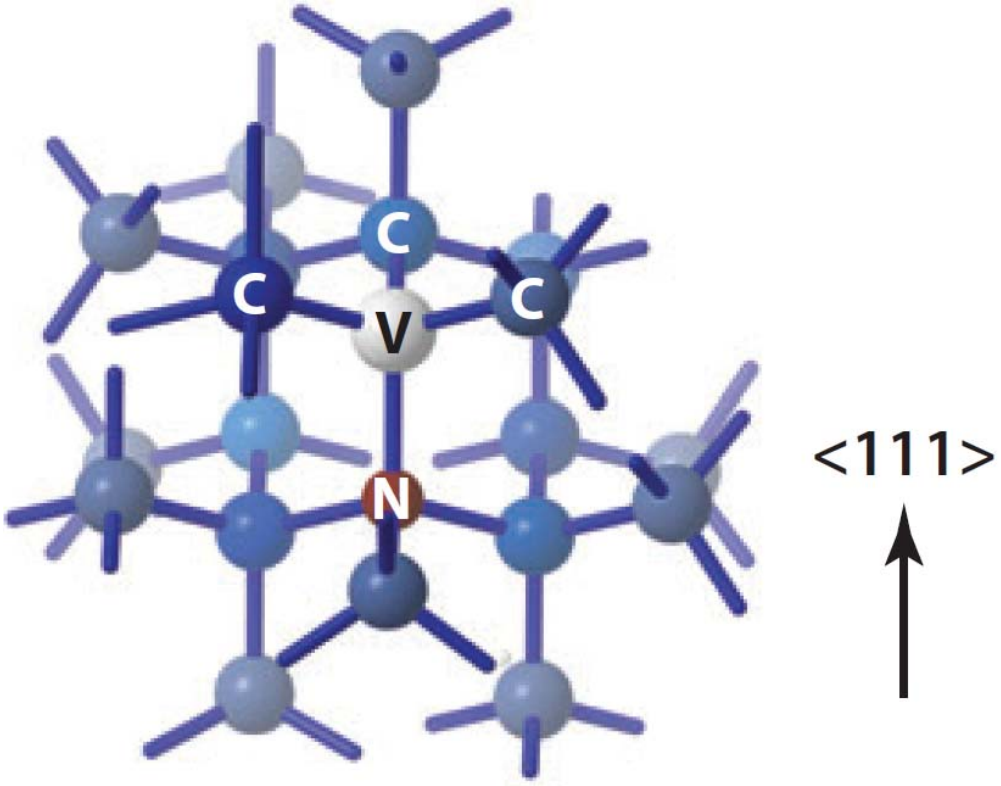

Figure 1.1: Diamond crystal lattice with nitrogen vacancy center parallel to the 111 crystallographic axis. [1]

Vacancies can be introduced into the diamond lattice to form NV centers, usually by electron irradiation to dislodge carbon atoms or as a biproduct of ion implantation. With both types of defect present (nitrogen doping + carbon vacancies), the diamond can be annealed

(600-800 °C) to cause carbon atoms to hop into vacancies, which in turn causes vacancies to migrate throughout the diamond, usually arriving at the surface, where they are effectively removed from the crystal. When nitrogen defects are present, the unpaired electrons that cannot form covalent bonds to the lattice have significantly higher potential energy, and this potential energy can be minimized if the unpaired electrons localize into a neighboring vacancy, creating a more stable configuration for both defects. This configuration remains stable during annealing. The result is shown in Figure 1.1. The NV center also attracts an extra electron donated by a neighboring N becoming N^+, to yield a nagatively-charged NV center, NV^-. This center has an optically excited state that absorbs photons with energy in the green part of the optical spectrum from 500 to 560 nm and decays by emitting deep red fluorescence around 690 nm, shown in Figure 1.2.

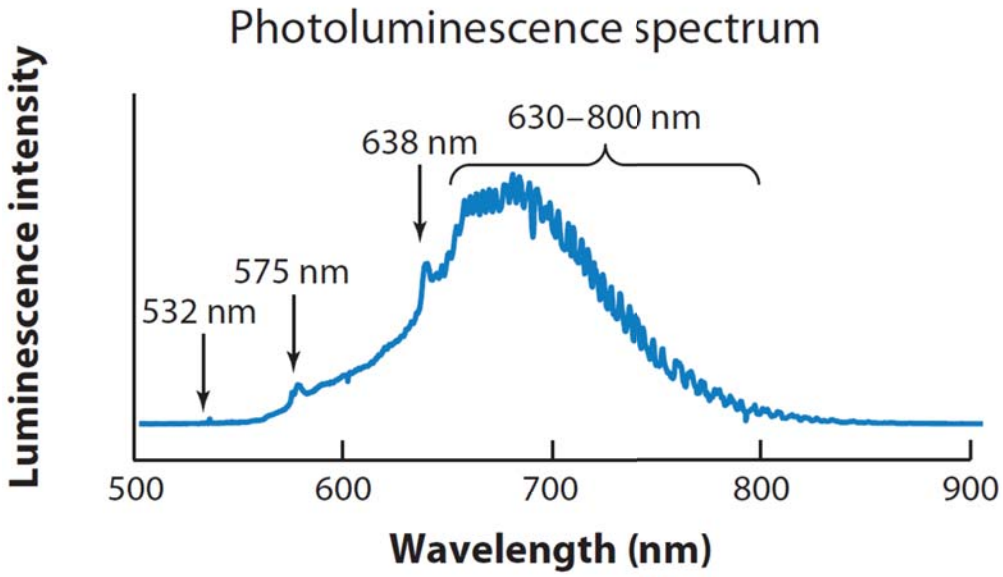

Figure 1.2: Fluorescent emission spectra from NV^- center. [1]

The two unpaired electrons in the ground electronic state of the NV^- center are in a triplet spin state (total spin angular momentum = 1). The spin projection quantum number can be $m_S = 1, 0$, or -1. In the absence of an applied magnetic field, the energy difference between the 0 state and the ± 1 states is $E = \hbar\omega_0$, with $\omega_0 = 2.87$ GHz. This energy is called zero field splitting (ZFS). This allows the spin transitions to be excited by oscillating electromagnetic fields in the microwave range.

The optical excitations ($\nu \sim 560$ THz) are spin preserving, meaning they do not alter the spin states. There is one other important electronic state involved in detecting magnetic resonance from NV$^-$ centers; the metastable singlet state labeled as $|s\rangle$ in Figure 1.3. This state represents an alternative decay pathway from the optically excited state $|e\rangle$ to the ground state $|g\rangle$ that does not emit photon radiation in the visible range. The metastable state has a singlet spin state that is limited to $m_S = 0$ only, and after decaying from this state to the ground state, $|g\rangle$, the NV$^-$ center will have $m_S = 0$.

As shown in Figure 1.3, the likelihood of a transition from the excited state, $|e\rangle$, to the metastable state, $|s\rangle$, is strongly affected by the spin state. The result is that if the NV$^-$ center has spin $m_S = 0$, there is less than a 2% chance that the electron pair will decay to the metastable state, $|s\rangle$, then to the ground state without emitting light and a 98% chance that it will decay to the ground state, $|g\rangle$, and emit a photon. In contrast, if the NV$^-$ center has $m_S = 1$ or -1, there is a 30% chance that it will decay to the metastable state and only a 70% chance of emitting a photon.

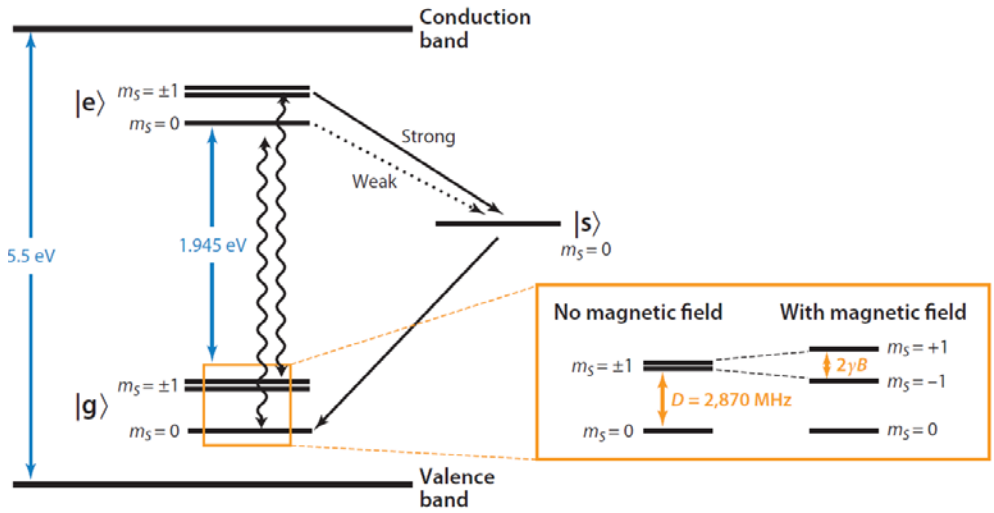

Figure 1.3: Electronic structure of NV$^-$ center. Squiggle arrows represent radiative transitions, straight arrows represent non-radiative transitions [1]

These dynamics have two important implications for observing ODESR.

Optical Pumping of the $m_S = 0$ State: At room temperature, and in thermal equilibrium, the spin state of a population of NV$^-$ centers will be found in a mixture of $m_S = 0, 1$ and -1 states. Because the spin state $m_S = 1$ or -1 increases the likelihood of transitioning to the metastable state, and the metastable state results in a spin $m_S = 0$ state, by repetitively exciting the optical transition (i.e. with a green laser), any NV$^-$ centers that were in spin $m_S = 1$ or -1 will end up in the spin $m_S = 0$ state. Any NV$^-$ center in the spin $m_S = 0$ has a 98% chance of fluorescent decay (retaining its $m_S = 0$ state, excitation and fluorescent decay are spin preserving transitions), and the 2% chance that it goes to the metastable state both result in the $m_S = 0$ state. NV$^-$ centers that originally are in the spin state $m_S = 1$ or -1 have a 70% chance of fluorescent decay (spin preserving), but a 30% chance of transitioning to the metastable state and being converted to the spin $m_s = 0$ state, so on average after a few rounds of excitation, it is likely that NV$^-$ centers originally in the spin $m_S =$1 or -1 will be converted to $m_S = 0$. This process is called optical pumping. Pumping means that the spins are initialized into the $m_S = 0$ state, preparing the NV$^-$ centers for measurement of microwave induced spin transitions. For comparison, in NMR experiments, a very strong superconducting magnet is used to polarize the spins; however, only a small fraction of spins (10^{-4}) align with the magnetic field and this small faction of the total spins are the manipulated to provide NMR and MRI measurements. In NV$^-$ diamond, we are able to polarize close to 100% of spins via optical pumping.

ODESR and Microwave Induced Spin Transitions: With all NV$^-$ spins pumped into the $m_S = 0$ state and the $m_S = 0$ state possessing 98% quantum efficiency for fluorescence output, the fluorescence output is maximized. By applying microwaves at the resonant frequency for the spin $m_S = 0$ to $m_S = 1$ or -1 transition, the NV$^-$ center will emit less light as up to 30% of the optical excitations will result in non-radiative decay through the metastable state. By sweeping the microwave frequency, we observe negative peaks (fluorescence drops) in the fluorescent signal when the microwave frequency hits resonance, allowing us to observe the electron spin resonance via fluorescence intensity.

Energy Levels of the NV$^-$ Center Spin States: The energy levels of the spin states define the frequency of microwaves that will activate the transitions of the spin state from $m_S = 0$ to $m_S = 1$ or -1. These energy levels are defined by the spin-Hamiltonian: [1] (in frequency units; multiply by Planck's constant, h, to get energy units)

$$\mathcal{H}_{spin} = \underbrace{D(S_z^2 - \frac{2}{3})}_{\text{ZFS}} + \underbrace{\gamma \mathbf{B} \cdot \mathbf{S}}_{\text{Magnetic}} + \underbrace{\epsilon_z E_z (S_z^2 - \frac{2}{3}) + \epsilon_{xy}\{E_x(S_xS_y + S_yS_x) + E_y(S_x^2 + S_y^2)\}}_{\text{Electric}} \quad (1.1)$$

where $D = 2.87$ GHz is the ZFS parameter, $\mathbf{B} = B_x\hat{x} + B_y\hat{y} + B_z\hat{z}$ is the magnetic field vector, $\mathbf{S} = S_x\hat{x} + S_y\hat{y} + S_z\hat{z}$ is the spin vector, $\mathbf{E} = E_x\hat{x} + E_y\hat{y} + E_z\hat{z}$ is the electric field vector, and ϵ_x and ϵ_y are coupling constants. The NV$^-$ center's main axis is taken to be in the $\hat{z}$ direction (Figure 1.1). From the Hamiltonian, we can calculate the energy of 3 spin states and the energy difference between them, which determines the resonance frequency of the microwaves required to cause spin state transitions from $E = h\nu$. In weak magnetic and electric fields the ZFS term dominates and the energy contribution of the spin hamiltonian ($\mathcal{H}_{spin}$) for each spin state, $|S, m_S\rangle$, becomes:

$$\begin{aligned}
m_S = -1 \quad & \mathcal{H}_{spin}\,|1,-1\rangle = D(S_z^2 - \frac{2}{3})\,|1,-1\rangle = 2.87 * \frac{1}{3}\,|1,-1\rangle = 0.957 \text{ GHz}\,|1,-1\rangle \\
m_S = 0 \quad & \mathcal{H}_{spin}\,|1,0\rangle = D(S_z^2 - \frac{2}{3})\,|1,0\rangle = 2.87 * (-\frac{2}{3})\,|1,0\rangle = -1.91 \text{ GHz}\,|1,0\rangle \\
m_S = 1 \quad & \mathcal{H}_{spin}\,|1,1\rangle = D(S_z^2 - \frac{2}{3})\,|1,1\rangle = 2.87 * \frac{1}{3}\,|1,1\rangle = 0.957 \text{ GHz}\,|1,1\rangle
\end{aligned}$$

The allowed transitions are governed by selection rules and only $\Delta m_S = \pm 1$ are allowed, resulting in the energy difference for allowed transitions from $m_S = 0$ to $m_S = 1$ or $m_S = 0$ to $m_S = -1$ as $\Delta E = h \cdot (2.87 \text{ GHz})$, where 2.87 GHz is the frequency of microwaves that will result in the correct energy for resonance, driving transitions from the $m_S = 0$ state to either $m_S = 1$ or -1.

CHAPTER 2

Optical Sensing of Temperature and Magnetic Fields with NV^- Diamond based Magnetic Resonance Spectroscopy: Chemistry 114 ODESR Student Experiment

2.1 Preface

The last equation in the introduction is the direct connection between external magnetic fields and the magnetic resonance spectrum in NV^- centers in diamond and establishes the basis for magnetometry and thermometry using NV^- centers. By optically measuring the magnetic resonance spectra and identifying the frequency of negative peaks, the external magnetic field experienced by the NV center is the directly measured. This chapter provides the student manual written to translate the DARPA funded technology our lab developed into a hands-on lab demonstration in which undergraduate students collect magnetic resonance spectra optically by measuring laser excited fluorescence emitted from a diamond using a photodetector and oscilliscope. The magnetic resonance spectra are used to measure the internal temperature of the diamond and externally applied magnetic fields. The remainder of the chapter consists of the practical instructions to students for use in the laboratory to conduct the experiment.

2.2 Optically Detected Electron Spin Resonance (ODESR): Temperature and Magnetic Field Sensing

In this experiment, optically detected electron spin resonance (ODESR) or optically detected magnetic resonance (ODMR), will be used to detect temperature changes in a diamond sample from laser excited fluorescence measurements. From these measurements the temperature dependence of the zero-field splitting (ZFS) D parameter in the spin Hamiltonian will be

determined. The ODESR spectrum will also be used to measure magnetic fields, applied with an electromagnet, and the coupling coefficient for magnetic fields will be calculated. With measurements of the magnetic field in both directions, the electric field due to crystal strain in the diamond will be estimated.

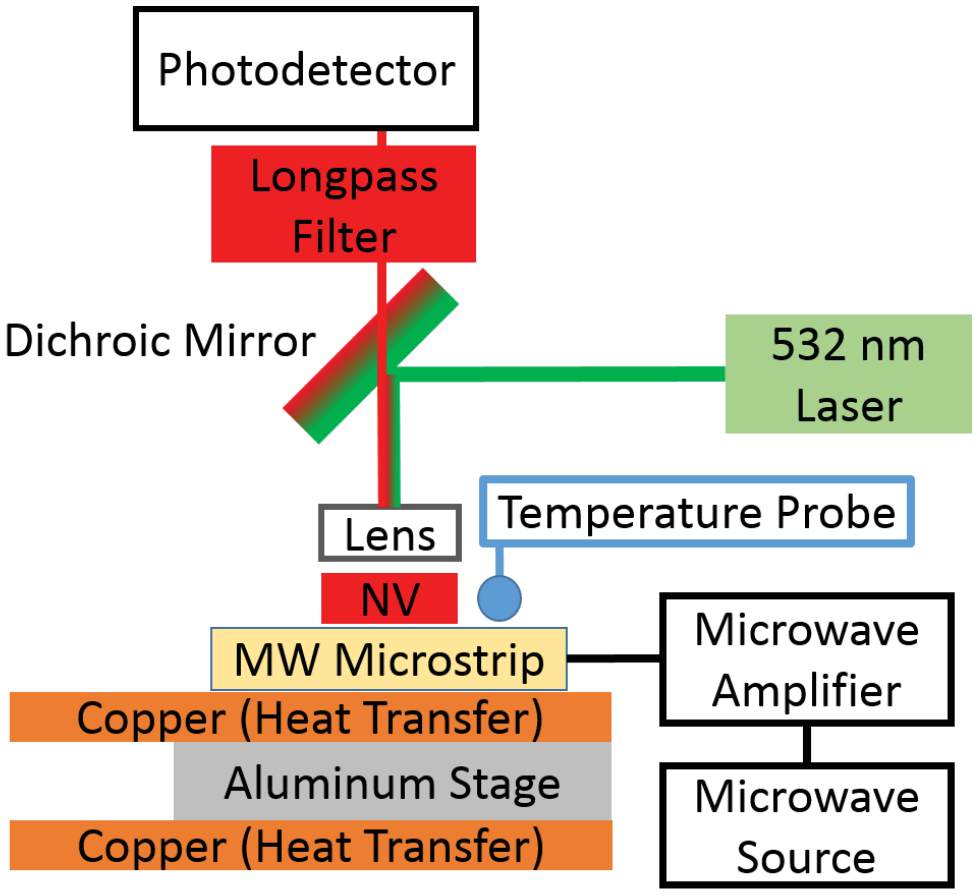

Figure 2.1: Diagram of experimental setup

2.3 Apparatus

In order to collect the ODESR spectrum, we utilize a standard fluorescence microscopy setup shown in Figure 2.1 consisting of a 532 nm laser for the excitation source, a dichroic mirror, a focusing objective, a long-pass filter and a photodetector. The dichroic (two-color) mirror reflects light with wavelengths below 605 nm and transmits light with longer wavelengths. This allows the mirror to reflect the laser light into the lens and to reflect returning laser

light back toward the laser source, while transmitting red fluorescent light through to the photodetector.

The diamond is placed under the focusing objective and on top of a microstrip, which acts as an antenna to transmit an oscillating microwave field into the diamond. This oscillating field couples to the NV^- centers spins to stimulate transitions when the resonance conditions are met. This effect is described by the rotating wave approximation. [2] This approximation states that an oscillating magnetic field can drive spin transitions when the energy provided by the oscillating field to the spin approaches the energy level of the spin transition, which is $\hbar\omega_0$, where ω_0 is the frequency of the microwave signal when on resonance.

2.4 Procedure

Instrument Settings: Turn on sample stage thermometer, laser, photodetector, microwave source, microwave amplifier, and function generator by switching on the power strip on the far right. On the function generator on the right, press the power button on the lower left of the device. Press `Store`, then `Browser` on the right of the screen so a blue light appears next to `State 1: odmr.RSF`, then press `Read` to load the settings. If necessary, load the settings on the oscilloscope by pressing `Save/Recall`, then press the top right button next to the screen labeled `action` until it reads `Recall Setup`. Ensure the next button down `Recall From` shows `Setup` and the next lower says `Setup 1`. Press the lowest button `Recall` to load the settings. **Check that the M Pos setting in the upper right of the oscilloscope screen is 1.130 s** This places the trigger at the right location in the trace and is essential for alignment of the traces with the analysis scripts.

Initial Signal Detection: Turn to the second computer on the right and click the gray button labeled `RF is Off`. It should turn red and read `RF is On`. Next, turn back to the function generator and press the `Output` button for Channel 1, which will light up green when pressed. This output acts as the timing trigger to synchronize the microwave frequency sweep and on the oscilloscope and you should see a green `Trig'd` symbol at the top of the

screen. Adjust the Channel 1 vertical position until you see the signal, which should appear as two inverted peaks and center the signal vertically, midway from the baseline to the peak minimum.

Record Traces: On the left computer, open the program on the computer desktop named Open Choice Desktop. Click "Select Instrument" in the upper left, select
USB::0x0699::0x0367::C063937::INSTR
and click OK. Turn the Fisher Scientific thermocouple on and monitor the temperature until it stabilizes around 26°C. Allow the temperature to stabilize until the change is less than 0.1°C every 2 minutes. Allow the signal to average for 12 minutes and record the temperature of the stage every 2 minutes to monitor the stability. If the temperature drift is too high, you can continue the averaging for additional two minute intervals until you have 12 minutes of averaging with stable temperature (the minimum acceptable stability is 0.1°C per 2 min, but stability of 0.1°C per 12 minutes is achievable). When the averaging time is completed, click `Select Channels` ensure only `CH1` is checked and click `Get Data`. The waveform from the oscilloscope will appear on the screen. Click `Save As` and save the file as the average temperature recorded during the measurement (i.e. `26.3`), create a new folder for your group in the subfolder for the current quarter in `C:\Users\ODMR 114 Demo\Desktop\114 Student Data` and save the data in CSV file format.

Temperature Series: Turn on hot plate and set temperature to 500°C with the orange lid and weight on the surrounding case. Monitor the temperature of the stage on the Fisher thermometer until it reaches 95°C, then turn the hotplate down to 400°C and allow it to stabilize until the temperature change is less than 0.1°C in two minutes. This should take about 20 minutes. After the temperature stabilizes, adjust the vertical position on the oscilloscope until the waveform is centered, start a timer and allow the signal to average for at least 12 minutes, recording the temperature of the stage every two minutes. When complete, turn to the OpenChoice Desktop interface and click `Get Data` (the new waveform should appear on the screen) then click `Save As` and use the average temperature during

signal averaging as the file name (i.e. `91.1`). Save as a CSV file.

Next, remove the lid from the box and adjust the temperature of the hot plate to 350°C. Replace the lid and the weight and monitor the temperature until it stabilizes to less than 0.1°C in two minutes. This stabilization should take about 15 minutes. After the temperature has stabilized, adjust the vertical position of the signal on the oscilloscope to center the waveform, start a timer and allow the signal to average for 12 minutes or more. Record the temperature every two minutes. Repeat this process for 300, 250, 200, 150, 100, and 50°C set points on the hotplate.

```
7      %INPUT DATA HERE
8
9      %%%%%%%%%%%%%%%%
10     %Enter the number of traces recorded in the series
11 -   numTraces=9;
12     %%%%%%%%%%%%%%%%
13
14 -   Trace=cell(numTraces,2);
15
16     %%%%%%%%%%%%%%%%
17     %Enter the file names for data traces from oscilliscope here
18 -   Trace{1,2}='26.4';
19 -   Trace{2,2}='37.0';
20 -   Trace{3,2}='42.0';
21 -   Trace{4,2}='47.6';
22 -   Trace{5,2}='53.3';
23 -   Trace{6,2}='66.3';
24 -   Trace{7,2}='74.9';
25 -   Trace{8,2}='82.8';
26 -   Trace{9,2}='90.5';
27     %%%%%%%%%%%%%%%%
28
29
30
31 -   for i=1:numTraces
32     %%%%%%%%%%%%%%%%
33     %Enter directory for files from oscilliscope here
34 -   filename = ['C:\Users\ODMR 114 Demo\' Trace{i,2} '.csv'];
35     %%%%%%%%%%%%%%%%
```

Figure 2.2: Regions that require user modification are shown between rows of %%%%%%

Magnetic Field Measurement: Leaving the hotplate setting at 50 °C or set the hotplate to 50 °C and wait for it to stabilize. Check the settings on channel 2 of the DG4162 Function

Generator and ensure that the period is set to 5.200 seconds, the High Limit (HighL) is set to `9.000 V` and the Low Limit (LowL) is set to `8.998 V`. Press the Output2 button (it will light up green) on the interface to turn on the positive voltage. This will apply a constant 9 V to the magnetic coil attached to channel 2 and will generate a constant magnetic field in the vertical direction. The coil is located above the lens. Adjust the oscilliscope voltage (vertical position) to center the signal on the screen and allow the signal to average for at least 12 minutes, recording the temperature every 2 min. When complete, turn to the OpenChoice Desktop interface and click `Get Data` then click `Save As` and use the voltage as the file name appended with the temperature (i.e. `9V43.1`). Repeat this for 9.25, 9.5, 9.75, and 10 V. To change the voltage, press High Limit (HighL) on channel 2 and enter `9.250 V` then press enter. Next, press Low Limit (LowL) and enter `9.248 V`, then press enter.

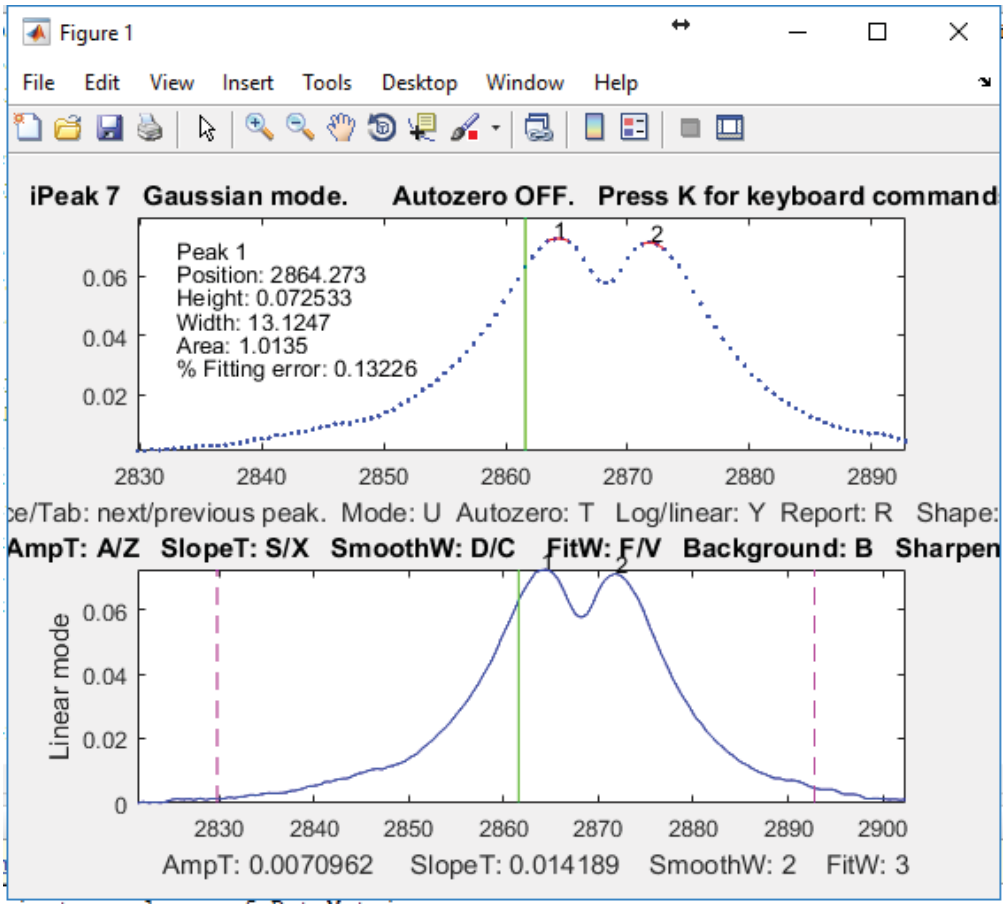

Figure 2.3: Slope adjustment in ipeak

N ext collect a series with the magnetic field reversed. First, turn the channel 2 output off by pressing the Output2 button so it is unlit. Then, change the lower voltage limit (LoLevel) to -9 V by pressing the button to the right of the LoLevel setting on the screen and then entering `-9 V` and enter. Next, change the upper voltage limit (HiLevel) to -8.998 V by pressing the button to the right of the HiLevel setting on the screen, enter `-8.998 V` and press enter. Now press the Output2 button to apply the voltage to the coil. Center the voltage trace on the oscilliscope and allow the signal to average for at least 12 minutes, recording the temperature every 2 minutes. Press `Get Data` in OpenChoice Desktop and save the file as the voltage with the average temperature appended (i.e. `-9V43.0`). Repeat this process for -9.25, -9.5, -9.75, and -10 V for a total of 10 magnetic field traces. This will allow us to calculate the gyromagnetic ratio, or γ, of the NV^- spin in the magnetic field term of the Hamiltonian.

2.5 Data Analysis

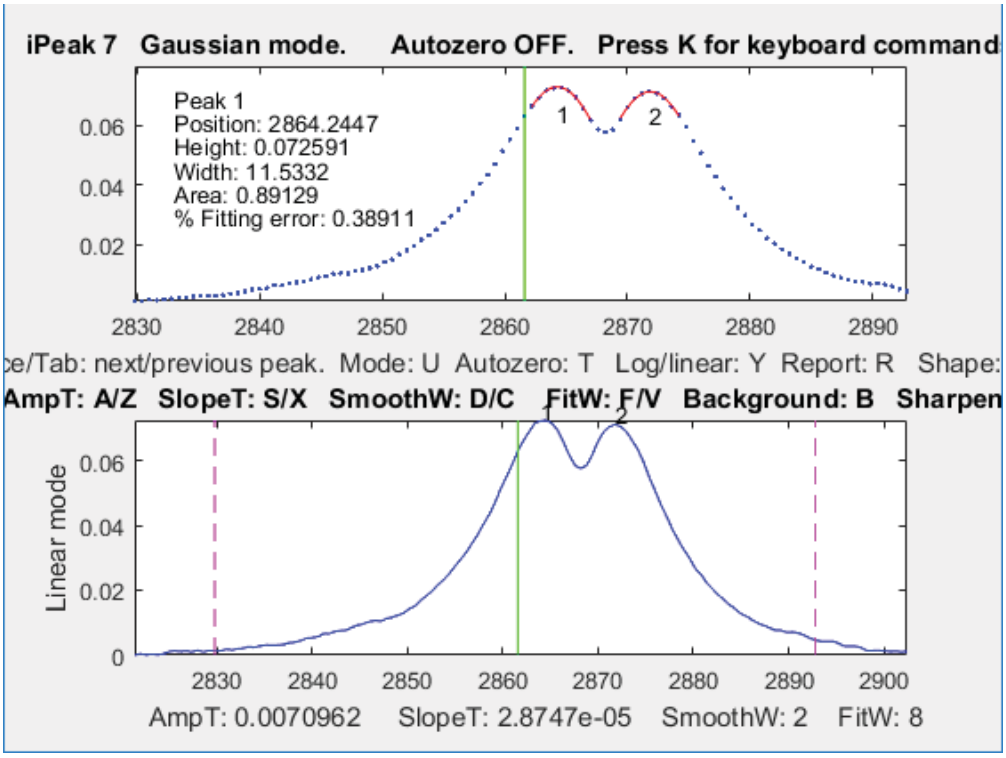

Figure 2.4: Fit width adjustment in ipeak.

Plot, Normalize and Average Traces: Open MATLAB from the Windows start menu. Open the file `ProcessTraceTemp.m` found in the folder `C:\Users\ODMR 114 Demo\Desktop\114 ODMR Analysis`. Use the `Save file as` command to save this file in your group's folder. In the analysis script, the sections that require input are surrounded by `%%%%%%` shown in Figure 2.2. Enter the number of traces that you recorded, which should ideally be 10. Scroll down to the first row where it says `Enter the file names for data traces from oscilloscope here.` In between the single quotes on each line, enter the file names for each temperature trace and the magnetic field traces. Next, enter the name of the folder where your files are located into the first array element of the filename in line 35. Press `Run` on the upper menu to execute the script, which should generate 3 figures: The raw traces, the baseline normalized traces, and the ODMR signal at each fixed frequency. Save these figures for your report. The script plots the raw traces recorded from the oscilloscope (first figure), normalizes the signal to the baseline with zero microwaves applied (second figure), then takes the values recorded for each microwave frequency step and averages them to output the ODMR signal at that frequency.

Peak Fitting for Temperature Series: To determine the center location of each individual peak, you will use ipeak, a peak analysis module written for MATLAB. Open `ipeak.m` from the `C:\Users\ODMR 114 Demo\Desktop\114 ODMR Analysis` folder. Execute the script to enable use of the ipeak function. Load the first trace for analysis using ipeak using the MATLAB command: `ipeak(MWFreq,aveODMR{1})`
This will use the values stored in the array `MWFreq` as the x axis values and the first averaged ODESR trace for fitting. After running this function, an interactive figure will open. Press 'Shift+G' to toggle the mode from Gaussian to Lorenztian peak mode. Repeatedly press the `down arrow` key to bring the full curve into view in the top window. Next, press the `x` key several times to lower the maximum slope for peaks until 1 and 2 appear above each peak.

Next, press `f` approximately 5 times to broaden the fitting width of the preliminary peak estimate (pink curve) so that the estimate extends to both sides as shown in Figure 2.4, without overlapping. To perform multiple peak fitting, press `m` and in the MATLAB

command window; a dialog box asking for peak shape will appear. Press 2 and hit enter to select a Lorentzian function as the equation to fit peaks to. For number of trials, enter 100.

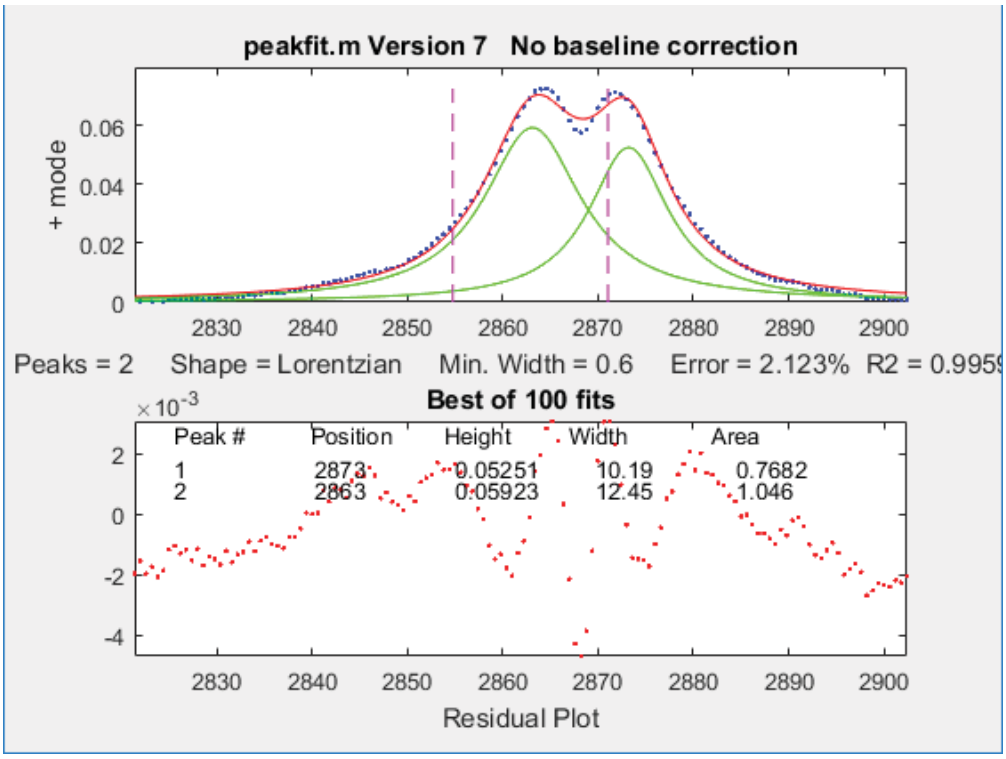

Figure 2.5: Fitting results from ipeak.

A second figure will appear showing the fitting results and the peak information will appear in the MATLAB command window. Verify that the fit is reasonable. Figure 2.5 gives an example of the expected fit. To record the peak fitting results, copy them into the TempPeakResults data structure created by the script with the command:

```
TempPeakResults{#}=P
```

where the # is the trace number used for the fitting.

Repeat this analysis for all temperature traces (ideally 1-8). The command to load each new trace into ipeak is:

```
ipeak(MWFreq,aveODMR{#})
```

where # is the trace number. Next, create 2 plots of temperature vs peak center for peaks 1 and 2. To do this, first generate the x axis of temperature values in MATLAB by defining an array of the temperature values recorded while taking the temperature traces. Do not

include the last 2 traces taken with the magnetic field on. The syntax is:

```
Temperatures=[31.0 43.5 50.3 58.1 66.3 73.7 81.3 91.1]
```

replacing these temperatures with the ones you recorded. Next, create the Y axis from the peak centers with:

```
for i=1:8; Peak1(i)=TempPeakResults{i,1}(1,2); end;
```

and

```
for i=1:8; Peak2(i)=TempPeakResults{i,1}(2,2); end;
```

Now generate a plot of the data in a new figure using the command:

```
figure; plot(Temperatures,Peak1,Temperatures,Peak2)
```

Format the figure and identify the peak data in the legend with these commands:

```
legend('Peak1','Peak2')
xlabel('Temperature ^{\circ} C')
ylabel('Microwave Frequency (GHz)')
title('Temperature vs. Microwave Frequency for m\_s=0 to -1 and m\_s=0 to 1')
```

In the new figure's Tools dropdown menu, select Basic Fitting. In the Basic Fitting window, at the top select data as Peak1 and under Plot fits check linear. Click on the arrow at the bottom of the window to display the next window and record the fitting coefficients p1, p2 and the norm of the residuals. Ensure the show equations check box is checked, and save the figure in JPEG or PNG file format.

For the second peak, in the Basic Fitting window, select Peak2 under select data, record the coefficients p1, p2 and the norm of the residuals, ensure that the show equations box is checked and then save the figure again with a different name for your report. The slope of the linear fit, the coefficient p1, gives the measured value for the temperature dependence of the ZFS term in the Hamiltonian, Equation 1.1, with units of KHz/°C. Compare the value of this parameter to the literature value. [3]

Plot, Normalize and Average Magnetic Field Traces: Open MATLAB from the Windows start menu. Open the file 'ProcessTraceMagField.m' from folder `C:\Users\ODMR`

`114 Demo\Desktop\114 ODMR Analysis`. Use the `Save file as` command to save this file in your group's folder. In the analysis script, the sections that require input are surrounded by `% % % % % % % % % %` shown in Figure 2.2. Enter the number of traces that you recorded, which should ideally be 10. Scroll down to the first row where it says `Enter the file names for data traces from oscilloscope here`. In between the single quotes on each line, enter the file names for each magnetic field trace. Next, enter the name of the folder where your files are located into the first array element of the filename in line 35. Press `Run` on the upper menu to execute the script, which schould generate 4 figures: The raw traces, the baseline normalized traces, and the ODMR signal at each fixed frequency for the negative and positive voltages. Save these figures for your report.

Peak Fitting for Magnetic Field Traces: Load the first magnetic field trace into ipeak using the command:

`ipeak(MWFreq,aveODMR{#})`

where the # is the trace taken with 9 V applied to the magnetic coil, ideally 1. In the interactive ipeak window, press the down arrow until the full curve is shown in the upper window. Press `x` several times (10-20) until the numbers 1,2,3, and 4 are shown above the 4 peaks. Reduce the smooth width to 1 by pressing `c` once. Extend the preliminary fit width by pressing `f` 8 or 9 times. Press `m` to fit the multiple peaks, followed by entering option 2 in the MATLAB command window to select Lorentzian functions, and enter `100` for the number of trials. After the fit is complete, save the peak results into the data structure MagPeakResults using the command:

`MagPeakResults{#}=P` where the # is the trace number used for fitting. Repeat this process for all of the magnetic field traces.

Analysis of Magnetic Field Traces: From the second term in the Hamiltonian (1.1), the energy contribution of the magnetic field to a given state depends on the dot product of the spin vector and the magnetic field vector. To calculate the energy of the transition from $m_s = 0$ state to either $m_s = 1$ or -1 it is necessary to know the direction of the spin

vector and the magnetic field. For the NV$^-$ spin direction, we have to remember that the NV defect is aligned in the same direction as the carbon bonds found in the diamond. Bonds between carbon atoms in diamond have sp^3 hybridization, with 4 possible orientations, each with 109.5° bond angles between them. Similarly, the NV$^-$ centers generally form equally in all 4 possible orientations. An applied magnetic field will contribute to the energy of each NV$^-$ center differently depending on its direction.

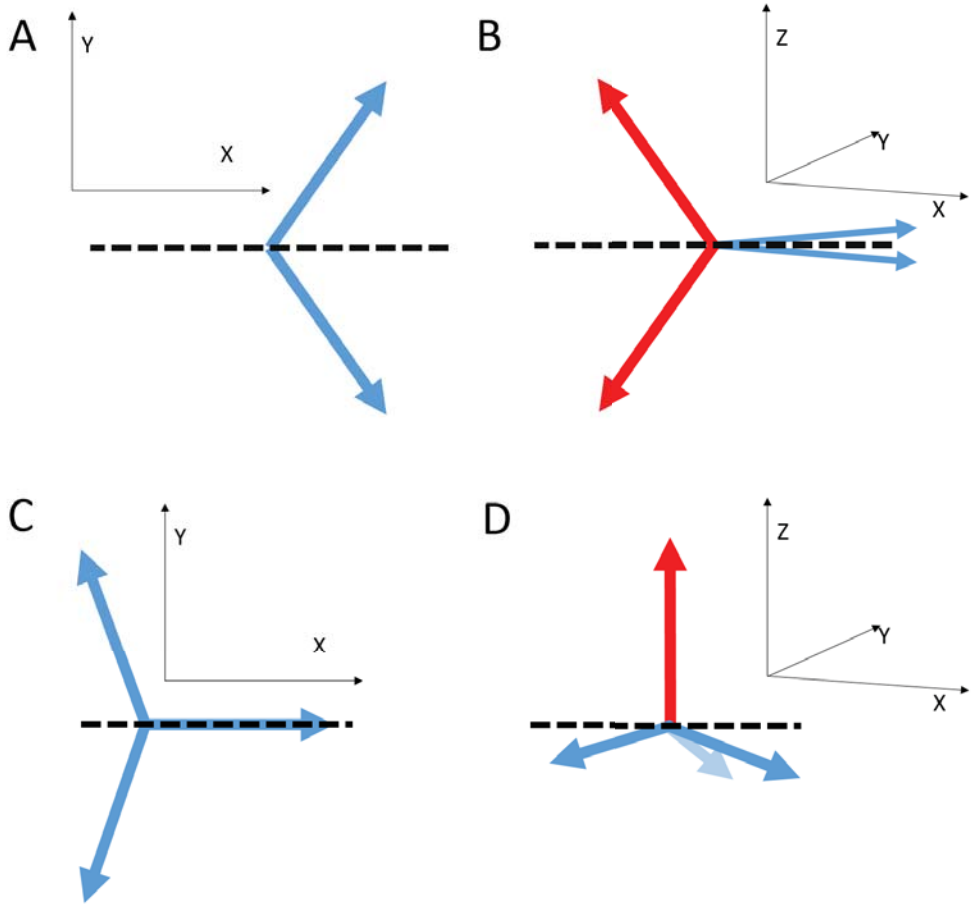

Figure 2.6: Fitting results from ipeak.

In this experiment, we are using a diamond with the crystal oriented with either the [110] or [111] plane facing up. For the [110] diamond, there are two bonds oriented in the $x-y$ plane (in the plane of the table top). The other two orientations can be found by taking the line that bisects the 109.5°angle between the first two directions and extending it as a unit vector in the opposite direction, then tilting the unit vector into the positive and negative z

direction by 54.75°, to give a 109.5° bond angle, as shown in Figure 2.6A.,B. With a magnetic field from the coil being applied in the z direction, it should be clear that we end up with 2 unique cases. The two NV^- orientations in the $x-y$ plane are perpendicular to the magnetic field, which yields a dot product of 0 and should not change the energy of the transitions. The two orientations that have some component in the z direction will have a change in the energy of the transitions, with equal magnitude and opposite directions, resulting in the same magnitude of change in the transition energy. In this experiment, changes in the transition energy appear as shifts in the resonant frequency, which shifts the peaks locations in the ODMR spectra.

The [111] crystal orientation has three fold symmetry in the $x-y$ plane as shown in Figure 2.6C. The fourth bond orientation is in the z direction, with the other three projecting into the $x-y$ plane and into the $-z$ direction, as shown in Figure 2.6D. With a magnetic field applied along the z direction, there are only two unique cases. One orientation parallel to the z axis, and three directions that form degenerate projections onto the z axis, making 109.5°angles with the z axis, resulting in the spin projection onto the z axis being scaled by $\cos(109.5°)$.

To get started on the analysis, open the file `AnalyzeMagFieldSeries.m` from folder `C:\Users\ODMR 114 Demo\Desktop\114 ODMR Analysis`. Use the `Save file as` command to save this file in your group's folder. This file will plot the absolute peak separations from the data collected in the `MagPeakResults` structure for positive currents and negative currents, as well as the peak separations relative to the peak separations from the lowest magnitude current trace (i.e. peak separations from traces taken with 9V or -9V on the function generator).

The voltage setting on the function generator can be converted to the current flowing through the coil by knowing that the equivalent circuit for the coil has a resistance of 64.5 Ohms. A positive voltage results in a magnetic field pointing in the $+z$ direction. For a solenoid, the magnetic field along by the z axis can be found by:

$$B_z = \frac{\mu_0 In}{2} R^2 \frac{r^2}{(z^2+r^2)^{\frac{3}{2}}} \tag{2.1}$$

To interpret the magnetic field measurement, it is necessary to include the direction of the NV$^-$ centers in order to determine strength of the applied magnetic field, B. B is a vector quantity, $\mathbf{B} = B_x\hat{x} + B_y\hat{y} + B_z\hat{z}$. When B is applied along the z direction, we write $\mathbf{B} = B_z\hat{z}$. This makes the dot product in the magnetic field term of equation (1.1): $\mathbf{B} \cdot \mathbf{S} = B_z S_z$. The spin vector, $\mathbf{S}$, is a vector of length $\sqrt{S(S+1)}$, where $S = 1$ is the spin (we work with spin operators expressed in units of $\hbar$). The quantum number for its z-projection can be $m_S = -1, 0, 1$. The orientation is important because the magnetic field term is $\gamma\mathbf{B} \cdot \mathbf{S}$ and the magnetic field is in the Z direction, so the z projection must be scaled according to the angle between the NV$^-$ direction in question and the z axis. For example the two NV$^-$ orientations in the [110] crystal orientation with a z component are scaled by $\sin(109.5°/2)$.

Report Questions and Calculations:

1. Compare the values of the temperature dependence of the zero field splitting parameter, $\frac{\partial D}{\partial T}$ obtained from your temperature series measurements (i.e. the slope from the linear fit) from both peaks to the literature value in reference [3]. Explain in your own words what this coefficient represents and give its units.

2. For the temperature series, calculate the distance in MHz between the two peaks (p2-p1). Calculate the average and standard deviation for the peak separations obtained from all temperature traces. What is the energy difference between the two states represented by these peaks? (value and units) What term in the Hamiltonian contributes to this energy?

3. Using equation 2.1, the calculated currents from $V = IR$, the literature value for the NV$^-$ gyromagnetic ratio [1] and your peak measurements from the magnetic field series to determine a coil characteristic constant (Q, aka "quality factor") for the coil that includes the number of turns, the distance from the coil to the diamond, and the coil geometry by solving $\Delta B = Q\Delta I$, where Q includes μ_0, n, r and z.

4. Fit the slope of the line for the peak locations from the magnetic field data vs. the current for the outermost peaks (p4-p1) and innermost peaks (p3-p2) for the positive and negative magnetic field traces. Use the literature value [1] for the gyromagnetic ratio of the NV^- center to calculate B, the magnetic field at the diamond for all voltages tested. Comparing the relative shift of the two pairs of peaks, is the data most consistent with the diamond surface having a [111] or [110] crystal orientation? Why?

5. Fit the slope of the line for the peak shifts measured for each individual peak for both the negative and positive voltage series. Use this to calculate the magnetic field strength at the diamond for each voltage and compare the values to those obtained in the previous step.

6. Notice that the positive and negative currents do not result in identical peak shifts. Compare the separation distance between the outer peaks for both each pair of positive and negative currents (i.e. traces taken at 9 and -9 V, 9.25 V and -9.25 V, etc.). Repeat this analysis for the inner peaks. Using the literature value for the gyromagnetic ratio [1] and D [3] parameter and your measured magnetic fields, calculate the contribution of the magnetic field and temperature terms to the Hamiltonian for the outer peaks of the highest current pair (10 V, -10 V). Compare this calculated value and the energy difference calculated from the ODMR spectra to solve for the contribution of the electric field parameter to the Hamiltonian for both the inner peaks and outer peaks. Explain what this value represents for the outer and inner peaks and why you would expect these values to differ.

CHAPTER 3

Nanodiamond Landmarks for Subcellular Multimodal Optical and Electron Imaging

3.1 Abstract

There is a growing need for biolabels that can be used in both optical and electron microscopies, are non-cytotoxic, and do not photobleach. Such biolabels could enable targeted nanoscale imaging of sub-cellular structures, and help to establish correlations between conjugation-delivered biomolecules and function. Here we demonstrate a sub-cellular multi-modal imaging methodology that enables localization of inert particulate probes, consisting of nanodiamonds having fluorescent nitrogen-vacancy centers. These are functionalized to target specific structures, and are observable by both optical and electron microscopies. Nanodiamonds targeted to the nuclear pore complex are rapidly localized in electron-microscopy diffraction mode to enable zooming-in to regions of interest for detailed structural investigations. Optical microscopies reveal nanodiamonds for in-vitro tracking or uptake-confirmation. The approach is general, works down to the single nanodiamond level, and can leverage the unique capabilities of nanodiamonds, such as biocompatibility, sensitive magnetometry, and gene and drug delivery.

3.2 Introduction

Nanoparticles have emerged in recent years as a promising approach to particulate labeling probes for multimodal imaging, and also for targeted drug or gene delivery. They can also be used for tracking at the single-molecule level [4]. In general, little is known about the immediate environment of targeted nanoparticles due to a lack of suitable visualization protocols. Knowledge of the local environment would enable clear delineation of relationships between the activity of a labeled agent and the local biological environment. One would like

to know, for example, the nature and proximity to adjacent macromolecular assemblies. Despite considerable investigation, the identification and optimization of such a cross-platform biomarker has remained elusive. Optical microscopy offers versatility, specificity, and sensitivity in fixed and live cell settings [5]. The development of super-resolution techniques has improved spatial resolution to tens of nanometers, but these techniques are restricted to a subset of cellular processes [6–8]. Transmission electron microscopy (TEM) offers higher spatial resolution [9]. But, it lacks reliable multimodal markers to align the field-of-view with a desired subcellular region. This is particularly true if multiple iterations between imaging techniques is desired. Routine multimodal correlated imaging, which could enable the study of live cells with concurrent visualization of ultra-structural details [10], would require the development of inert biomarkers and protocols for correlating optical and electron microscopies. Reporter systems suitable for both optical and TEM imaging are lacking. For example, fluorescent dyes and fluorophores, required for fluorescence microscopy, cannot be resolved by TEM, can be cytotoxic, and photobleach under optical excitation. Several candidate markers for multimodal imaging have been pursued, but none has yet been found to be practical and universally applicable. Gold nanoparticles and nano-gold cluster compounds are readily bio-conjugated and resolvable by TEM due to their strong electron scattering. Gold can be cytotoxic by itself, and frequently becomes isolated in lysosomes in live cells. Detergent can be used after fixation to allow penetration into cells, but penetration and immunolabeling efficiency can be low, particularly with colloidal gold, due to steric hindrance [11]. Particulate markers such as gold particles are frequently applied after cryo-slicing and thawing, after cryo-fracture, or post-embedding after slicing. That is, after cell death. These approaches have higher immunolabeling success rates, which is dependent upon particle size and whether or not a slice is embedded [11]. While the cryo-slicing approach has produced some impressive correlative imaging results [12], it is an exceptionally difficult approach, and is also not amenable to multiple iterations between imaging techniques. Last, immunogold without fluorophores can be used as a particulate marker, but for typical particle sizes, requires silver-enhancement to enlarge the particles to render them visible in optical and/or electron microscopies of slices [13]. Colloidal quantum dot (QD) biolabels are resolvable by

TEM, do not photobleach, and can be functionalized with antigen-specific antibodies for targeting. They are, however, cytotoxic, so their surfaces must be decorated with organic conjugants to provide a barrier [14]. They (QDs) also suffer from "blinking" problems [15] and are incompatible with the osmium tetroxide stain frequently used in sample preparation for TEM [14, 16]. Fluorescent nanodiamonds (NDs) have emerged as promising biomarkers. They have been used as optical labels [17], magnetic sensors [18], magnetic resonance imaging (MRI) contrast agents [19], cell division monitors [20], drug and gene delivery vectors [21–23], for single molecule tracking in live cells [24], and for nanometer-scale thermometry in living cells [25]. Fluorescence can be enhanced by implanting strongly fluorescing nitrogen vacancy (NV^-) color centers [26] to enable optical imaging. Such diamond labels are amenable to transfection into the cytoplasm [27], have surfaces that can be conjugated directly to proteins for targeting sub-cellular structures, are nontoxic to cells [28, 29] and microorganisms [30], do not photobleach or blink, and are compatible with traditional TEM stains and labels. In this Letter, we describe the use of bioconjugated NDs [9, 31] as markers for locating target cell structures. Locating ND landmarks by regular TEM is problematic due to the strong background signal originating from the amorphous fixation medium. Nanodiamonds tend to agglomerate [32, 33], reducing the bio-availability of conjugants, which tend to remain outside of cells, adhere to the outer cell membrane [34], and when taken up generally remain trapped in endosomes [34–36], all of which render them biologically inert. While the successful transfection of conjugated NDs has been reported using fluorescence microscopy, the results have not been confirmed independently [27]. To this end, lattice-resolution TEM or electron diffraction is required. Our NDs are implanted with NV^- centers and targeted using a nuclear membrane-specific localizer protocol where single NDs are transfected into the cytoplasm of live HeLa cells. After embedding and slicing, the cells are imaged by fluorescence lifetime imaging (FLIM), confocal microscopy and by TEM bright-field, lattice fringe imaging, and electron diffraction to unambiguously differentiate NDs from similar-looking features. The bright fluorescence of NDs yields excellent cellular labels. Confocal fluorescence microscopy confirms that control (untransfected) cells incubated with an excess of NDs primarily form aggregates of NDs outside cells, with occasional NDs internalized and

retained near cell surfaces, consistent with reported observations [32–36].

3.3 Results

For lower ND-concentration imaging, we turned to FLIM. DAPI serves as a positive control for lifetime imaging (Fig. 1a), where the nuclei are clearly resolved from the cytoplasm and from areas outside the cell by differential fluorescence lifetimes. The secondary peak in fluorescence is consistent with DAPI having a stronger signal and a clear peak at the expected lifetime of 2.2 ns. This peak can also be resolved into components below 1 ns and above 3 ns, representing bound and unbound DAPI, consistent with the expected emission of DAPI from two and three-photon absorption processes which both occur at 910 nm [37]. This signal dominates. Cellular auto-fluorescence, which had the strongest measured lifetimes between 1 and 3 ns, is consistent with literature values (Fig. 1b). Together these signals serve as strong positive controls for the accurate measurement of fluorescence lifetimes. Nanodiamonds exhibit an extremely short optical emission lifetime, on the order of 200 ps (Fig. 1c). The histograms of lifetimes weighted by pixel intensity show two peaks, one that corresponds to the short emission lifetime of the NDs ($\sim$250 ps), and a second that corresponds to the cellular auto-fluorescence and/or DAPI signals. The NDs in cells show the expected distribution, appearing as punctate spots with exclusion from the nucleus (Fig. 1c).

Conjugation and transfection were used to deliver NDs into living cells (in vitro), to help them escape from endosomes, and to be released into the cytoplasm. Fluorescence lifetime imaging of untransfected NDs (Figs. 2a, b) confirms the fluorescence imaging results above. Lifetime imaging of cells transfected with NDs conjugated to anti-actin antibodies using polypropylene imide (PPI) dendrimers (Fig. 2c) confirms successful transfection by the broad distribution of NDs throughout the cytoplasm, which is distinct from distributions of nanodiamonds when confined within endosomes or targeted to specific membrane-bound structures. The exclusion of signal from the nucleus is consistent with the published literature on NDs, and provides additional evidence that the NDs are responsible for the short lifetime

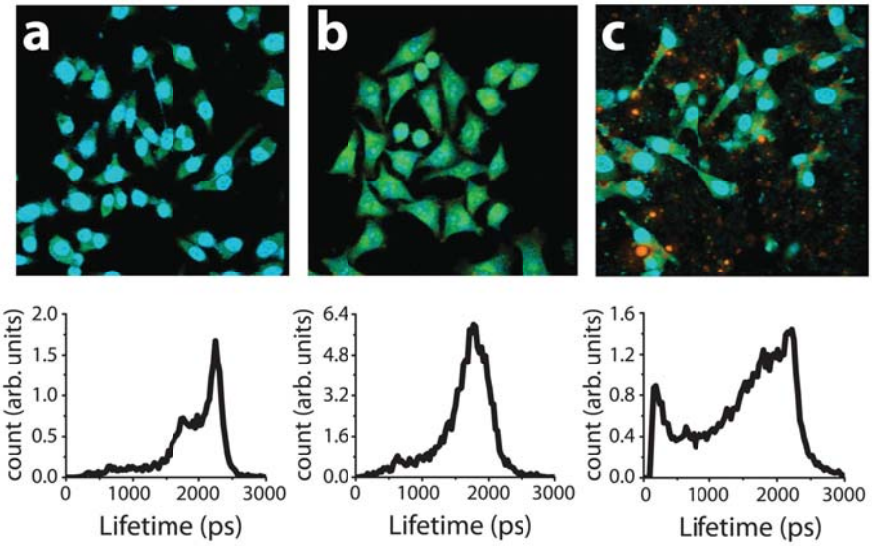

Figure 3.1: Fluorescence lifetime imaging of cells with NDs, with corresponding fluorescence lifetime spectra. (a) HeLa cells stained with DAPI. (b) Unstained HeLa cells. (c) NDs incubated with HeLa cells. Figure reproduced from Ref. [38]

component. Conjugation alone does not produce a broad cellular distribution, but PPI dendrimers significantly enhance the release of NDs into the cytoplasm (Fig. 2d), promoting enhanced targeting to cytoplasmic regions.

Imaging of individual NDs in a biological TEM specimen presents several challenges. Because our goals are to enable multiple iterations of imaging, and ultimately to perform correlated imaging, cell cultures were first embedded in epoxy resin before slicing by ultramicrotome, with slices ranging from 70 to 250 nm in thickness. The mounting resin yields a significant amorphous background that confounds TEM image interpretation, particularly for objects under 100 nm in size. A further complication is that NDs and the mounting resin have essentially identical electron densities. Together, these prevent the use of the most common methods for achieving image contrast in a nano-inclusion. That is, underfocusing the image to achieve Fresnel contrast at edges is not feasible, as contrast delocalization in the mounting medium causes a strongly modulated background that can obscure any such detail, even at very limited defocus. Second, there is no appreciable mass-thickness contrast between NDs (carbon) and the mounting medium (carbon, oxygen, nitrogen). There is also

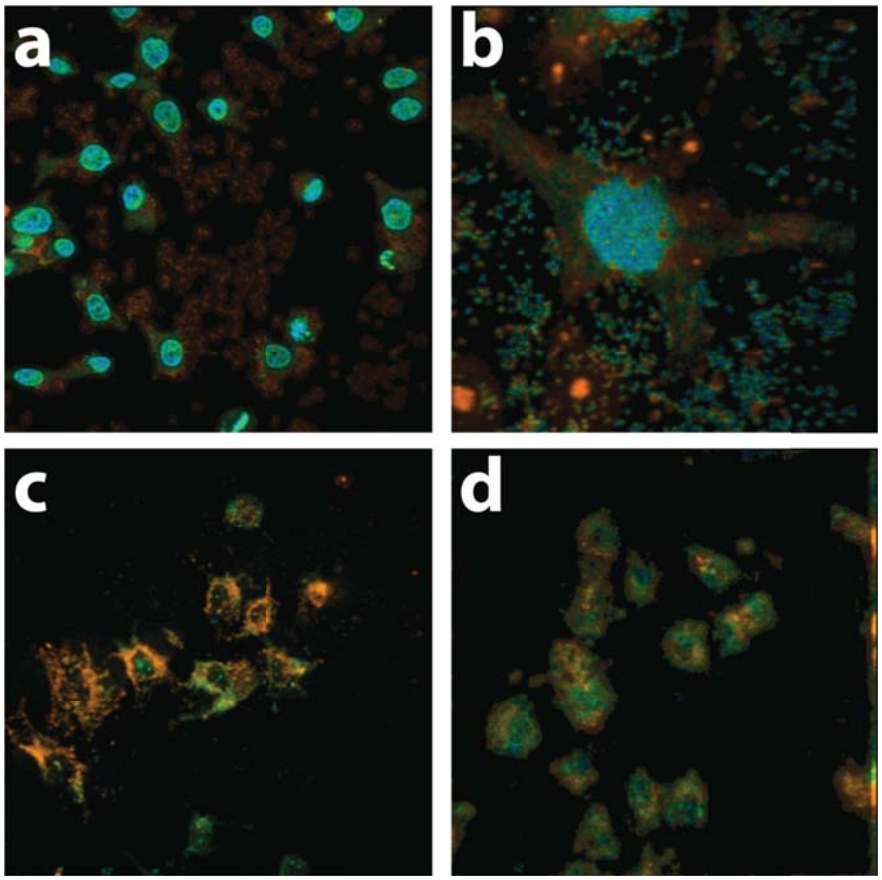

Figure 3.2: Comparison of distributions of nanodiamonds in HeLa cells by fluorescence lifetime imaging. (a) Cellular distribution observed in untransfected NDs (control) in excess concentration. (b) Magnified image of an untransfected cell showing nucleus and cytoplasm, with aggregated nanodiamonds primarily outside of cells. (c) Uniform distributions of NDs throughout the cytoplasm (no DAPI) in NDs transfected into cells with PPI dendrimers. (d) Less uniform distribution of NDs added to cells without transfection agent (brightness enhanced, no DAPI). Figure reproduced from Ref. [38]

the complicating factor that a stained sample (osmium tetroxide, uranyl acetate and lead citrate) presents significant cell-structure contrast which must be discerned from the ND landmarks.

The TEM technique was initially validated on simulated biological slices, comprising NDs dispersed in agarose gel, fixed, resin-mounted, and sliced for TEM. Our TEM observations of untransfected cells dispersed with NDs reveal the morphology and distribution reported in

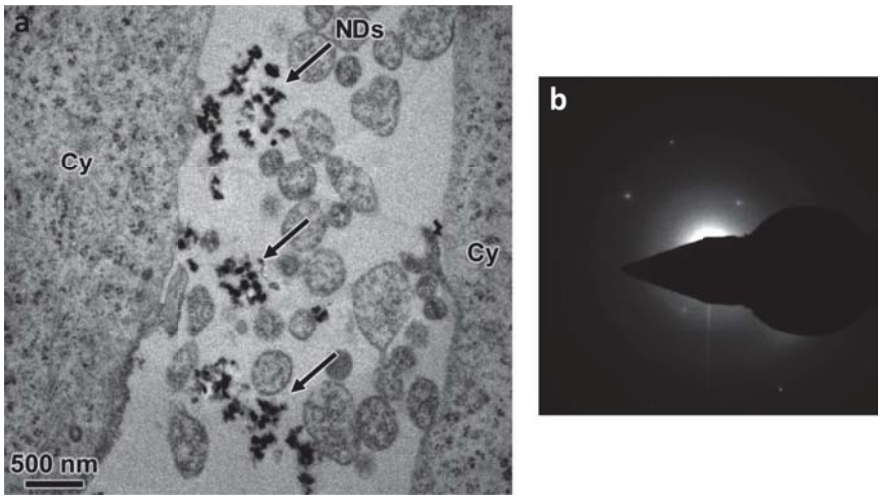

Figure 3.3: TEM characterization of a control sample reveals the typical appearance of NDs in non-transfected HeLa cells. (a) Image of several loose agglomerations of NDs in the extracellular matrix. Cytoplasm (Cy), nanodiamonds (NDs). Scale bar, 500 nm. (b) Electron diffraction pattern of the same area, confirming the agglomerations to comprise NDs. The shadow is from a pointer, used to block the central beam for image acquisition. Figure reproduced from Ref. [38]

the literature, and are consistent with our observations made by optical techniques, above. That is, the NDs are loosely agglomerated, and are almost exclusively present in the extracellular matrix (Fig. 3a). We found during this study that some dark features having the morphology of a ND particle were in fact not NDs. That is, it is necessary to confirm that any ND-like feature in fact is a ND, rather than, for example, a nanoprecipitated lead citrate agglomeration. The second approach to confirm that the dark features are indeed NDs is electron diffraction (Fig. 3b) by the ND lattice. Diffraction spots corresponding to diamond are evident over the diffuse scattering of the amorphous mounting medium. The shadow is due to a pointer used to block the primary beam from the camera, to enable acquisition of diffraction patterns with adequate dynamic range. Without this, camera bloom and oversaturation would obscure the fine details.

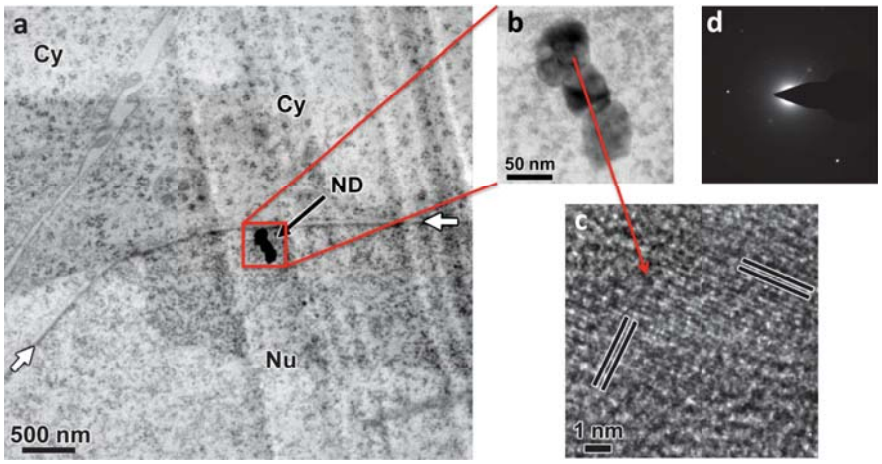

Figure 3.4: TEM verification ofNDtransfection and adherence to nuclear membrane of HeLa cells. (a) Image of a portion of a cell with a ND adhered to the nuclear membrane. White arrows indicate the nuclear membrane. Stripes are knife-marks from the ultramicrotome, and the wide, horizontal dark band is due to a slight wrinkle of the slice. Scale bar, 500 nm. (b) Magnified image of single ND (consisting of three domains). Scale Bar, 50 nm. (c) HRTEM image of the ND, showing lattice fringes (indicated by pairs of lines) which verify its crystalline character. Scale bar, 1 nm. (d) Electron diffraction pattern of the same area, further verifying that the particle is a (crystalline) ND. The shadow is from a pointer, used to block the central beam for image acquisition. Cytoplasm (Cy), Nucleus (Nu), nanodiamond (ND). Figure reproduced from Ref. [38]

3.4 Discussion

Figure 4 presents the central result of this work. Targeting of the nuclear membrane (Fig. 4a) was accomplished by a covalently conjugated antibody specific to Nup98 (Fig. 4a), which is a nucleoporin (NUP) protein normally found at the nuclear pore, embedded in the nuclear membrane. The particular ND shown in Fig. 4b is composed of three sub-grains. High-resolution transmission electron microscopy (HRTEM) (Fig. 4c) reveals lattice fringes of the crystalline diamond structure, and an electron diffraction pattern of the same ND (Fig. 4d) provides further confirmation that the landmark is a ND. This procedure yielded transfected NDs that were found to be non-agglomerated and attached to the nuclear

membrane. The results of Fig. 4 enable us to conclude that TEM can characterize the successful transfection, targeting, and localization (as a landmark or alignment fiducial) of single NDs at a region of interest. It is anticipated that this work will have a transformative effect in the biological sciences, enabling the determination of mechanistic descriptions of biological structures and dynamics. The approach was demonstrated for live-cell labeling, but is expected to be equally powerful for post-slicing labeling, whether by cryo or post-embedding. The intrinsic fluorescence of NDs having NV^- centers means that no fluorophore is needed for optical imaging of the nanoparticulate markers, so that cytotoxic fluorophores and detail-obscuring silver enhancement are unneeded. Transfected and targeted NDs could also serve as image-alignment fiducials for tomographic TEM reconstruction. Last, and perhaps most importantly, this NV^- ND approach is amenable to correlated optical and electron microscopy, perhaps even in live cell environments over multiple iterations.

3.5 Methods

Nanodiamonds, transfection reagents and conjugates The nanodiamonds used in these experiments were prepared by ball milling of larger, 100 mm diamonds containing NV^- centers and are on average, 100 nm in diameter. Conjugation of nanodiamonds to antibodies was performed by oxygen termination of the surface using strong acid treatment followed by EDC conjugation to the antibodies. Polypropylene imide dendrimers were purchased from SymoChem (Holland) and were conjugated with maltotriose to prevent cytotoxicity as described by Mkandawire et al. [27].

Cells and transfections All cells used were HeLa cells grown in DMEM with 10% FBS, 1% P/S. Transfections were performed by mixing transfection reagents with nanodiamond conjugates in HEPES buffer, or nanodiamonds alone in HEPES. Reagents were allowed to precipitate for 20 min at room temperature, followed by drop-wise addition of the solution to cells in serum-free DMEM, 1% P/S for 6 hours. Afterward, the media was replaced with growth media and cells were left to grow for 1824 hours on plastic coverslips, after which cells were fixed with 2% PFA, and some stained with DAPI. Coverslips were mounted onto

slides in 10% PBS/90% glycerol and sealed.

Fluorescence microscopy Confocal microscopy was performed on a Leica SP5- STED microscope. Excitation was done using two laser lines at 514 nm and 548 nm. Samples were bleached by repetitive scanning in order to reduce background. On this system, fluorescence can be detected using a photomultiplier tube (PMT) or avalanche photodiode (APD). Lifetime imaging was performed on a Leica SP2-FLIM microscope with Becker and Hickl SP-830 imaging hardware. Lifetime excitation was performed with infrared light from 900910 nm with a tunable TI sapphire laser.

TEM sample preparation The cell monolayers grown on coverslips were immersed in a solution of 0.1 M PBS, pH 7.4 containing 2% glutaraldehyde and 2% paraformaldehyde at room temperature for 2 hours, and then at 4 °C overnight. The cells were subsequently washed in 0.1 MPBS buffer and post-fixed in a solution of 1% OsO_4 in PBS, pH 7.27.4. Samples were then buffered in Na acetate, pH 5.5, and stained in 0.5% uranyl acetate in 0.1 MNa acetate buffer, pH 5.5, at 4°C for 12 hours. The samples were sequentially dehydrated in graded ethanol (50%, 75%, 95%, 100%) and infiltrated in mixtures of Epon 812 and ethanol (151 ratio) and 251 for two hours each time. The cells were then incubated in pure Epon 812 overnight and subsequently embedded and cured at 60°C 48 hr. Sections of 7090 nm thickness (gray interference color) were cut on an ultramicrotome (RMC MTX) using a diamond knife. The sections were deposited on carbon-film copper grids and doublestained in aqueous solutions of 8% uranyl acetate at 60°C for 25 min, and lead citrate at room temperature for 3 min prior to TEM.

TEM sample examination TEM examination was performed using an FEI Titan operated at 300 keV. Locations of regions of interest were recorded in relation to a fiducial on the copper grids, enabling location of the same area in subsequent optical microscopy experiments. Low electron beam currents, typically, 0.6 nA, along with standard low-dose imaging techniques, were employed in order to preserve specimen integrity. For very low-

magnification imaging, the FEI Titan uses the projector lenses for magnification, the optical path of which blocks many diffracted beams, rendering some NDs visible as dark spots (among real-world artifacts that may also appear dark). At moderate to high magnifications, a restrictive objective aperture is used to block all diffracted beams of the nanodiamond, rendering it dark against a relatively lighter background of the embedded cell. Tilting of an eucentric-height positioned sample was occasionally employed to achieve "twinkling" of ND particles as they moved through strongly diffracting (near-zone axis) orientations. HRTEM images were acquired as close to zero defocus as possible in order to minimize the contribution of the amorphous background, which would otherwise obscure any visible lattice fringes. Our solution to locating NDs by TEM is (1) to use a very restrictive objective aperture to block all diffracted beams from NDs, making them appear darker than surrounding material, and (2) to exploit their crystalline nature to discern them from sample-preparation artifacts. HRTEM imaging of the lattice fringes of NDs embedded in the amorphous mounting medium is feasible, but only near zero defocus of the objective lens. In the ideal case, lattice fringes in HRTEM images appear strongest at the Scherzer defocus, but due to the limited useful defocus range for cell/ND specimens, this is not possible.

CHAPTER 4

Targeted Nanodiamonds for Identification of Subcellular Protein Assemblies in Mammalian Cells

4.1 Abstract

Transmission electron microscopy (TEM) can be used to successfully determine the structures of proteins. However, such studies are typically done *ex situ* after extraction of the protein from the cellular environment. Here we describe an application for nanodiamonds as targeted intensity contrast labels in biological TEM, using the nuclear pore complex (NPC) as a model macroassembly. We demonstrate that delivery of antibody-conjugated nanodiamonds to live mammalian cells using maltotriose-conjugated polypropylenimine dendrimers results in efficient localization of nanodiamonds to the intended cellular target. We further identify signatures of nanodiamonds under TEM that allow for unambiguous identification of individual nanodiamonds from a resin-embedded, OsO_4-stained environment. This is the first demonstration of nanodiamonds as labels for nanoscale TEM-based identification of subcellular protein assemblies. These results, combined with the unique fluorescence properties and biocompatibility of nanodiamonds, represent an important step toward the use of nanodiamonds as markers for correlated optical/electron bioimaging.

4.2 Introduction

Over the past several decades, transmission electron microscopy (TEM) has allowed imaging of biological samples at the single protein level. With recent advances in electron tomography, it is now possible to resolve protein structures in cell sections with sub-nanometer resolution and field of view greater than 1 μm^2 [39]. Currently, attempts to investigate the structures of proteins in situ are hindered by the lack of suitable live cell-compatible labels to identify the protein being observed in TEM. In this study, we show that nanodiamonds (NDs) can be used

as targeted intensity contrast labels in biological TEM to image subcellular protein assemblies inside mammalian cells. Nanodiamonds were selected as TEM labels because of their wide range of favorable physical properties for biological applications. Indeed, NDs containing negatively- charged nitrogen vacancy (NV^-) defect centers yield strongly fluorescent labels [40] with emission maxima in the near-infrared [41], enabling signal detection in vivo from nonsuperficial tissues [42], and have recently been used to measure temperatures [43] and magnetic fields [44] in living cells with nanometer precision. Nanodiamonds have been used to effectively deliver drugs [45], siRNAs [46], and proteins [47, 48], and are currently being evaluated in preclinical trials for delivery of doxorubicin to brain, mammary, and liver tumors [49, 50]. Nanodiamonds are also biologically inert and display minimal or no cytotoxicity [40, 51].

In our demonstration of NDs as targeted intensity contrast labels, we have used the nuclear pore complex (NPC) as a model macro assembly. Specifically, we targeted Nup98, a 98-kilodalton nucleoporin and a component of the central nucleoporin ring structure. Nup98 localizes to both the cytoplasmic and nucleoplasmic solvent accessible faces of the NPC and has a critical role in regulating macromolecular import and mRNA export to and from the nucleus [52]. Nup98 is unique among vertebrate nucleoporins and is known to shuttle in and out of the nucleus, trafficking with mRNA to processing bodies (P-bodies) in the cytoplasm and localizing to distinct sites within the nucleus [53, 54].

To date, fluorescence microscopy has been the method of choice to determine the subcellular location of functionalized NDs in cells [55, 56]. Unfortunately, this method provides a limited view of the cellular environment immediately surrounding the fluorescent probe. However, TEM images of this cellular environment would be desirable to determine what is being measured by the ND. Existing studies of NDs using TEM have been restricted to untargeted or surface modified NDs that remain restricted to endosomes. Previous work predominantly provides isolated snapshots of NDs in cells without quantification [57], with the exception of a recent quantitative study of 150 nm NDs in endosomes [58]. To our knowledge, our TEM analysis is the first quantification of NDs with average diameter under 100 nm selectively targeted to a specific macromolecular structure and outside of endosomes. By

utilizing a TEM compatible label [59], we have been able to verify the targeting of NDs to a specific subcellular structure via direct visualization.

To unambiguously quantify the localization of antibody-conjugated NDs in mammalian cells at the nanometer scale, we have measured the location of NDs relative to a visible, uniformly sized macro assembly, the NPC. In this study, we have successfully demonstrated the use of maltotriose-conjugated polypropylenimine (PPI) dendrimers to assist in endosomal escape and delivery of NDs to the cytoplasm of HeLa cells, allowing the NDs to traffic for 12 additional hours to the intended target. The goal of this study was to determine if this delivery and targeting method would result in labeling efficiency sufficient to justify use of the NDs to locate a target of interest when visualization of the target may be ambiguous and to determine if cellular factors or the conjugated antibody would dictate the localization pattern instead. Ultimately, this method will assist in low energy, low magnification identification of the NDs, reducing the electron radiation dose on the target of interest during the location stage of TEM imaging.

4.3 Materials and Methods

4.3.1 Cell culture

The procedure for transfection, preparation of the ND conjugates, and resin embedding is described in Zurbuchen et al. [59] and Mkandawire et al. [60]. Briefly, 2 g ($5.7\text{x}10^{-5}$ mol) of 4th generation PPI dendrimers (SyMO-Chem, Netherlands), 0.92 g (1.82 mmol) and 0.24 ml (1.82 mmol) borane-pyridine complex were mixed in sodium borate buffer at 50°C, stirred continually for 7 days, purified by dialyzing against DI water for 3 days and freeze dried in a lyophilizer. The nanodiamonds were sonicated in a 3:1 mixture of concentrated HNO_3:H_2SO_4 for 24 h to enhance carboxylation of the ND surfaces.

For the conjugated NDs, an antibody raised against Nup98 (C-5), a mouse monoclonal IgG1 from Santa Cruz Biotechnology (sc-74578, Antibody Registry ID: AB_2157953), was conjugated to NDs using 1-ethyl-3-(3-dimethylaminopropyl)carbodiimide (EDC) to covalently attach free amines on the antibody directly to the carboxyl groups on the ND sur-

face. The antibody:ND ratio during conjugation was 6:1. HeLa CCL2 cells (ATCC CCL-2) [61] were grown on polylysine-treated plastic coverslips for 24 h prior to transfection. 24.3 μg Nup98 conjugated and unconjugated NDs mixed with 2.5 μl Nup98 antibodies with an average diameter of 15-20 nm prepared by ball milling were pre-mixed with 100 μg maltotriose-conjugated PPI dendrimers, incubated at room temperature for 20 min. Transfection reagents were added dropwise to cells in a 6-well dish with 2 ml Dulbecco's modified Eagle's medium (DMEM) without serum at a final concentration of 12.2 μg/ml and 50 μg/ml of ND and glycodendrimer, respectively. Cells were incubated for 6 h, the media changed to DMEM with 10% fetal bovine serum and then incubated for an additional 12 h post transfection.

4.3.2 Electron microscopy sample preparation

To obtain material for electron microscopy, materials were directly fixed in a solution containing 2% (v/v) glutaraldehyde and 2% (v/v) paraformaldehyde in 0.1 M phosphate-buffered saline (PBS) buffer (pH 7.4) for 2 h at room temperature and then incubated at 4°C overnight. Subsequently, 0.5% (w/v) tannic acid was added, and the samples were incubated for 1 h at room temperature. The tissues were then washed five times in 0.1 MPBS buffer and postfixed in a solution of 1% (w/v) OsO_4 (in PBS; pH 7.2-7.4). The combined treatment with tannic acid, glutaraldehyde, and paraformaldehyde followed by osmification enhanced the staining of membranes. The samples were washed four times in 0.1 M sodium acetate buffer (pH 5.5) and then block stained in 0.5% (w/v) uranyl acetate (in 0.1 M sodium acetate buffer, pH 5.5) for 12 h at 4°C. Subsequently, the samples were dehydrated in graded ethanol (50%, 75%, 95%, 100%, 100%, and 100%) for 10 min per step, rinsed with propylene oxide, and infiltrated in mixtures of Epon 812 and propylene oxide (1:1 and then 2:1 for 2 h each), followed by infiltration in pure Epon 812 overnight. Embedding was performed in pure Epon 812, and curing was done in an oven at 60°C for 48 h. Sections of 80-90 nm and 200 nm thickness were cut with an ultramicrotome (RMCMTX) using a diamond knife and were deposited on copper 200 mesh Quantifoil grids or single-hole grids coated with formvar and carbon, respectively. Sections were then double-stained in aqueous solutions of

8% (w/v) uranyl acetate for 25 min at 60°C and lead citrate for 3 min at room temperature.

4.3.3 Electron microscopy

Images were taken on a T20 iCorr cryo-transmission electron microscope from the FEI Tecnai G2 family. Images were taken over wide cell areas at 200 kV using selected area (SA) magnifications ranging from 3,500× to 29,000×, resulting in resolutions from 21 to 3.8 $\mathring{A}$/pixel in 2D projections. Image regions were acquired either manually with defocus ranging from -5 to - 70 μm or using automated acquisition with Fourier transform-based autofocus over wide areas to obtain unbiased information from each sample. Images were collected on a 2048×2048 electron camera with 16-bit intensity resolution.

4.3.4 Image analysis

To assess ND localization statistically, 25 images from the targeted sample and 25 images from the untargeted control sample were selected to be faithful representations of the larger set of images, but without regard to ND quantity or distribution. Each set of 25 images was manually scored to determine edge-to-edge distances from individual ND to individual NPC for all NDs. We processed the images by applying contrast thresholds, morphology-based gradient filtering, and image arithmetic operations as indicated to enhance identification of NDs during the scoring using the Icy bioimage informatics platform [62]. Zoomed images of ROIs were enlarged 10-fold using a bilinear algorithm post-processing for publication.

4.4 Results

4.4.1 Conjugation of PPI dendrimers

To assess the effectiveness of antibody-conjugated NDs as labels in a cellular landscape, we have evaluated the spatial pattern of NDs twelve (12) hours after transfection into living cells relative to that of a specific, independently identifiable macromolecular assembly, the NPC. Maltotriose conjugated PPI dendrimers were mixed with NDs prior to transfection to

aid in delivery and endosomal escape. Maltotriose conjugation was verified using ^{13}C and ^{1}H NMR spectroscopy, and the results were consistent with previously published spectra and descriptions (see S1 Fig, supplementary information) [63, 64]. Quantitative comparison of NMR peaks from the ^{13}C spectrum indicates 83% conjugation of PPI dendrimer free amines ($-H_2C-NH_2$) with maltotriose (H_2C-NH_2-R, R = maltotriose).

4.4.2 ND-Nup98 antibody conjugates localize to the NPC

To target NDs to Nup98, anti-Nup98 antibodies were conjugated directly to the surfaces of NDs, and the conjugates were then delivered into the cytoplasm of HeLa cells via transfection with 32-branch PPI glycodendrimers to aid in endosomal escape. Twelve (12) hours after transfection, the cells were fixed and processed by standard resin embedding, stained with heavy metals including OsO_4 which predominantly binds to membrane regions including the nuclear envelope, and sectioned into ultra-thin slices of 90 nm. Fig 1c shows a higher magnification (29,000×, 3.8 $\mathring{A}$/pixel) 2D projection image of a NPC obtained from this preparation revealing the internal structural features including the cytoplasmic ring, the inner ring, the nuclear ring, and the nuclear basket. These features correspond to a recently published structure of the NPC [65] from HeLa cells (Fig 1a) and verify the image scale. A large number of nuclear pores are easily identified in thin sections at magnifications as low as 3400x and appear as clear gaps in the nuclear envelope staining or as visible structures matching the well-defined dimensions of the NPC. Using these features and the ability to detect NDs with high sensitivity, we generated a distribution of the minimum edge-to-edge distances observed from projection images between each ND and the nearest nuclear pore using representative images from the antibody-conjugated sample (targeted) and the unconjugated sample (untargeted) (Fig 2). The experiment was performed from ND conjugation through EM sample preparation 2 times independently and with 3 concentrations of both conjugated and control NDs. Due to lack of saturation at the highest concentration of NDs tested, we selected the highest concentration tested for quantitative analysis. We selected twenty-five (25) representative images from both conjugated and unconjugated (control) ND samples from over 100 images acquired for each sample and scored them manually to determine the

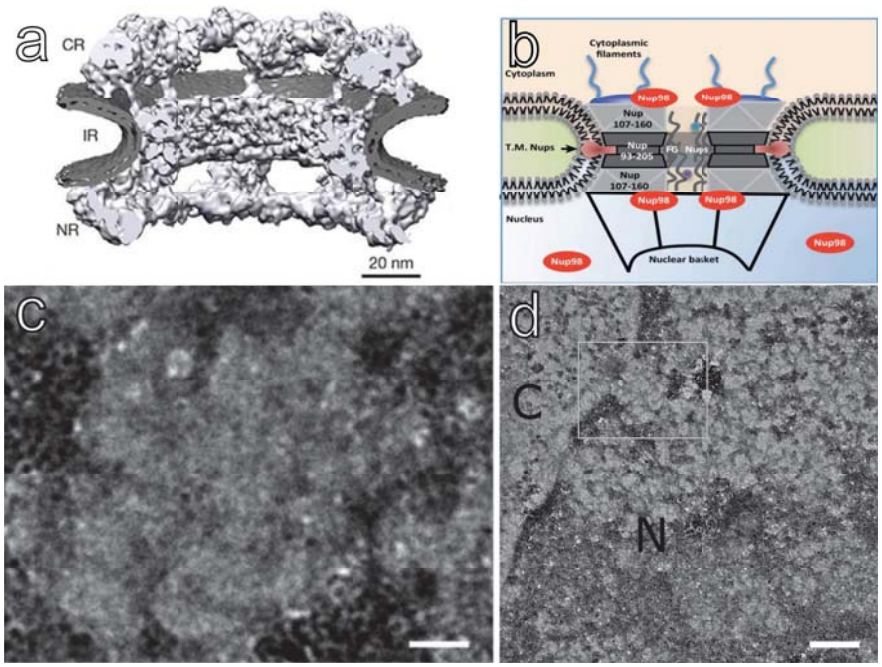

Figure 4.1: Nup98 and the NPC as a target for NDs. (a) In situ structure of human nuclear pore from isolated intact HeLa nuclei. Reproduced from Ref. [65] with permission. (b) Location of Nup98 within the NPC showing that Nup98 can localize in the central channel on both sides of the nuclear pore and outside, where it helps anchor the NPC to the nuclear envelope. Reproduced from Ref. [53] with permission. (c) High magnification (3.8 $\AA$/pixel) TEM image of human nuclear pore in 90 nm epoxy resin slice from HeLa cells showing structural details including the cytoplasmic ring, internal ring, nuclear ring and basket. Scale bar, 20 nm, rotated. (d) Wide area view of the NPC in (c), scale bar 100 nm, no rotation. C and N designate cytoplasmic and nuclear regions. Figure reproduced from Ref. [66].

distribution of edge-to-edge distances. Image selection was blind to the position of any image inside of the larger image set. Automatic focus and image acquisition over pristine, random areas was used to collect images without bias, with prescreening only to identify areas that contained cells. To construct a binary statistic, we categorized NDs within 7.5 nm of either side of the pore as bound to account for the size of an antibody and the location of Nup98 at the edge of the NPC, represented by the central bins in Fig 2, panels (g) and (h). Using this criterion to define the bound fraction, 31.0 percent of all intracellular anti-Nup98 conjugated NDs or clusters were bound to a NPC, compared with 1.26 percent for unconjugated ND or

clusters. ND counts per cluster had a mean $\mu = 9.4$ and a standard deviation $\sigma = 11$ for the targeted NDs and mean $\mu = 7.5$ and standard deviation $\sigma = 6.3$ for the untargeted NDs. These values were consistent across several counts. We also analyzed the images with a different binary statistic by defining each NPC as labeled or unlabeled using the same distance criteria (within 7.5 nm), resulting in 32/89 or 36.0% NPCs labeled by NDs in the targeted set and 3/93 or 3.2% NPCs labeled in the untargeted set. Treating the probability of an NPC being bound to a ND as a Poisson statistic, we then performed a test of the null hypothesis that these counts were generated by the same underlying probability of success for unequal sample size as described by Shiue and Bain [67]. Briefly, for two Poisson distributions X $\sim$ POI(λ_1=$s_1 \times \gamma_1$) and Y $\sim$ POI(λ_2=$s_2 \times \gamma_2$), where s is the total number of observations and γ is the probability of success, the conditional distribution of Y, given the counts observed are Y = y and (X + Y) = x + y = m, is a binomial distribution with parameters m and p or (Y — x + y = m) $\sim$ Bin (m,p) where p = $s_2/(s_1+s_2)$. This conditional distribution provides a universally most powerful unbiased (UMPU) test of the hypothesis H_0: γ_1=γ_2 against the alternative H_a: γ_2 γ_1 at the level of 1 Bin(y-1; m,p). To use this test, we observe y = 32 (targeted), x = 3 (untargeted), x + y = 35 and determined that 1-Bin(31; 35, 89/182) = 1.1×10^{-7}, or 1 the cumulative probability that y $\leq$ 32, allowing us to reject the null hypothesis for any alpha $\leq 1.1\times10^{-7}$. Similar analysis taking the counts of central bin of the above histograms as successes in a Poisson distribution gives y = 49, x = 3, and x + y = 52 yielding 1-Bin(48; 53, 158/397) = 1.5×10^{-14}.

Comparing the untargeted data to a normal distribution using a chi-square goodness-of-fit test we determined a p-value of 0.027, which indicates a reasonable deviation from a normal distribution, especially considering that this includes both cytoplasmic and nuclear distances in the same distribution. Assessing the targeted data set by excluding the central bin and assessing all remaining values using the same test, we obtain a p-value of .17, indicating that the distance from nuclear pores of the unbound fraction of targeted diamonds are close to normally distributed. Due to manual identification of nuclear pores it is possible that the closest NPC is not detected, however identification of the nuclear envelope is unambiguous in all images and given the high density of nuclear pores found on the nuclear envelope

compared to the distances being measured, an error in identification would only slightly alter the distributions presented.

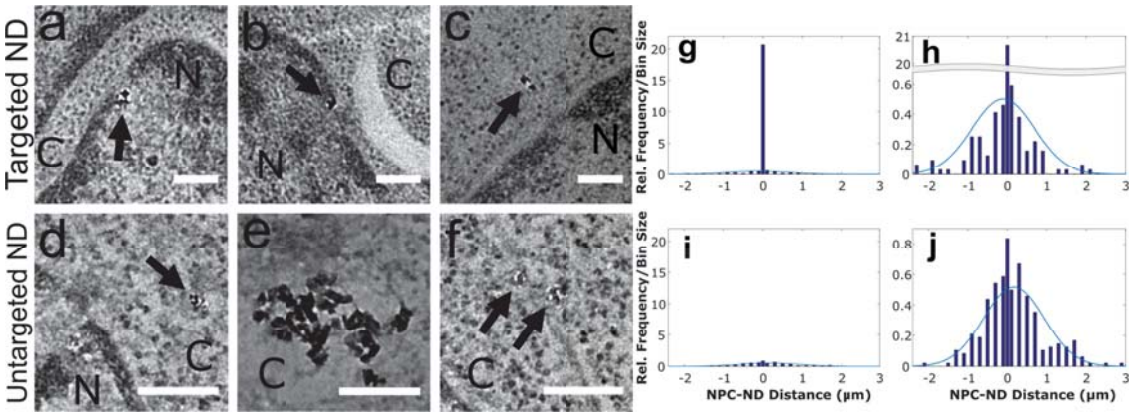

Figure 4.2: Successful targeting of NDs to the NPC. (a-f) Representative images of anti-Nup98-conjugated NDs (a, b) bound to or (c) located near an NPC, and (d-f) unconjugated NDs. C and N designate cytoplasmic and nuclear regions. Scale bar, 125 nm. Black arrows point to NDs. (g,i) Histograms of edge to- edge distances from each ND or cluster to the nearest nuclear pore for anti-Nup98-conjugated (g) and unconjugated NDs (i). Central bin counts as a percentage of the total NDs counted are 31.0% and 1.26% for (g) and (i), respectively. (h,j) Rescaled data from (g) and (i). Negative and positive values refer to distances into the nucleus and cytoplasm, respectively. We analyzed twenty-five (25) representative images from both the conjugated and unconjugated TEM samples and identified 158 and 239 NDs or ND clusters, respectively, including approximately 1,000 intracellular NDs for both sets. Minimum distance (bin 0) was defined as ± 7.5 nm to account for antibody length. The center 3 bin edges are: -200, -7.5, 7.5, 200, and all others increment by 200 nm. The blue curve is a normal distribution based on the mean and standard deviation of the targeted NDs not bound to the NPC and the untargeted NDs, respectively. Figure reproduced from Ref. [66]

4.4.3 Anti-Nup98-conjugated NDs as markers for the nuclear pore

Anti-Nup98-conjugated NDs bind to the NPC in a manner that reflects the expected localization pattern of Nup98 (Fig 3a-3e). The NDs tend to appear in clusters centered in the pore or off-center, consistent with having been dislodged and left at the edge of the NPC on either side of the membrane, possibly due to interference by endogenous molecular traffic. Considering that the NDs in this study have a size (∼20 nm) smaller than the NPC central channel (∼60 nm) [65], aggregates of NDs within the pore are not unexpected. Nup98 is known to localize to other cellular structures, and thus the calculated percentage of conjugated NDs localized at the NPC (31.0%) likely represents a lower bound for the targeting efficiency of anti-Nup98-conjugated NDs. Consistent with this, we observed strong localization of NDs to additional distinct structures. Identifying and properly quantifying binding to these other structures is hindered by lack of positive identification, however, and will be the subject of future investigations. Fidelity of the ND conjugates for Nup98 overall appears significantly higher than the percentage reported bound to NPCs, but can only be qualitatively assessed by observation at this time. It is known that Nup98 localizes to multiple subcellular assemblies such as P-bodies and intranuclear bodies however, these structures cannot be unambiguously identified in our TEM images. Most ND localization studies with larger NDs do not observe ND entry into the nucleus. This claim is not consistent with our observations with ∼20 nm NDs for either targeted or untargeted NDs in this study. However, our study was not intended to analyze this characteristic and future systematic studies of this observation coupled with additional measurements should be more conclusive. It has been observed that 4 nm gold particles modified with both poly (ethylene glycol) [68] and polyethylenimine [69] and 70 nm SiO_2 nanoparticles [70] form aggregates in the nucleus, emphasizing the importance of further research on the ability of NDs to enter the nucleus.

4.4.4 Isolating NDs from cellular background

To further assess the utility of NDs as TEM landmarks, we evaluated the intensity profile of NDs in transmission electron images. We found that the NDs are clearly distinguished

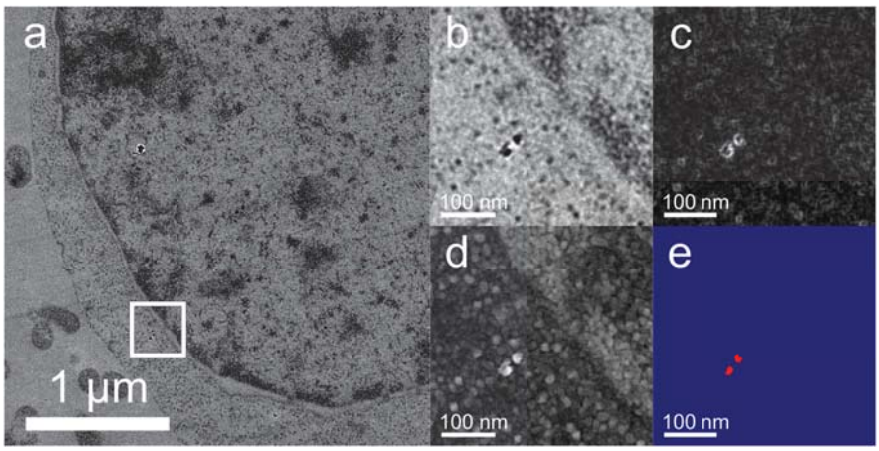

Figure 4.3: Nanodiamonds can be detected individually from low magnification (5,000×) images. (a) Original image. (b) Zoom of ROI from (a). (c) Gradient morphometry enhancement of (b). (d) Contrast inverted image of (b). (e) Inverted and gradient images summed with threshold applied to isolate diamond. Red and blue indicate saturated maximum and minimum intensities, respectively, resulting in a binary colored image. Figure reproduced from Ref. [66].

from both the surrounding intracellular milieu and heavy metal stained components because of their low transmitted intensity and bright intensity fringes. Fig 3 provides an example of these features in raw and processed images captured under low magnification, demonstrating that they can be used to detect NDs with zero background. The NDs were successfully isolated from the cellular background in heavy metal-stained samples using a simple two-step image processing method. First, a gradient morphometry filter [62] was used to generate a separate image. Then, by inverting the intensity of the original image to turn dark contrast into bright signal and superimposing the two images, a clearly distinguishable object for each ND results. NDs are detected with high sensitivity because they appear as simultaneously bright and dark objects on the scale of tens of nanometers, producing an exceptionally strong spatial gradient, in addition to their intensity contrast. It can be seen from Fig 4 that NDs can be isolated with zero background signal over areas spanning significant fractions of cells that include cytoplasmic, nuclear and extracellular regions. Because the appearance of NDs in TEM images depends on the crystal orientation and the defocus, most (but

not all) NDs observed can be isolated with zero background from automatically acquired images with human intervention only to select coverage areas. Based on the results from this acquisition method, alteration of the acquisition process to include a limited series of tilt angles or defocus values and diffraction mode imaging at each location should enable all individual NDs to be isolated with zero background in wide area images. Our previous work has demonstrated that diffraction-mode imaging can identify NDs over a magnification range spanning seven orders of magnitude, and that high resolution TEM can conclusively verify the identity of NDs by observing the atomic lattice and by generating diffraction patterns [59].

4.5 Discussion

Fluorescent labeling of proteins has been highly successful for sub-micron visualization of protein localization. Nonetheless, the resolution of optical measurements is subject to Abbe's diffraction limit [71] and super-resolution techniques do not allow for visualization of the cellular environment surrounding fluorescent labels at the nanometer scale. Fluorescence microscopy studies indicate that the cellular uptake mechanism for unconjugated NDs is endocytosis and that NDs are subject to several cellular trafficking mechanisms [57]. Although fluorescence microscopy can determine the localization of particles to the perinuclear region, more advanced optical techniques and carefully controlled experiments are required in order to differentiate targeting to more specific cellular regions, such as localization to the nuclear $v.$ cytoplasmic sides of the nuclear envelope [52]. Moreover, the diffraction limit of light ($\sim$200 nm) imposes a significant obstacle to the mapping of 20 nm nanoparticles relative to a 120 nm macro assembly such as the NPC. Light microscopy precludes discrimination among particles that are bound to the intended target, that are near the target, that have displaced the target protein from its assembly, or particles that are bound in aggregates or nanoscale structures preventing them from directly contacting the intended target. While sub-diffraction methods such as STED microscopy can visualize fluorescent molecules such as NV- NDs, these methods are limited by substantial sample restrictions, the requirement for high laser powers that can bleach fluorophores and damage intact cell samples, inability

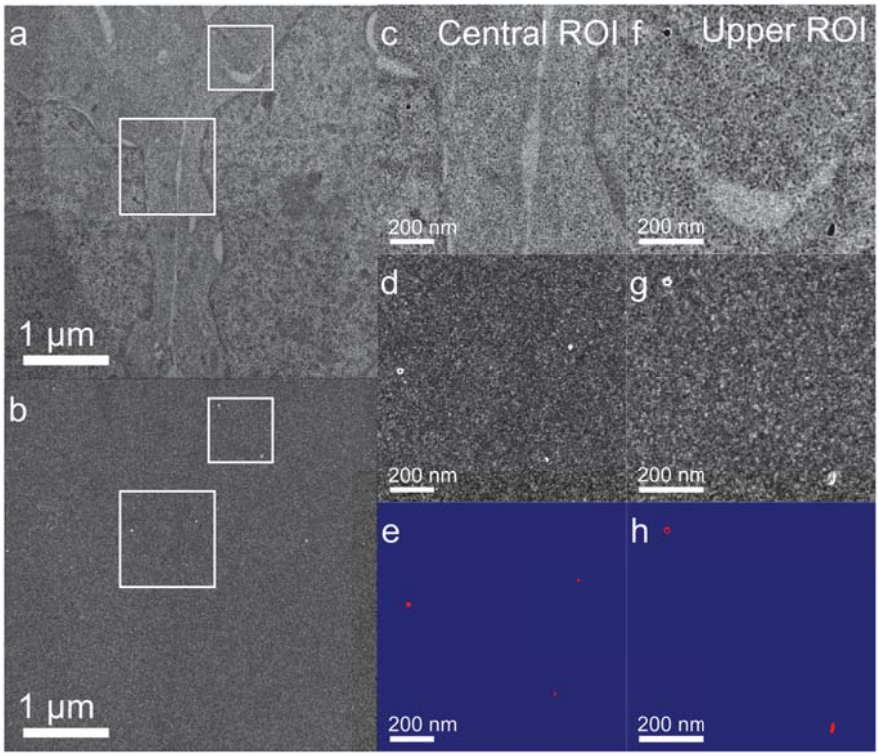

Figure 4.4: Nanodiamond isolation is robust and reproducible. (a) Wide area view of two cells transfected with anti-Nup98- conjugated NDs. (b) Gradient enhanced image of (a). (c) Central ROI from (a). (d) Central ROI from (b). (e) Original image inverted and added to gradient image, then contrasted to show isolation of ND with zero background. (f) Upper ROI from (a). (g) Upper ROI from (b). (h) Original image inverted and added to gradient image with threshold applied to show isolation of ND with zero background. Figure reproduced from Ref. [66].

to distinguish large NDs from clusters because they do not detect the diamond material and the requirement to co-stain any target, severely limiting the interpretation of the context surrounding the target and label. In practice, most sub-diffraction imaging systems are restricted to 40-80 nm resolution in cells [72], especially because STED resolution depends strongly on the power of the depletion beam. Furthermore, even ∼20 nm resolution is insufficient for structural identification of individual macromolecular assemblies such as the nuclear pore or to separate individual NDs when clustered, precluding accurate quantification [73]. In fact, this methodology was specifically inspired as a way to complement STED

and other fluorescent imaging techniques, by providing much of the information inaccessible through these methods.

Nanoscale localization information about the Nup98 nucleoporin of the NPC by immunogold staining of cells post fixation has been studied [74]. However, the ability of antibodies to successfully localize NDs to subcellular regions with nanoscale precision and outside of endosomes in live cells has not been demonstrated prior to this study. Given the resolution limit of light microscopy and the emerging use of NDs as nanoscale optical sensors in live cell thermometry and magnetometry, as well as in drug and gene delivery, knowledge of the precise location of NDs relative to a target of interest is increasingly important.

In previous work, we demonstrated that NDs possess the physical and biological properties necessary to act as landmarks in a cellular environment for TEM using resin-embedded ultrathin sections from HeLa cells [59]. Whether the localization of antibody-conjugated NDs to specific protein assemblies is sufficiently robust to enable live cell labeling of protein assemblies, accounting for transfection and trafficking throughout cells, has not been previously determined and is the subject of this work. In general, quantification of the subcellular location of nanoparticles is difficult due to the large number of sections and images required to unambiguously identify nanoparticles, usually at higher magnifications than the present study, and the difficultly of normalizing to the variable geometry or volumes of the sub cellular regions being compared. [75, 76] By utilizing a recognizable, homogeneously sized macromolecular structure, the NPC, and the binary criteria of being inside or outside of the nucleus, our analysis avoids these complications.

We show here that NDs provide a robust, identifiable landmark that can be used to direct expensive and time-consuming tomography studies to specific regions of interest (ROIs), providing a high probability of detecting the target of interest, even if the identity of the protein assemblies and their constituents cannot be verified until after image processing and reconstruction. Using this method, low magnification images with wide fields of view can provide quantification of NDs or identification of ROI's around NDs with automated image collection. Low SNR is an inherent limitation in TEM of cells; increasing beam exposure enhances SNR at the cost of increasing damage to the sample.

Targeting of biologically inert contrast agents such as NDs with high specificity to sub-cellular structures can extend the applications for TEM imaging of biological structures by providing a multi-functional label capable of correlating fluorescently detected sensor signals and images with structural information obtainable exclusively by TEM. Nanodiamonds offer several distinct advantages over other nanoparticles used for probing biological systems using TEM. Quantum dots (QDs) are amenable to surface functionalization but lack the versatility of binding, especially directly to proteins, offered by a heavily carboxylated surface. They are also generally cytotoxic [77,78] and are prone to intermittent fluorescence [79]. Moreover, QD fluorescence is quenched by osmium tetroxide fixation [80] limiting the practicality of QDs for multimodal imaging. Gold nanoparticles (AuNPs) lack the biosensing capabilities of NDs [43], do not readily undergo endosomal escape, accumulating in endosomes even after accounting for diverse strategies to aid in cytoplasmic delivery [81,82], and are not easily distinguished by appearance in electron micrographs from OsO_4-stained cytosolic lipid droplets [83].

Unlike NDs, AuNPs are not bioinert and produce cytotoxic effects at concentrations as low as 20 nM [84]. AuNPs may also induce protein aggregation at physiological pH due to the high affinity of gold for free thiols on proteins, which are abundantly present in the reducing environment of the cytoplasm [85]. While capping and surface modifications can reduce these effects, their removal in vivo and resulting exposure of the bare gold surface makes modified AuNPs unattractive for long-term biological labeling or clinical applications [86]. Finally, metal oxide nanoparticles are useful as contrast agents in TEM but exhibit high cytotoxicity [87, 88] and lack the versatility of NDs, especially the sensing capabilities and the availability of surfaces for direct covalent conjugation of proteins.

Based on our results, targeted NDs can identify specific sub-volumes or cellular ROIs with sufficient efficiency to target high-resolution imaging or electron tomography. To improve detection, acquisition of a minimal defocus series including positive defocus at each location will enable detection of variations in ND fringes with the defocus, further capitalizing on the material differences between crystalline and amorphous carbon structures, which ideally show no contrast at positive defocus. Furthermore, this signature can be analyzed using

image- based, high-content recognition algorithms similar to those currently used in fluorescence microscopy to identify subcellular geometric patterns in drug screening assays [89]. Automating the recognition of fiducial or correlation markers over whole cell areas provides a major advantage for in situ imaging approaching the structural level, fiducial marker identification for reconstruction of electron tomograms and single particle reconstructions of large numbers of repetitive images to refine structures. This method has direct applications in traditional TEM as well as in focused ion beam thinned cryo sections, where the imaging necessary to locate structures of interest can significantly degrade the sample. We are currently optimizing methods to extend this technique to correlated light (live cell) and electron microscopy without the need for specialized microscopes or stages.

Beyond research, this method has applications for improving the analysis of both ND and monoclonal antibody-based therapeutics. TEM-based ND imaging enables the localization of therapeutic antibodies bound to NDs in tissues of humans or animals to be determined unambiguously at the nanometer scale. To date, an increasing array of monoclonal antibodies have been approved by the Food and Drug Administration (FDA) to treat cancer, autoimmune diseases, allergic asthma, viruses, blood disorders, organ transplant rejection, osteoporosis, and several other disorders [90]. PPI dendrimers also have promise in therapeutic applications. In vivo studies with rats have demonstrated that 25% conjugation with maltotriose reduces cytotoxicity to a minimal level and 100% conjugation eliminates detectable toxicity at all doses tested [63]. When tested on panels of human cells for pharmaceutical applications, densely maltotriose-conjugated dendrimers were the least cytotoxic form of PPI glycodendrimers, compared to unconjugated, partially conjugated and maltose-conjugated PPI dendrimers [91]. Given their low cytotoxicity profile, maltotriose-conjugated dendrimers hold promise as a component of therapeutics for use in humans [92]. The third part of our targeting strategy, the NDs, are also generating increasing interest as therapeutic agents. In vivo studies in mice have shown that intraperitoneal injection of NDs did not cause detectable cytotoxicity in the central or peripheral nervous system or impair neural function based on gross animal behavior and hippocampal novel object recognition (NORT) tests which can report damage to the hippocampus [93]. A recent study concluded that 20

and 100 nm carboxylated NDs showed no cytotoxicity or genetoxicity measured in real time in six human cell lines derived from liver, kidney, intestine and lung tissue, with ND doses up to 250 μg/ml and recommended that carboxylated NDs be considered for use as a negative control in nanoparticle toxicity studies [51]. The added advantage of detectability by TEM at the nanoscale, compared to other candidate medicinal nanoparticles or antibodies alone, could improve and expedite clinical trials for NDs as vehicles for antibodies, proteins, nucleic acids or drugs, potentially lowering costs and reducing ambiguity about the subcellular fate of these particles in preclinical studies. Due to the long-term chemical stability of NDs, this imaging method could also help assess tissue penetration and persistence of therapeutic NDs in biopsies or post mortem tissue immediately following or months after ND administration. Nanoscale imaging of NDs identified as bound to or near a target of interest or accumulating inside cellular structures where they are isolated from the target of interest can correlate therapeutic efficacy measurements with ND location by direct visualization.

Determination of the mechanisms of action and drug resistance for monoclonal antibody therapies are increasingly important for improving clinical outcomes and studies on trastuzumab emtansine show that acquired resistance may be due to reduced binding of the antibody to cancer cells, inefficient internalization or intracellular trafficking, heightened recycling of the antibody-target complex or impaired lysosomal degradation [94]. The ability to successfully target and identify the subcellular location of ND-antibody-target complexes by TEM could contribute significantly to further studies of these mechanisms.

4.6 Conclusions

We have demonstrated a method to prepare, deliver and image ND-antibody conjugates for labeling of cellular protein assemblies. We chose the Nup98 nucleoporin, a component of the NPC, as the target for our study because of the recognizable structure of the NPC, its well defined location and the significance of its physiological functions for sensing and drug delivery applications. Using TEM, we assessed the percentage of NDs bound to the Nup98 nucleoporin at the NPC on a single diamond-single complex basis. In addition to

localization at the NPC, we observed clustering of diamonds at other locations, distinct from the NPC, where Nup98 is known to localize. Our results demonstrate that NDs can be identified individually over the area of entire cells at low magnification with near zero background signal from first pass automated image acquisition.

Using the unique signature of NDs observed under TEM in biological samples, we have measured the distance of individual NDs to individual NPCs from images taken over wide areas and with automated acquisition, demonstrating the minimal image requirements necessary to identify NDs. Given the established efficacy of NV^--containing NDs for fluorescence microscopy applications, our results highlight the value of NDs for correlated imaging. Widespread use of correlated fluorescence and electron imaging has been hindered by practical limitations surrounding the markers and sample preparations. Here we have described a TEM based method that enables high precision localization of particles and the ability to recognize ROIs with a novel TEM marker. This method is compatible with live cell optical microscopy using an established non-bleaching fluorophore (NV^- ND), allowing for practical correlated imaging that can be performed on separate light and electron microscopes, thereby facilitating extension of correlated imaging beyond specialized instruments to equipment readily available at most research institutions. Our technique has the ability to complement and outperform the common method of fluorescence-based localization. We have recently extended this technique into plunge-frozen, whole, unstained cells to provide a versatile and unambiguous standard that can provide localization of particles at the level of proteins and protein assemblies without requiring costly embedding and sectioning.

We further investigated the appearance of NDs observed by TEM, and noted that the maximum and minimum transmitted intensities from NDs are each more extreme than the signal variation from the resin-embedded cellular background or heavy metal staining. We also observed geometrically consistent, ring-shaped intensity gradients likely due to a combination of thickness- and phase-based intensity fringes, capable of providing well defined geometric features for computer-based recognition. These features will likely prove valuable for automated acquisition and tomographic reconstruction.

CHAPTER 5

All Optical Imaging of Action Potentials in hESC Cardiomyocytes with Electrically Modulated Fluorescence from Nitrogen Vacancy Centers in Internalized Nanodiamonds

5.1 Introduction

Nitrogen vacancy (NV) defect centers in diamond have robust physical characteristics that have been utilized for far field optical sensing in several ways including optically detected magnetic resonance, charge state detection and combinations of both. NV centers can exist stably in at least three charge states: NV^-, NV^0, and NV^+. The stability of each of these states is affected by the electronic band structure inside the diamond, which is altered by application of external electric fields. In bulk diamond, external electric fields provided by application of voltage through electrolytic fluid on a diamond surface have been shown to affect the charge state of NV centers within $\sim$ 20 nm of the surface [95]. In the case of NV centers in nanodiamonds (ND), reduced particle diameters result in an increased number of surface exposed NV centers, enhancing the susceptibility of the NV center to charge state manipulation by external electric fields. Work on nanodiamonds containing a single NV center in conductive solution provides evidence that transitions between NV^- and NV^0 are affected by electrochemical potential, mediated in part by electric field effects at the ND-solution interface and in part by electron transfer from the ND to the solution and ultimately the electrodes, while transitions from NV^0 to NV^+ are mediated almost exclusively through electron transfer to electrodes [96]. The fluorescence output of NV defect centers in diamond depends strongly on the charge state. NV^- centers have a zero phonon line (ZPL) of $\sim$ 638 nm and a peak spectral emission around 690 nm due to phonon coupling induced broadening. In comparison, NV^0 centers have a ZPL around 578 nm, with a peak spectral emission at 645 nm, and NV^+ centers are not fluorescent [96]. These centers can also be distinguished

at a single defect level by comparison of the number of photons emmited per second after an initialization and readout illumination sequence with two lasers [97]. The charge state can be manipulated by optical excitation for different times, excitation intensities and excitation wavelengths and the charge state can be optically read out without altering it by using low excitation power [97]. Use of external electric fields to actively control the NV charge state has been demonstrated by nanopatterned electrodes on a bulk diamond surface, and this effect is an enabling mechanism in a diamond based, scalable quantum computing proposal, allowing reduction of coupling of the NV center to nearby spins by conversion to the NV^+ state [98].

Quoting from the Advisory Committee to the NIH Director's Interim Report, "Brain Research through Advancing Innovative Neurotechnologies (BRAIN) Working Group's:

> Nanodiamonds, for example, are particles whose photochemical properties-fluorescent light emission-might be tailored to exhibit sufficient sensitivity to applied electric fields to serve as optical reporters of electrical activity. With respect to neuroscience applications, however, essentially all aspects of this proposed technology are untested, from deployment of the particles within the neuronal plasma membrane to measurement of the light signals.

To test the potential of NV centers in NDs (NVNDs) for use as nanoscale voltage sensors in electrophysiologic tissue, we have delivered nanodiamonds to human embryonic stem cell derived cardiomyocytes (hESC CMs) and successfully observed fluctuations in fluorescence in response to cellular contractions that are consistent with the voltage fluctuations that occur in cardiomyocytes. To verify the source of the fluctuations we also provide measurement with a voltage sensitive (VS) dye, FluoVolt, for comparison.

In the development of fluorescent dyes for use in recording optical action potentials (OAPs), the gold standard in the literature for validation of new chemical entities as voltage sensitive (VS) dyes has been presentation of simultaneous patch clamp and fluorescence data and confirmation of a similar shape profile in an overlay. Today, voltage sensitive dyes have achieved remarkable performance and have been thoroughly validated by simultaneous patch

clamp recording, including FluoVolt, one of the latest generation of photoexcited electron transfer (PET) based VS dyes. Because of the established record of VS dyes to profile action potentials in cardiomyocytes [99] in the literature and the high quantitative accuracy accross wells afforded by a high througput drug screening platform, we concluded that side-by-side comparison of the NVND fluorescent signal with a VS dye was sufficient to validate the signals were both representative of the same dynamics.

5.2 Materials and Methods

5.2.1 hESC culture and maturation

H9 (WA09) hESC lines were maintained as described before [100] hESCs were routinely verified as mycoplasma-free using a luminometer. hESCs were grown and differentiated in a chemically defined condition [101]. Briefly, hESCs were detached and held in suspension culture using cardiac differentiation medium (DCDM) containing IMDM and DMEM (ThermoFisher) supplemented with 1% MEM nonessential amino acid solution, 2 mM L-glutamine, 1% penicillin-streptomycin (ThermoFisher). The medium was additionally supplemented with chemical compounds: 1 μM CHIR (Abcam) for first two days and switched to KY021111 (a gift from Dr. Minami Itsunari, Osaka University) and XAV939 (Santa Cruz) on day 3 and day 5 of differentiation. DCDM was changed every ten days after differentiation day 10. Usage of all the human embryonic stem cell lines is approved by the UCLA Embryonic Stem Cell Research Oversight (ESCRO) Committee and the Institutional Review Boards (IRB) (approval #2009-006-04).

5.2.2 Delivery of Nanodiamonds

ND delivery protocol is as described in Lake et al. [38, 66], with variations described below. The NDs used were 40 nm carboxylated high NV content NDs (Adamas). NDs were used directly without additional acid treatment and sonicated for 2 hours prior to use. 10 μg (1 mg/ml in DI water) of ND were mixed by pippette with 2 μl of PPI dendrimers (2.5 mg/ml in HEPES buffer) and allowed to equilibrate for 20 minutes at room temperature. This solution

was then added to hESC CM cells in a 384 well plate with freshly changed media allowed to equilibrate in the incubator ahead of time. Note, hESC CM culture media does not contain serum and this was used throughout all stages. Cells were incubated with ND:PPI mixture for 1 day at 37 °C with 5% CO_2. The media was changed the morning before imaging or every 4 days. The cell culture was stable and regular imaging was conducted periodically over the course of several weeks, generally.

5.2.3 Imaging

Imaging was performed on a Molecular Devices ImageXpress XL high throughput screening microscope with temperature controlled stage. Images were acquired in sets of 800 frames with 20 ms exposures, 16 bit pixel depth, 2048x2048 pixel resolution binned 2X to 1080x1080, and a 20X objective, captured sequentially with the phase contrast transmission channel and Cy3 and Cy5 fluorescence channels with the standard filters. VS dye was imaged with the FITC channel and used as specified in the manual in the regular cell media. The long pass mirror after the filter cube provided a 675 nm cutoff. Cells were imaged immediately after leaving the incubator and returned immediately after imaging. Imaging generally required 30-60 min depending on the number of sites and number of conditions per 384 well plate. HEPES solution was added to the media to a final working concentration of 20 mM to ensure maintenance of CO_2 levels in the culture media. Image focus was determined by laser auto ranging followed by image based optimization and image series were acquired at 2-4 sites per well, with each condition prepared in duplicate or triplicate.

5.2.4 Image Processing

Image manipulation was kept strictly minimal and based on scientific rationale. Specifically, NVNDs have been shown to be non-photobleaching, and while the charge state can be altered, it can also be refreshed limitlessly. Continuous observation without photobleaching for over one year has been documented [102]. In contrast, fluorophores in cells and media, and in general most fluorophores, are subject to signficant photobleaching during prolonged

exposure at the intensities commonly used in fluorescence microscopy. From these assumptions, it could be predicted that if an electrically modulated signal predominantly originates from a source that is not subject to photobleaching (e.g. NVNDs), then by subtracting the exponential decay from the observed signal, the remaining constant offset should be enriched in the modulated NVND signal. This subtraction also serves to flatten the baseline, providing a uniform comparison of peak heights over time. The decay in the fluorescence was fit by a biexponential decay functional which provided the best fit best without overfitting on a per pixel basis. Motion artifacts can create patterns in which a bright pixel becomes dark during a contraction and then returns to bright after relaxing, resulting in negative peaks. Intensity changes due to shifts in electrochemical potential at various points in the cell could also produce negative peaks that are of true physiologic significance. To compensate for this and to remain consistent with common image formats, it was also necessary to offset any negative intensities , and the absolute value of the global minimum for all pixels across all time points for the entire image series is added to the entire dataset. All math operations are performed with values converted to 32 bit depth. Last, the image is normalized by scaling the intensity of the entire data set with the global minimum and global maximum rescaled to 0-65535, consistent with the original 16 bit intensity resolution from the microscope. The baseline was also flattened as needed for a few phase images that showed a clear logarithmic trend, and after fitting a logarithmic function with form Y=A+B*log(X+C) were subtracted from the ROI intensity sum time trace. This trend was attributed to the illumination lamp.

5.3 Results

Upon analysis of fluorescence from NDs delivered to hESC CM's in previous experiments for antibody targeting, it was noted that significant peaks in the fluorescence were visible in the time trace of the intensity for regions of beating CMs. To further explore whether these signals were consistent with charge state fluctuations driven by the electrical changes (electric field, electrostatic potential, or charge transfer) occuring during the action potential of a beating cardiomyocyte, we utilized the high speed streaming capability and shot-to-shot stability of a drug screening microscopy system to visualize small changes in the fluorescence

signal from nanodiamonds delivered to cells. Imaging was performed periodically over two weeks. Figure 5.1 (A-C) shows the full field of view for one site in the 384 well plate. Phase contrast imaging allows characterization of the highly repetitive cellular motion during a contraction [103], providing comparisons with fluorescence images in order to identify dynamics not explained by physical motion that could be attributable to electrical effects. Figure 5.1 (D-F) shows a zoomed region that displayed strong contractions. The frame was chosen to be immediately after the initial rise in the first peak in the fluorescence and phase channels. In comparison, Figure 5.1 (G-I) show the same region during the rest period before the contraction. Labels identifying each region used for analysis are shown in Figure 5.1 (E).

Because varitations in signal can occur through motion in or out of the region under analysis or through intensity changes, we chose to analyze the regions by comparing the signal contribution from the pixels on the boundary of the region to the signal from the entire bounded region, inclusive of the boundary. This is based on the premise that the intensity changes caused by motion of small objects, relative to the field of view, will loosely follow a pattern in which the pixel intensity fluctuations in the boundary should be stronger than the fluctuations of the integrated intensity of the entire region. Idealized planar motion should show conservation of pixel intensity throughout the region, except for pixels that cross in and out of the boundary.

Motion of pixels that do not cross the region boundary do not contribute to intensity changes. Peaks in the overall intensity trace of a region of interest that originate from motion artifacts show a consistent and logical trend, identifiable by examination of the intensity traces of the bordering pixels. Specifically, the peaks present in the intensity traces increase in signal to noise from the full region sum, to the bounding ring sum, to the specific bounding edge (e.g. top) consistent with the traces shown in Figures 5.2 and 5.3.

In contrast, genuine intensity changes in the fluorescence output due to changes in the NVND charge state should have the opposite behavior. Pixel intensity should increase or diminish as non-conserved pixel intensity, without any flux through the boundary. Clear examples of this are shown in Figure 5.4, where no significant signal contribution comes from the bounding pixels.

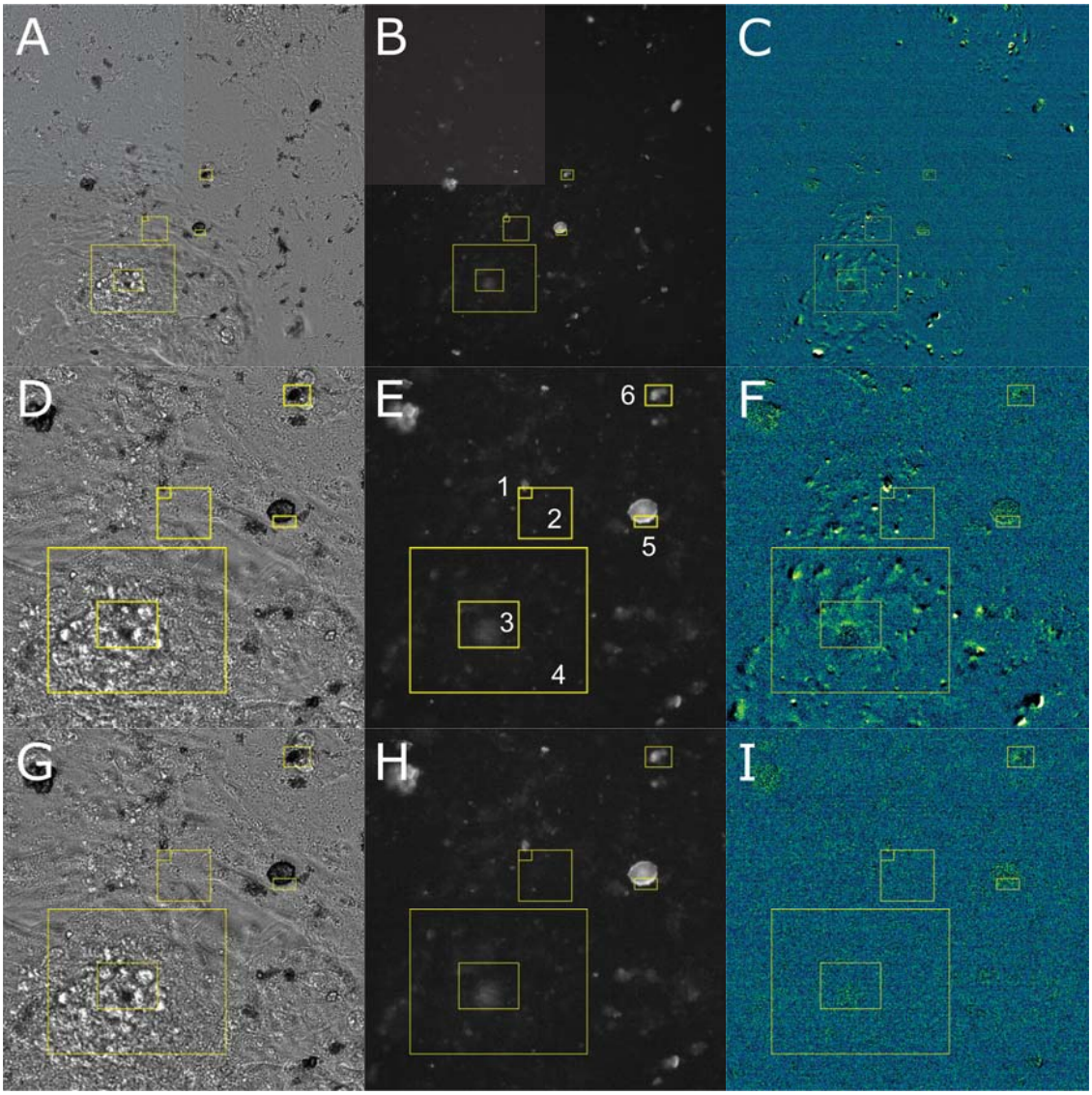

Figure 5.1: (A-C) Full field of view images (724 (w) µm x 724 (h) µm) in 384 well at initial peak of contraction. (A) Phase Contrast (frame 105, 2.1 s). (B) Cy5 (frame 131, 2.62 s). (C) Cy5 with baseline correction by fitting and subtracting a biexponeneital exponential decay function at each pixel, then offsetting to account for negative values and normalizing to the global min/max for the entire image and time series. (D-F) Zoom to regions of analysis (335 (w) µm x 335 (h) µm). (G-I) Frames during resting period. (G) Frame 42, 0.84 s. (H,I) Frame 14, 0.28 s

Voltage and calcium sensitive proteins and dyes all have strengths and weaknesses. Because NVNDs are non-bleaching and can be localized to specific biological structures, these

sensors could be highly advantageous in sensing specific subcellular regions over long periods of time, while avoiding exposure of the cell to unnecessarily broad staining. Figure 5.6 provides evidence that NVNDs possess the necessary properties for use in this application. The NVND sensors were also able to detect a single or small group of cells beating with an arrhythmia consistent with being chronically triggered: repolarization followed immediately by depolarization. As shown in Figure 5.6, this further confirms that NVNDs provide sufficient signal to identify relevant functional events in cardiac biology.

Figure 5.8 shows fluorescent traces for three regions of varied size from two different wells. While the pattern exhibits some shape differences between the two different synchronized groups of cells, many features of the shape are conserved and regions of different sizes from subcellular, to cellular, to tissue scale show highly reproducible patterns. Figure 5.9 shows a single OAP for all three sized regions in Figure 5.8(B) (black axis). Overlaid in green (green axis) is the fluorescent signal from the NVNDs. The detailed similarity of the shape profile provides strong evidence that the NVND signal shape can be almost completely explained by the voltage signal reported by the VS dye.

Besides localization at the nanoscale, lack of photobleaching and little to no cytotoxicity are two additional benefits offered by NVND sensors. In this experiment, we observed hESC CMs remaining healthy and beating strongly when cultured with very high NVND concentrations (200 μg/ml) for extended periods of time, often in excess of 2 weeks after delivery of NVNDs and with many rounds of imaging. Figure 5.10 shows images of the cell culture over the first 7 days with NVNDs (A-F). On day 7, VS dye was added to assess the voltage signal for comparison. On the seventh day, strong, regular contractions similar to those seen in Figure 5.10 were observed. After media replacement and return to regular cell culture, the same well was stained again with VS dye and imaged with the Cy3, Cy5 and FITC channels in the same afternoon. In contrast to the repeated imaging with the NVNDs, the VS dye appears to have caused a decline in the health of the cells, evidenced both by cell morphology and by the signal response in the FITC channel shown on the right of Figure 5.11. After only two rounds of imaging the cells stopped beating. This was attributed to either long term culture with the VS dye remaining after wash or acute phototoxicity caused

by the dye during imaging with a different excitation wavelength that could have created phototoxic byproducts. Also of note, there are areas where cells are removed from the plate. In contrast, the end point generally observed for CMs with NVNDs is highly similar to that of untreated hESC CMs, with an otherwise intact cell monolayer (or clumps) that have just stopped beating. Occasionally, the beating will slow to one beat every 10 seconds or less before ceasing, but beating rapidly then ceasing to beat shortly after was not observed with NVNDs over the course of the experiments.

5.4 Discussion

The predominantly positive peaks in response to positive intracellular potential swings is consistent with published experiments [96]. This report showed that electrochemical potential changes through conductive contacts as well as electric field applied to nanodiamonds through a passivated electrode both contribute to increased fluorescence output in response to rising voltage and vice versa. This was attributed to a shift in the energy levels of the conduction band for near surface NV centers in nanodiamonds that stabilize the NV^0 state. One aspect of the NV charge state dynamics that has not been addressed is the consideration of combined optical and electrical effects on the charge state. When an NV^- center is ionized and the electron travels to the neighboring N^+, it may not always travel directly and could populate metastable defects, vacancies, neighboring NV centers etc., as well as being ionized into the solution. Electrons transferring from the conduction band back down to a bound ground state, including NV^0, have enough energy to populate the excited state of the defect or atomic system, which subsequently relaxes to the ground state, emitting a photon. While electrical effects may not be coupled sufficiently strongly to drive these transitions, the shift in the Fermi levels could alter both the distribution of electronic states in the diamond and charge transfer dynamics.

Due to the complexity of the micro environment in CMs during an action potential, there are potentially several mechanisms that could explain the changes in fluorescence observed in these experiments. X-Y motion was analyzed explicitly. However, Z motion should be

considered. The microscope used is not confocal and the Z dimension for the focal spot is ∼5 μm. Not only is this likely to include the entire cell in the Z dimension, but this focal volume is not the limit from which light is still collected in epifluorescence, lessening the intensity changes due to focus effects. While calculations could be performed to place bounds on the contribution of motion artifacts in the Z dimension based on purely geometric arguments, these artifacts cannot explain several other consistent characteristics in the observed signal including appearing to spread between cells (indicative of networked gap junctions) like a VS dye in comparison to a calcium dye, which has a more cell centric pattern dominated by the response of each individual cell. The signals from NVNDs also feature fast intensity changes over large areas, and an asymmetric peak shape that matches almost exactly in fine detail with the signal from the VS dye.

Charge state dynamics [104] and photoconductivity [105] in NV diamond has been a major area of progress in recent years and protocols that utilize readout and control of the NV charge state to achieve read out, control or coupling to both electron and nuclear spin states either composing or adjacent to the NV center, and vice versa, have been successfully demonstrated [106], [107] and extended into practical applications. [108] By moving these experiments to a more versatile platform compatible with these protocols, both the signal to noise and versatility of measurements can be improved dramatically and taken down to the single NVND level to interrogate gap junctions, axons, dendritic spines, synapses, and other organelle scale features. With regular advances in producing NVNDs, judicious cellular targeting and the application of advanced optical, charge and spin based protocols, NVNDs should be considered one of most promising candidates for a workhorse nanoscale voltage sensor for use in electrophysiological tissue, despite the modest (∼1 %) electrically driven change in fluorescence as a percentage of total fluorescence. As is common for experiments with VS dyes, the large fluorescence shifts demonstrated in controlled experiments often yield significantly reduced signal to noise when measured in commercially relevant environments like high throughput drug screening or when used in whole tissues.

5.5 Conclusion

In this report, we present what is to our knowledge the first recorded optical detection of an action potential (OAP) in electrophysiological tissue using NV centers in nanodiamonds as nanoscale voltage sensors delivered internalized in hESC CMs, or any other cell type. We were able to achieve sufficient time resolution to accurately characterize the observed fluctuations in NVND fluorescence during the contraction of hESC CMs and to compare them to an established voltage sensitive dye. Overlaying the signals from the putative voltage sensor and a well characterized voltage specific dye provides strong evidence that the intensity changes seen in both fluorescent signals are sufficient to detect the intracellular voltage changes during spontaneous contractions of hESC CMs. Building on our previous demonstrations that nanodiamonds can be targeted to specific cellular assemblies, and are stable, uniquely identifiable labels for use in electron and light microscopy, the current work expands this set of features to include stable persistence after uptake in hESC CMs for weeks without inhibiting muscle contractions. With this first demonstration of NV containing nanodiamonds as a single chemical entity that can enable the simultaneous study of function and structure in electrophysiological tissues at the nanometer spatial scale necessary to separate the smallest functional units, e.g. synapses and gap junctions in brain and cardiac tissue, respectively.

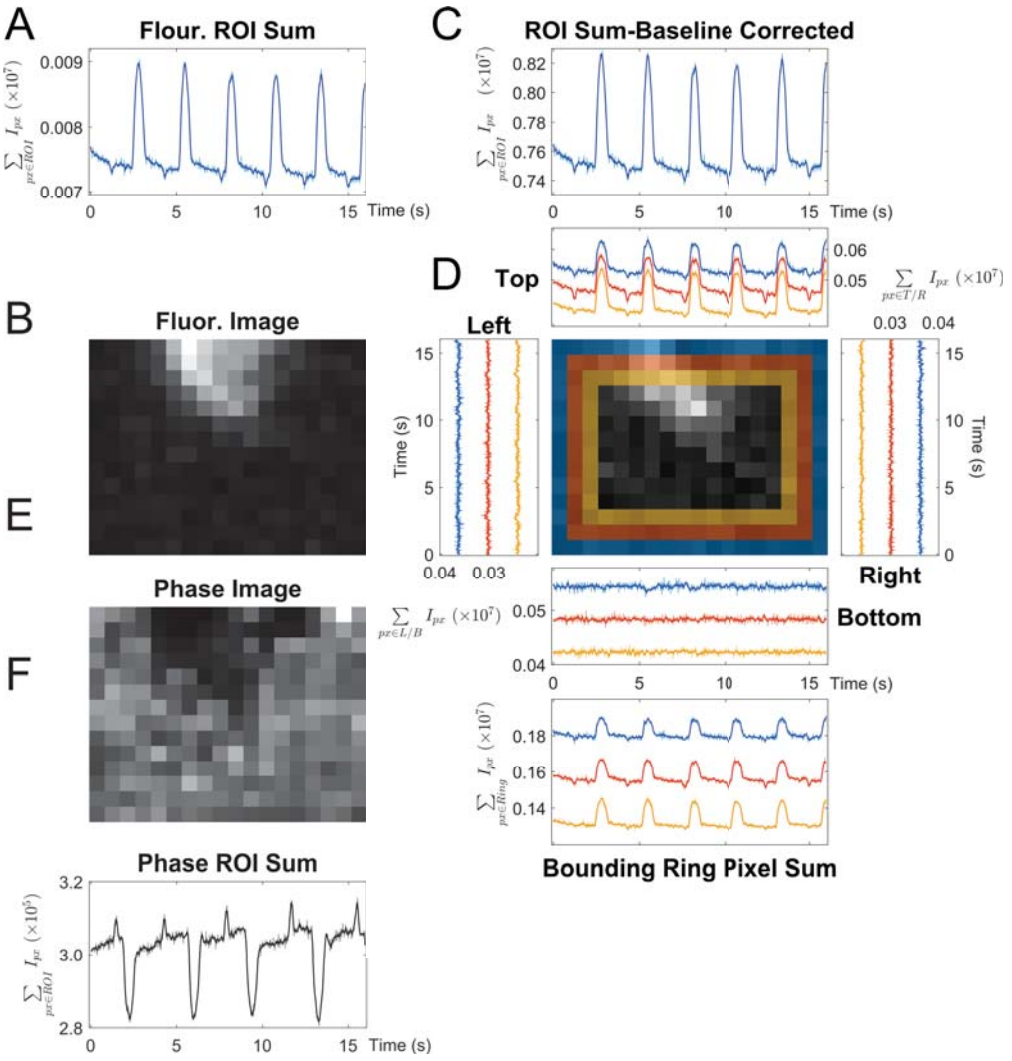

Figure 5.2: Region 1. Motion artifacts from 40 nm carboxyated nanodiamonds in hESC Derived Cardiomyocytes. All traces show the 5 frame moving average in bold over the raw data, captured at 20 ms intervals (50 FPS). Region size: 12.1 (w) µm x 9.4 (h) µm (A) Sum of intensity for all pixels in the selected region. (B) Same as (A), but for the baseline corrected image series. (C) Uncorrected fluorescence image (Cy5 Channel, frame 131, 2.62 s) at the initial peak of contraction. (D) Baseline corrected fluorescent image with showing intensity sum traces for interior bounding pixels on top, right (dim.= image width) and left, bottom (dim.= image height -1), and the sum of the bounding pixel ring for pixels 1 (blue), 2 (red) and 3 (yellow) pixels into the image. (E) Phase contrast (frame 105, 2.1 s) image of the same region at the initial rise of contraction. (F) Intensity sum for all pixels in region from phase contrast image.

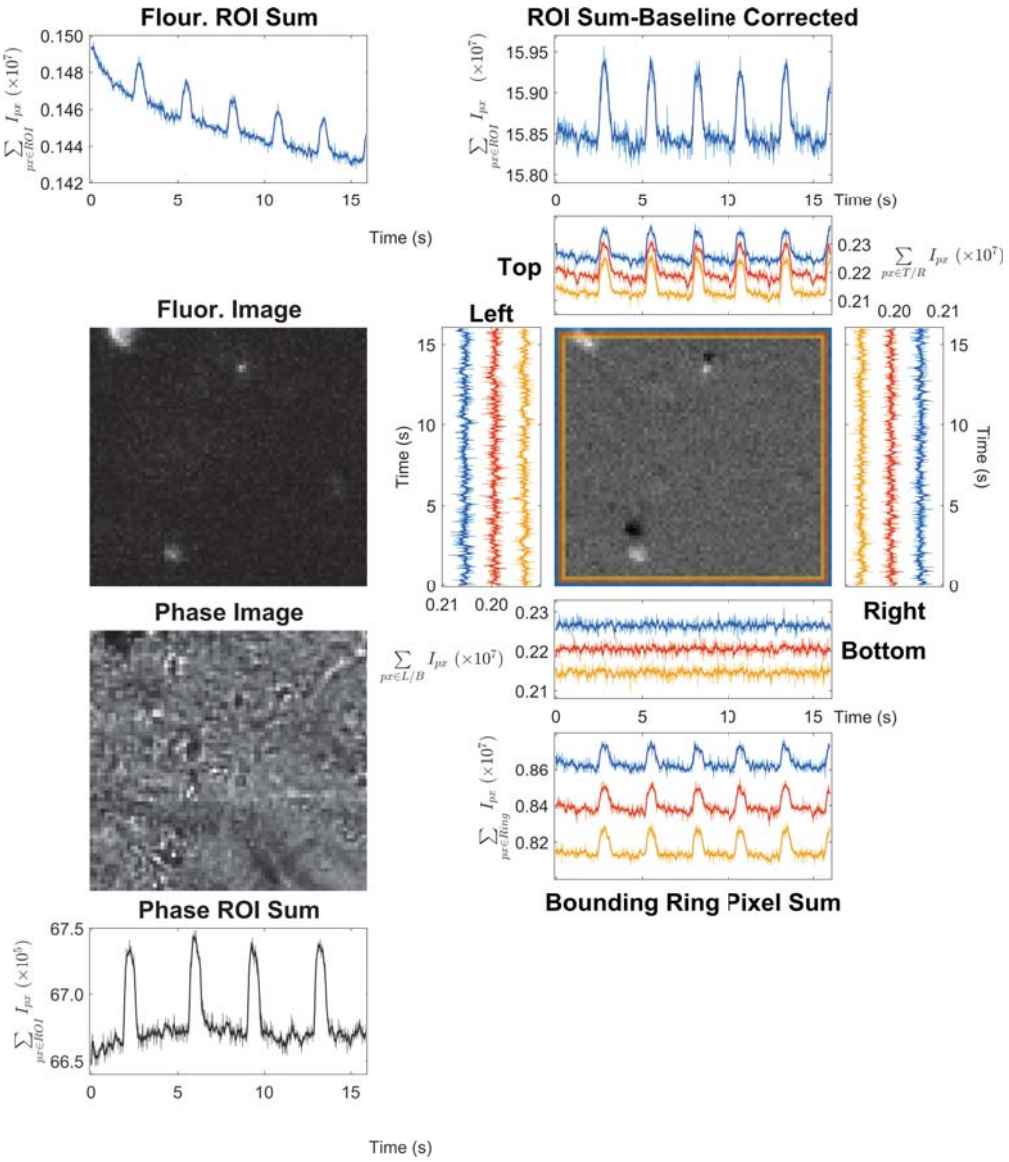

Figure 5.3: Region 2. (A-F) are as described in 5.2. Region size: 50.3 µm (w) x 47.0 µm (h). Impact of bright pixels moving at the region of interest boundary on the intensity trace over a wide area. Note increasing signal to noise of peaks from region sum, to boundary sum to individual boundary edge, indicating the source of the peaks in the ROI has a significant contribution from motion at the boundary.

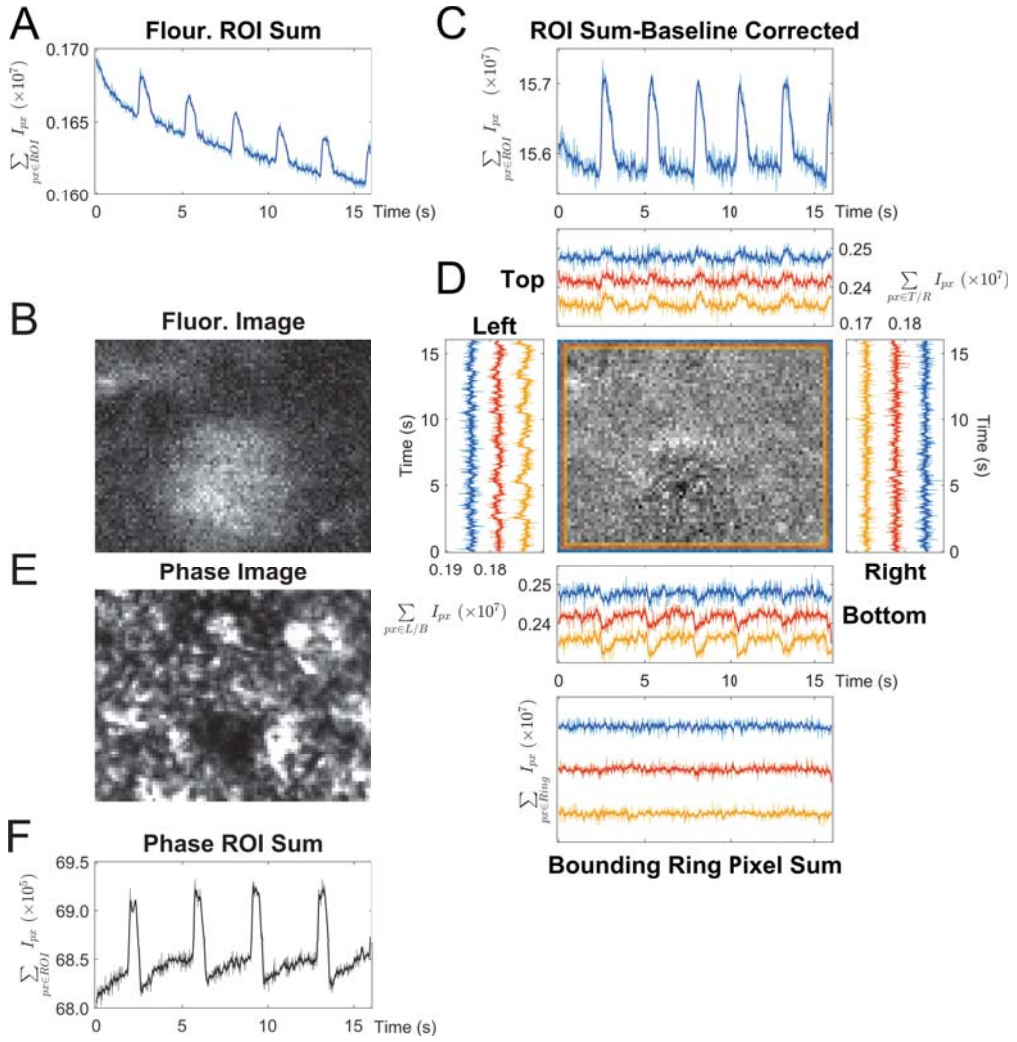

Figure 5.4: Region 3. (A-F) are as described in 5.2. Region size: 50.3 μm (w) x 42.2 μm (h). Region of several cells with carboxylated nanodiamonds delivered internally by PPI dendrimers. Fluorescent signal in (D) shows increased intensity at the edges of the cell. The sharp rise and asymmetry in the fall of the peak shape is consistent with peak shapes observed with other voltage and calcium dyes, but not the physical contraction.

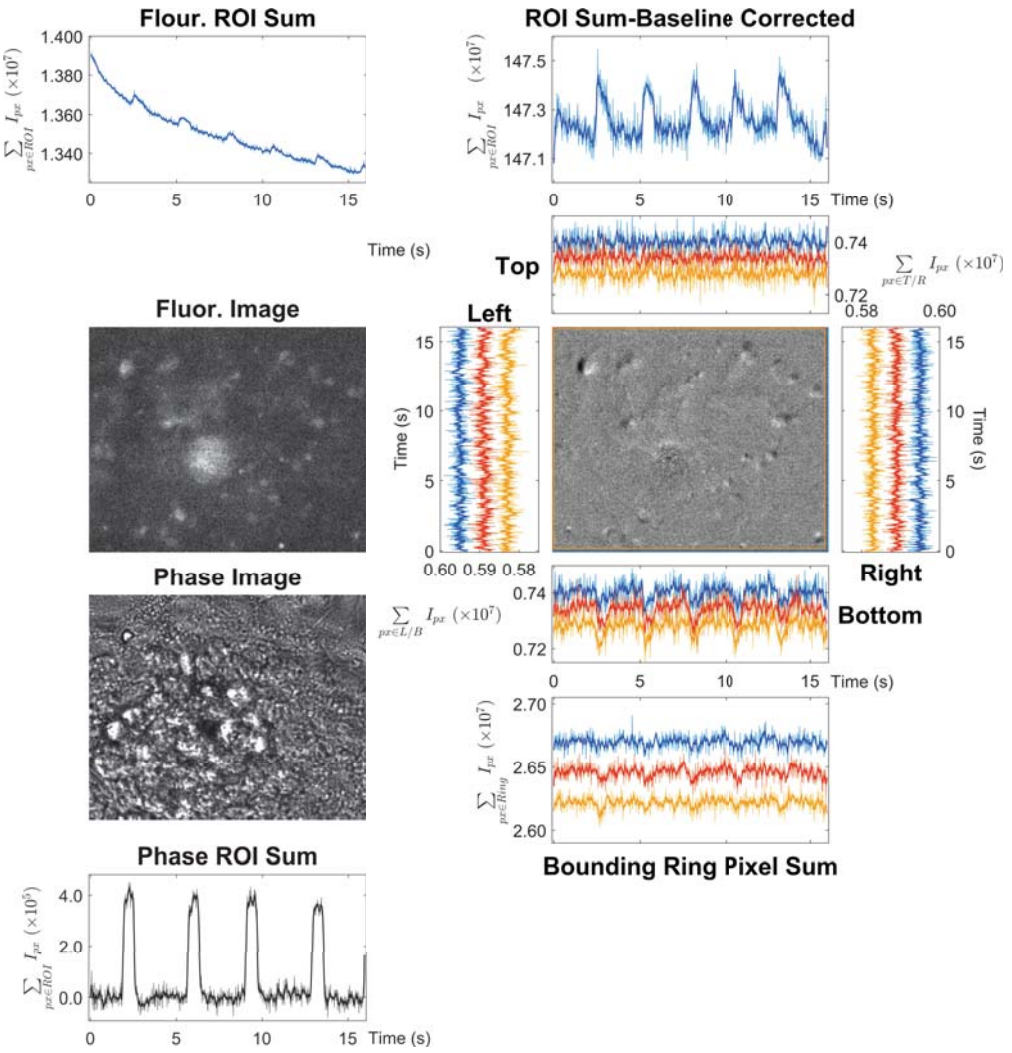

Figure 5.5: Region 4. (A-F) are as described in 5.2. Region size: 164.2 μm (w) x 133.3 μm (h). Fluorescent signal from a wide area containing many cells showing that the observed signal shape is consistent across a significant region containing many cells and reducing the impact of any boundary contributions to motion.

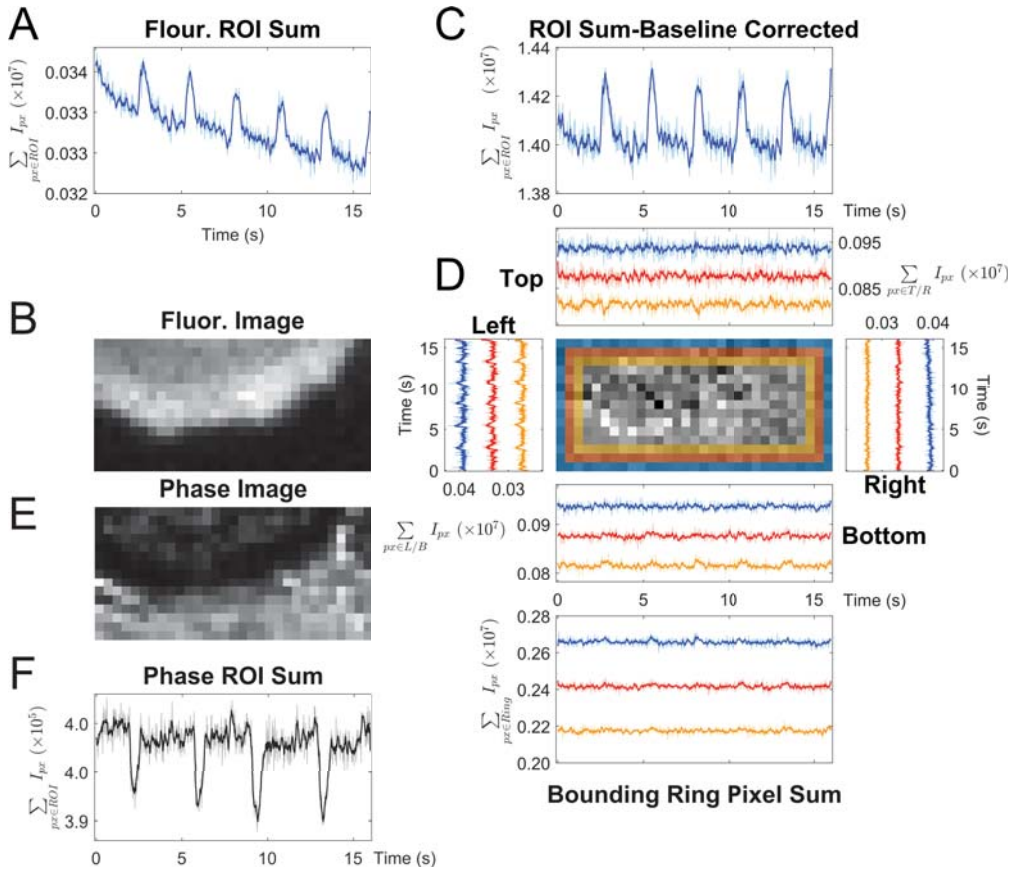

Figure 5.6: Region 5. (A-F) are as described in 5.2. Region size: 20.8 μm (w) x 10.1 μm (h). Fluorescent signal from cell edge showing a similar asymmetric peak shape, demonstrating that optical action potentials can be imaged at a subcellular region of interest with NV fluorescence from internalized nanodiamonds.

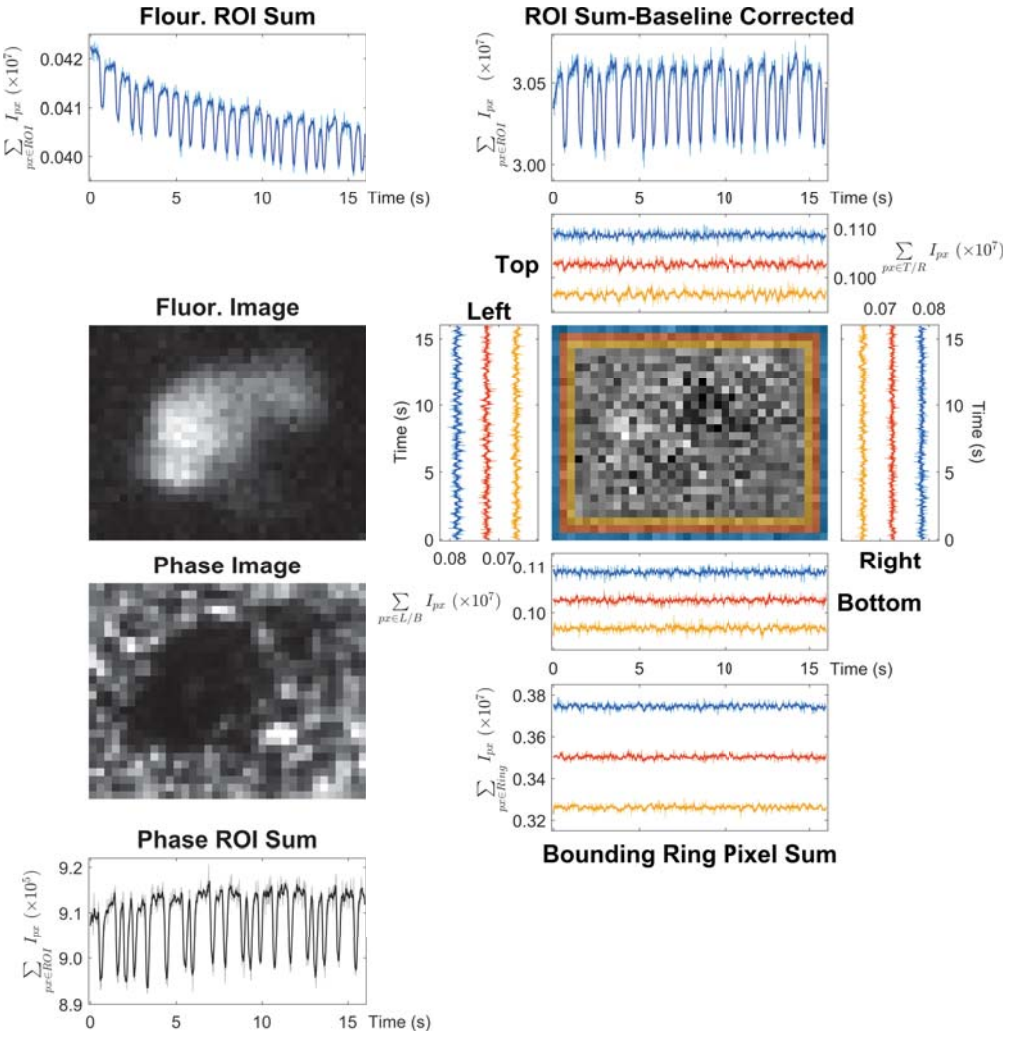

Figure 5.7: Region 6. (A-F) are as described in 5.2. Region size: 24.1 μm (w) x 18.8 μm (h). Detection of arrhythmia in CM cells consistent with chronic stimulation. "Negative" spikes are consistent with the cell firing again after the minimum refractory period, rather than the usual recovery period in a normal cardiac rhythm.

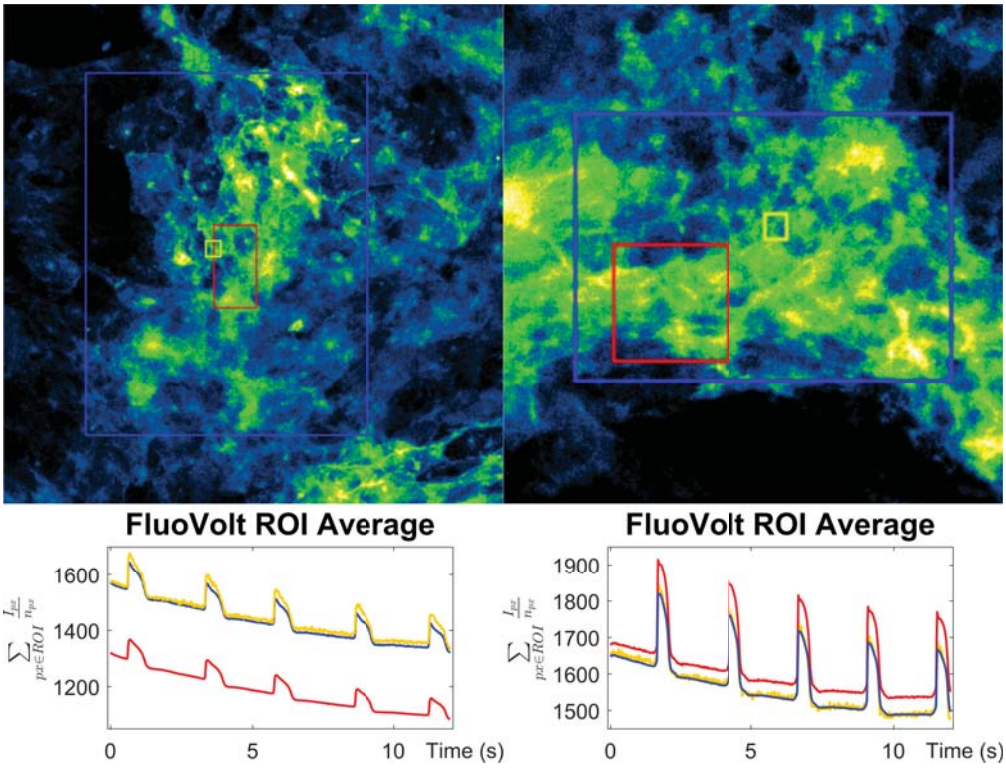

Figure 5.8: Voltage sensitive fluorescence dye measurements of cardiac action potentials in human embryonic stem cell derived cardiomyocytes (hESC CMs) for representative regions at three scales: subcellular (yellow), single to multiple cells (red) and tissue scale (blue). For each region, the corresponding color trace below represents the uncorrected average intensity (not the sum), or the sum of the intensity of all pixels in the region, $\sum_{px \in ROI} I_{px}(t)$, divided by the number of pixels (n_{px}).

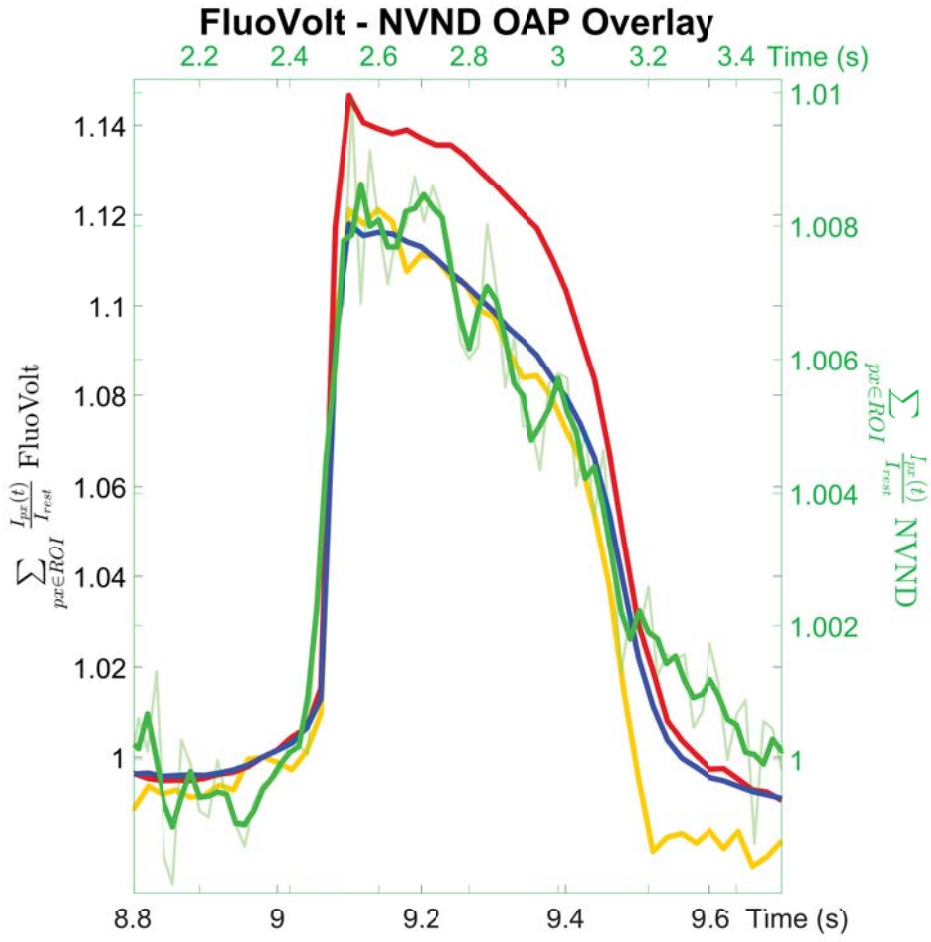

Figure 5.9: Optical detected action potential (OAP) measured via fluorescence from nitrogen vacancy centers in nanodiamonds (NVNDs) delivered to hESC CMs. Left Axis (black). Single optical action potential recorded with voltage sensitive (VS) dye across regions of increasing size: subcellular (yellow), single to several cell (red), synchronized clusters (blue). Regions are the same shown in 5.8B. Right Axis (green). Optical action potential from 40 nm diameter NVNDs 5 days after delivery to hESC CM overlaid with VS dye traces from 5.8B.

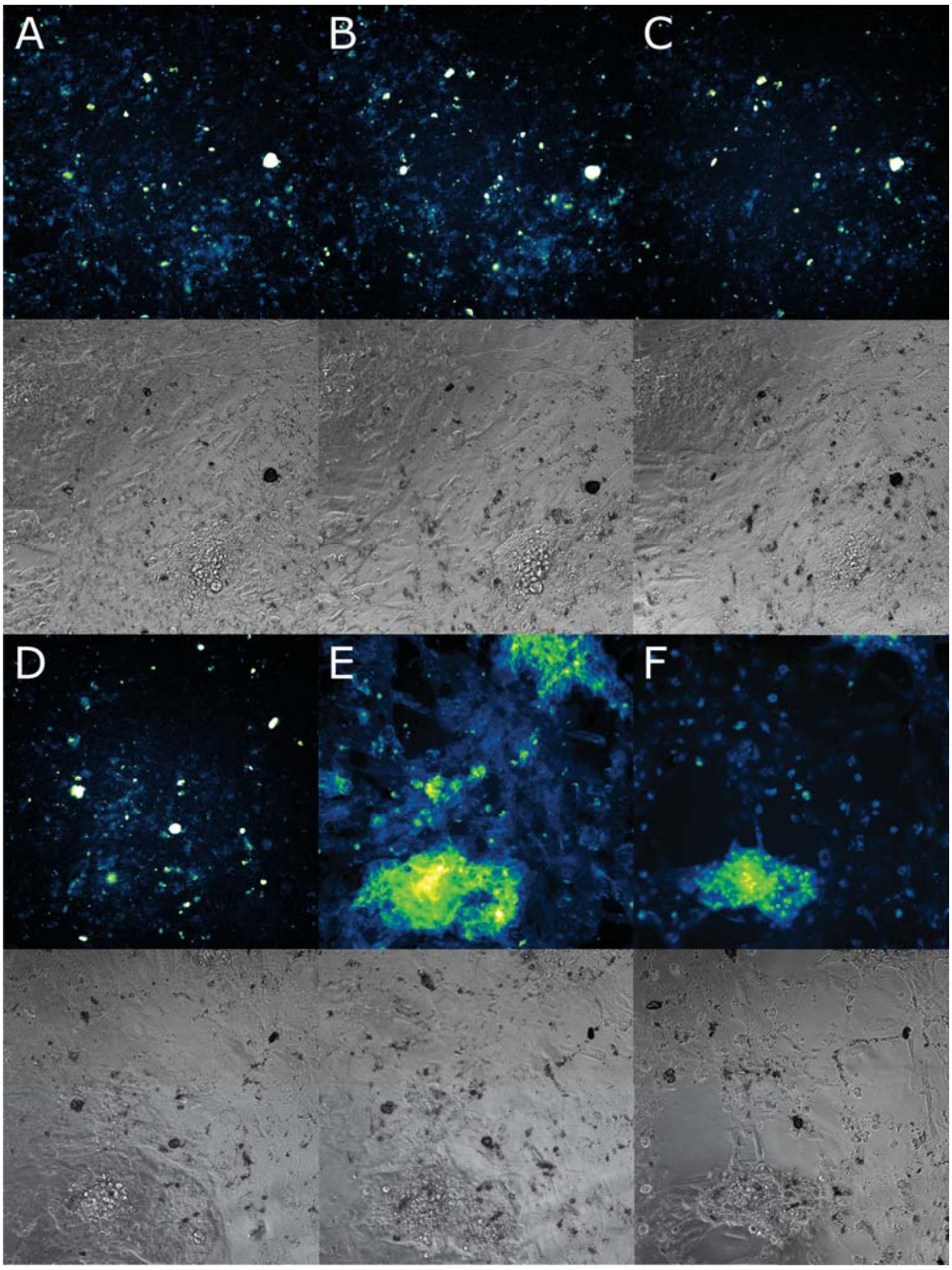

Figure 5.10: hESC CM cell culture and imaging over two weeks after delivery of 40 nm diameter nitrogen vacancy nanodiamonds (NVNDs) to cells. After 7 days imaging NVNDs using the Cy5 channel (A-D), voltage sensitive (VS) dye was added to obtain an optical action potential reference using the FITC channel. (A) 1 day. Cy5 (top), Phase (bottom). (B) 2 days. Cy5 (top), Phase (bottom). (C) 4 days. Cy5 (top), Phase (bottom). (D) 5 days. Cy5 (top), Phase (bottom). (E) 7 days. FITC (top), Phase (bottom). (F) 5 days. FITC (top), Phase (bottom).

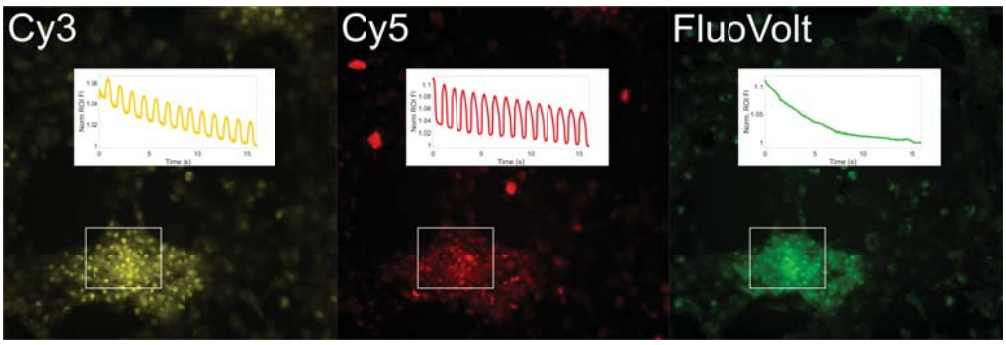

Figure 5.11: Cy5, Cy3 and FITC channel fluorescence images of hESC CM cell culture 14 day after delivery of NVNDs, 7 days after first VS dye staining. Re-stained prior to imaging. Inset traces show traces of beating (Cy5, Cy3) and non-beating (FluoVolt) hESC CMs after a few hours incubated with the VS dye.

CHAPTER 6

Conclusion

The development of magnetic resonance sensing and imaging to date has provided tremendous amounts of information that could not have been obtained through any other means. The trajectory of magnetic resonance technology development leads directly to the research efforts presented in this dissertation attempts to lay the ground work for extending this technology even further into the regime of functional biology at the nanoscale. Specifically, the introduction of a sensor capable of translating magnetic resonance information into optical microscopy and compatible with the most advanced forms of electron tomography will make it possible in the future to perform MRI on live cells with the resolution required to visualize functional information at the scale of individual protein or molecules. While these ultimate goals may still be far off, the work presented provides the tools necessary to collect magnetic resonance spectra from nanodiamonds targeted to specific macromolecular assemblies containing never before revealed functional dynamics, followed immediately by electron tomography to obtain not just the structure of the assembly, but also the structure of the unique microenvironment surrounding the sensor at the time of the last functional measurement. Refining this ideal experiment into a practical, reproducible methodology could present a new opportunity for core facilities at universities and research institutions that have already invested heavily in electron tomography to bring functional biological measurements down to the nanometer scale, approaching the structural level as a complement to the static structural information rapidly becoming available about biological macroassemblies.

References

[1] R. Schirhagl, K. Chang, M. Loretz, and C. L. Degen, "Nitrogen-vacancy centers in diamond: Nanoscale sensors for physics and biology," *Annual Review of Physical Chemistry*, vol. 65, pp. 83–105, 2014.

[2] W. contributors, "Rotating wave approximation - wikipedia, the free encyclopedia," 2018. [Online; accessed 10-Dec-2018].

[3] V. Acosta, E. Bauch, M. Ledbetter, A. Waxman, L.-S. Bouchard, and D. Budker, "Temperature dependence of the nitrogen-vacancy magnetic resonance in diamond," *Physical Review Letters*, vol. 104, no. 7, p. 070801, 2010.

[4] P. Alivisatos, "The use of nanocrystals in biological detection," *Nature Biotechnology*, vol. 22, no. 1, p. 47, 2004.

[5] H. C. Ishikawa-Ankerhold, R. Ankerhold, and G. P. Drummen, "Advanced fluorescence microscopy techniquesfrap, flip, flap, fret and flim," *Molecules*, vol. 17, no. 4, pp. 4047–4132, 2012.

[6] E. Abbe, "Contributions to the theory of the microscope and microscopic detection (translated from the german)," *Archiv fur Mikroskopische Anatomie*, vol. 9, pp. 413–418, 1873.

[7] S. W. Hell, "Far-field optical nanoscopy," *science*, vol. 316, no. 5828, pp. 1153–1158, 2007.

[8] T. J. Deerinck, "The application of fluorescent quantum dots to confocal, multiphoton, and electron microscopic imaging," *Toxicologic Pathology*, vol. 36, no. 1, pp. 112–116, 2008.

[9] S. A. Müller, U. Aebi, and A. Engel, "What transmission electron microscopes can visualize now and in the future," *Journal of Structural Biology*, vol. 163, no. 3, pp. 235–245, 2008.

[10] Y. Su, M. Nykanen, K. A. Jahn, R. Whan, L. Cantrill, L. L. Soon, K. R. Ratinac, and F. Braet, "Multi-dimensional correlative imaging of subcellular events: Combining the strengths of light and electron microscopy," *Biophysical Reviews*, vol. 2, no. 3, pp. 121–135, 2010.

[11] J. Robinson, T. Takizawa, and D. Vandre, "Applications of gold cluster compounds in immunocytochemistry and correlative microscopy: Comparison with colloidal gold," *Journal of Microscopy*, vol. 199, no. 3, pp. 163–179, 2000.

[12] A. Pombo, M. Hollinshead, and P. R. Cook, "Bridging the resolution gap: Imaging the same transcription factories in cryosections by light and electron microscopy," *Journal of Histochemistry & Cytochemistry*, vol. 47, no. 4, pp. 471–480, 1999.

[13] M. De Waele, "Silver-enhanced colloidal gold for the detection of leukocyte cell surface antigens in dark-field and epipolarization microscopy," in *Colloidal Gold, Volume 2*, pp. 443–467, Elsevier, 1989.

[14] R. Hardman, "A toxicologic review of quantum dots: Toxicity depends on physicochemical and environmental factors," *Environmental Health Perspectives*, vol. 114, no. 2, pp. 165–172, 2005.

[15] M. Nirmal, B. O. Dabbousi, M. G. Bawendi, J. Macklin, J. Trautman, T. Harris, and L. E. Brus, "Fluorescence intermittency in single cadmium selenide nanocrystals," *Nature*, vol. 383, no. 6603, p. 802, 1996.

[16] T. J. Deerinck, "The application of fluorescent quantum dots to confocal, multiphoton, and electron microscopic imaging," *Toxicologic Pathology*, vol. 36, no. 1, pp. 112–116, 2008.

[17] C.-C. Fu, H.-Y. Lee, K. Chen, T.-S. Lim, H.-Y. Wu, P.-K. Lin, P.-K. Wei, P.-H. Tsao, H.-C. Chang, and W. Fann, "Characterization and application of single fluorescent nanodiamonds as cellular biomarkers," *Proceedings of the National Academy of Sciences*, vol. 104, no. 3, pp. 727–732, 2007.

[18] L. McGuinness, Y. Yan, A. Stacey, D. Simpson, L. Hall, D. Maclaurin, S. Prawer, P. Mulvaney, J. Wrachtrup, F. Caruso, *et al.*, "Quantum measurement and orientation tracking of fluorescent nanodiamonds inside living cells," *Nature Nanotechnology*, vol. 6, no. 6, p. 358, 2011.

[19] L. M. Manus, D. J. Mastarone, E. A. Waters, X.-Q. Zhang, E. A. Schultz-Sikma, K. W. MacRenaris, D. Ho, and T. J. Meade, "Gd(iii)-nanodiamond conjugates for mri contrast enhancement," *Nano Letters*, vol. 10, no. 2, pp. 484–489, 2009.

[20] Z.-Y. Lien, T.-C. Hsu, K.-K. Liu, W.-S. Liao, K.-C. Hwang, and J.-I. Chao, "Cancer cell labeling and tracking using fluorescent and magnetic nanodiamond," *Biomaterials*, vol. 33, no. 26, pp. 6172–6185, 2012.

[21] E. K. Chow, X.-Q. Zhang, M. Chen, R. Lam, E. Robinson, H. Huang, D. Schaffer, E. Osawa, A. Goga, and D. Ho, "Nanodiamond therapeutic delivery agents mediate enhanced chemoresistant tumor treatment," *Science Translational Medicine*, vol. 3, no. 73, pp. 73ra21–73ra21, 2011.

[22] A. Alhaddad, M.-P. Adam, J. Botsoa, G. Dantelle, S. Perruchas, T. Gacoin, C. Mansuy, S. Lavielle, C. Malvy, F. Treussart, *et al.*, "Nanodiamond as a vector for sirna delivery to ewing sarcoma cells," *Small*, vol. 7, no. 21, pp. 3087–3095, 2011.

[23] D. Ho, "Beyond the sparkle: the impact of nanodiamonds as biolabeling and therapeutic agents," *ACS Nano*, vol. 3, no. 12, pp. 3825–3829, 2009.

[24] Y.-R. Chang, H.-Y. Lee, K. Chen, C.-C. Chang, D.-S. Tsai, C.-C. Fu, T.-S. Lim, Y.-K. Tzeng, C.-Y. Fang, C.-C. Han, *et al.*, "Mass production and dynamic imaging of fluorescent nanodiamonds," *Nature Nanotechnology*, vol. 3, no. 5, p. 284, 2008.

[25] G. Kucsko, P. Maurer, N. Y. Yao, M. Kubo, H. Noh, P. Lo, H. Park, and M. D. Lukin, "Nanometre-scale thermometry in a living cell," *Nature*, vol. 500, no. 7460, p. 54, 2013.

[26] F. Jelezko and J. Wrachtrup, "Single defect centres in diamond: A review," *Physica Status Solidi*, vol. 203, no. 13, pp. 3207–3225, 2006.

[27] M. Mkandawire, A. Pohl, T. Gubarevich, V. Lapina, D. Appelhans, G. Rodel, W. Pompe, J. Schreiber, and J. Opitz, "Selective targeting of green fluorescent nanodiamond conjugates to mitochondria in hela cells," *Journal of Biophotonics*, vol. 2, no. 10, pp. 596–606, 2009.

[28] M. Horie, L. K. Komaba, H. Kato, A. Nakamura, K. Yamamoto, S. Endoh, K. Fujita, S. Kinugasa, K. Mizuno, Y. Hagihara, *et al.*, "Evaluation of cellular influences induced by stable nanodiamond dispersion; the cellular influences of nanodiamond are small," *Diamond and Related Materials*, vol. 24, pp. 15–24, 2012.

[29] X. Zhang, W. Hu, J. Li, L. Tao, and Y. Wei, "A comparative study of cellular uptake and cytotoxicity of multi-walled carbon nanotubes, graphene oxide, and nanodiamond," *Toxicology Research*, vol. 1, no. 1, pp. 62–68, 2012.

[30] N. Mohan, C.-S. Chen, H.-H. Hsieh, Y.-C. Wu, and H.-C. Chang, "In vivo imaging and toxicity assessments of fluorescent nanodiamonds in caenorhabditis elegans," *Nano Letters*, vol. 10, no. 9, pp. 3692–3699, 2010.

[31] D. Studer, B. M. Humbel, and M. Chiquet, "Electron microscopy of high pressure frozen samples: Bridging the gap between cellular ultrastructure and atomic resolution," *Histochemistry and Dell Biology*, vol. 130, no. 5, pp. 877–889, 2008.

[32] Y.-K. Tzeng, O. Faklaris, B.-M. Chang, Y. Kuo, J.-H. Hsu, and H.-C. Chang, "Super-resolution imaging of albumin-conjugated fluorescent nanodiamonds in cells by stimulated emission depletion," *Angewandte Chemie International Edition*, vol. 50, no. 10, pp. 2262–2265, 2011.

[33] A. M. Schrand, J. J. Schlager, L. Dai, and S. M. Hussain, "Preparation of cells for assessing ultrastructural localization of nanoparticles with transmission electron microscopy," *Nature Protocols*, vol. 5, no. 4, p. 744, 2010.

[34] K.-K. Liu, C.-C. Wang, C.-L. Cheng, and J.-I. Chao, "Endocytic carboxylated nanodiamond for the labeling and tracking of cell division and differentiation in cancer and stem cells," *Biomaterials*, vol. 30, no. 26, pp. 4249–4259, 2009.

[35] A. M. Schrand, J. B. Lin, S. C. Hens, and S. M. Hussain, "Temporal and mechanistic tracking of cellular uptake dynamics with novel surface fluorophore-bound nanodiamonds," *Nanoscale*, vol. 3, no. 2, pp. 435–445, 2011.

[36] O. Faklaris, V. Joshi, T. Irinopoulou, P. Tauc, M. Sennour, H. Girard, C. Gesset, J.-C. Arnault, A. Thorel, J.-P. Boudou, *et al.*, "Photoluminescent diamond nanoparticles for cell labeling: Study of the uptake mechanism in mammalian cells," *ACS Nano*, vol. 3, no. 12, pp. 3955–3962, 2009.

[37] J. R. Lakowicz, I. Gryczynski, H. Malak, M. Schrader, P. Engelhardt, H. Kano, and S. W. Hell, "Time-resolved fluorescence spectroscopy and imaging of dna labeled with dapi and hoechst 33342 using three-photon excitation," *Biophysical Journal*, vol. 72, no. 2 Pt 1, p. 567, 1997.

[38] M. P. Lake and L.-S. Bouchard, "Targeted nanodiamonds for identification of subcellular protein assemblies in mammalian cells," *PloS one*, vol. 12, no. 6, p. e0179295, 2017.

[39] J. Mahamid, S. Pfeffer, M. Schaffer, E. Villa, R. Danev, L. K. Cuellar, F. Förster, A. A. Hyman, J. M. Plitzko, and W. Baumeister, "Visualizing the molecular sociology at the hela cell nuclear periphery," *Science*, vol. 351, no. 6276, pp. 969–972, 2016.

[40] S.-J. Yu, M.-W. Kang, H.-C. Chang, K.-M. Chen, and Y.-C. Yu, "Bright fluorescent nanodiamonds: No photobleaching and low cytotoxicity," *Journal of the American Chemical Society*, vol. 127, no. 50, pp. 17604–17605, 2005.

[41] F. Jelezko, C. Tietz, A. Gruber, I. Popa, A. Nizovtsev, S. Kilin, and J. Wrachtrup, "Spectroscopy of single n-v centers in diamond," *Single Molecules*, vol. 2, no. 4, pp. 255–260, 2001.

[42] V. V. Tuchin and V. Tuchin, "Tissue optics: Light scattering methods and instruments for medical diagnosis," 2015.

[43] G. Kucsko, P. Maurer, N. Y. Yao, M. Kubo, H. Noh, P. Lo, H. Park, and M. D. Lukin, "Nanometre-scale thermometry in a living cell," *Nature*, vol. 500, no. 7460, p. 54, 2013.

[44] D. Le Sage, K. Arai, D. Glenn, S. DeVience, L. Pham, L. Rahn-Lee, M. Lukin, A. Yacoby, A. Komeili, and R. Walsworth, "Optical magnetic imaging of living cells," *Nature*, vol. 496, no. 7446, p. 486, 2013.

[45] K. M. El-Say, "Nanodiamond as a drug delivery system: Applications and prospective," *J. Appl. Pharm. Sci*, vol. 1, no. 06, pp. 29–39, 2011.

[46] M. Chen, X.-Q. Zhang, H. B. Man, R. Lam, E. K. Chow, and D. Ho, "Nanodiamond vectors functionalized with polyethylenimine for sirna delivery," *The Journal of Physical Chemistry Letters*, vol. 1, no. 21, pp. 3167–3171, 2010.

[47] L. Moore, M. Gatica, H. Kim, E. Osawa, and D. Ho, "Multi-protein delivery by nanodiamonds promotes bone formation," *Journal of Dental Research*, vol. 92, no. 11, pp. 976–981, 2013.

[48] R. A. Shimkunas, E. Robinson, R. Lam, S. Lu, X. Xu, X.-Q. Zhang, H. Huang, E. Osawa, and D. Ho, "Nanodiamond–insulin complexes as ph-dependent protein delivery vehicles," *Biomaterials*, vol. 30, no. 29, pp. 5720–5728, 2009.

[49] G. Xi, E. Robinson, B. Mania-Farnell, E. F. Vanin, K.-W. Shim, T. Takao, E. V. Allender, C. S. Mayanil, M. B. Soares, D. Ho, *et al.*, "Convection-enhanced delivery of nanodiamond drug delivery platforms for intracranial tumor treatment," *Nanomedicine: Nanotechnology, Biology and Medicine*, vol. 10, no. 2, pp. 381–391, 2014.

[50] E. K. Chow, X.-Q. Zhang, M. Chen, R. Lam, E. Robinson, H. Huang, D. Schaffer, E. Osawa, A. Goga, and D. Ho, "Nanodiamond therapeutic delivery agents mediate enhanced chemoresistant tumor treatment," *Science Translational Medicine*, vol. 3, no. 73, pp. 73ra21–73ra21, 2011.

[51] V. Paget, J. Sergent, R. Grall, S. Altmeyer-Morel, H. Girard, T. Petit, C. Gesset, M. Mermoux, P. Bergonzo, J. Arnault, *et al.*, "Carboxylated nanodiamonds are neither cytotoxic nor genotoxic on liver, kidney, intestine and lung human cell lines," *Nanotoxicology*, vol. 8, no. sup1, pp. 46–56, 2014.

[52] G. Chatel, S. H. Desai, A. L. Mattheyses, M. A. Powers, and B. Fahrenkrog, "Domain topology of nucleoporin nup98 within the nuclear pore complex," *Journal of Structural Biology*, vol. 177, no. 1, pp. 81–89, 2012.

[53] T. M. Franks and M. W. Hetzer, "The role of nup98 in transcription regulation in healthy and diseased cells," *Trends in Cell Biology*, vol. 23, no. 3, pp. 112–117, 2013.

[54] S. Souquere, D. Weil, and G. Pierron, "Comparative ultrastructure of crm1-nucleolar bodies (cnobs), intranucleolar bodies (inbs) and hybrid pml/p62 bodies uncovers new facets of nuclear body dynamic and diversity," *Nucleus*, vol. 6, no. 4, pp. 326–338, 2015.

[55] O. Faklaris, V. Joshi, T. Irinopoulou, P. Tauc, M. Sennour, H. Girard, C. Gesset, J.-C. Arnault, A. Thorel, J.-P. Boudou, *et al.*, "Photoluminescent diamond nanoparticles for cell labeling: Study of the uptake mechanism in mammalian cells," *ACS Nano*, vol. 3, no. 12, pp. 3955–3962, 2009.

[56] M. Mkandawire, A. Pohl, T. Gubarevich, V. Lapina, D. Appelhans, G. Rodel, W. Pompe, J. Schreiber, and J. Opitz, "Selective targeting of green fluorescent nanodiamond conjugates to mitochondria in hela cells," *Journal of Biophotonics*, vol. 2, no. 10, pp. 596–606, 2009.

[57] O. Faklaris, V. Joshi, T. Irinopoulou, P. Tauc, M. Sennour, H. Girard, C. Gesset, J.-C. Arnault, A. Thorel, J.-P. Boudou, *et al.*, "Photoluminescent diamond nanoparticles for cell labeling: Study of the uptake mechanism in mammalian cells," *ACS Nano*, vol. 3, no. 12, pp. 3955–3962, 2009.

[58] S. Nagarajan, C. Pioche-Durieu, L. H. Tizei, C.-Y. Fang, J.-R. Bertrand, E. Le Cam, H.-C. Chang, F. Treussart, and M. Kociak, "Simultaneous cathodoluminescence and electron microscopy cytometry of cellular vesicles labeled with fluorescent nanodiamonds," *Nanoscale*, vol. 8, no. 22, pp. 11588–11594, 2016.

[59] M. A. Zurbuchen, M. P. Lake, S. A. Kohan, B. Leung, and L.-S. Bouchard, "Nanodiamond landmarks for subcellular multimodal optical and electron imaging," *Scientific Reports*, vol. 3, p. 2668, 2013.

[60] M. Mkandawire, A. Pohl, T. Gubarevich, V. Lapina, D. Appelhans, G. Rödel, W. Pompe, J. Schreiber, and J. Opitz, "Selective targeting of green fluorescent nanodiamond conjugates to mitochondria in hela cells," *Journal of Biophotonics*, vol. 2, no. 10, pp. 596–606, 2009.

[61] W. F. Scherer, J. T. Syverton, and G. O. Gey, "Studies on the propagation in vitro of poliomyelitis viruses: Iv. viral multiplication in a stable strain of human malignant epithelial cells (strain hela) derived from an epidermoid carcinoma of the cervix," *Journal of Experimental Medicine*, vol. 97, no. 5, pp. 695–710, 1953.

[62] F. De Chaumont, S. Dallongeville, N. Chenouard, N. Hervé, S. Pop, T. Provoost, V. Meas-Yedid, P. Pankajakshan, T. Lecomte, Y. Le Montagner, *et al.*, "Icy: An open bioimage informatics platform for extended reproducible research," *Nature Methods*, vol. 9, no. 7, p. 690, 2012.

[63] B. Ziemba, A. Janaszewska, K. Ciepluch, M. Krotewicz, W. A. Fogel, D. Appelhans, B. Voit, M. Bryszewska, and B. Klajnert, "In vivo toxicity of poly(propyleneimine) dendrimers," *Journal of Biomedical Materials Research Part A*, vol. 99, no. 2, pp. 261–268, 2011.

[64] B. Klajnert, D. Appelhans, H. Komber, N. Morgner, S. Schwarz, S. Richter, B. Brutschy, M. Ionov, A. K. Tonkikh, M. Bryszewska, *et al.*, "The influence of densely organized maltose shells on the biological properties of poly(propylene imine) dendrimers: New effects dependent on hydrogen bonding," *Chemistry–A European Journal*, vol. 14, no. 23, pp. 7030–7041, 2008.

[65] A. von Appen, J. Kosinski, L. Sparks, A. Ori, A. L. DiGuilio, B. Vollmer, M.-T. Mackmull, N. Banterle, L. Parca, P. Kastritis, *et al.*, "In situ structural analysis of the human nuclear pore complex," *Nature*, vol. 526, no. 7571, p. 140, 2015.

[66] M. A. Zurbuchen, M. P. Lake, S. A. Kohan, B. Leung, and L.-S. Bouchard, "Nanodiamond landmarks for subcellular multimodal optical and electron imaging," *Scientific Reports*, vol. 3, p. 2668, 2013.

[67] W.-K. Shiue and L. J. Bain, "Experiment size and power comparisons for two-sample poisson tests," *Applied Statistics*, pp. 130–134, 1982.

[68] Y.-J. Gu, J. Cheng, C.-C. Lin, Y. W. Lam, S. H. Cheng, and W.-T. Wong, "Nuclear penetration of surface functionalized gold nanoparticles," *Toxicology and Applied Pharmacology*, vol. 237, no. 2, pp. 196–204, 2009.

[69] M. Thomas and A. M. Klibanov, "Conjugation to gold nanoparticles enhances polyethylenimine's transfer of plasmid dna into mammalian cells," *Proceedings of the National Academy of Sciences*, vol. 100, no. 16, pp. 9138–9143, 2003.

[70] M. Chen and A. von Mikecz, "Formation of nucleoplasmic protein aggregates impairs nuclear function in response to sio2 nanoparticles," *Experimental Cell Research*, vol. 305, no. 1, pp. 51–62, 2005.

[71] E. Abbe, "On the estimation of aperture in the microscope.," *Journal of the Royal Microscopical Society*, vol. 1, no. 3, pp. 388–423, 1881.

[72] Y.-K. Tzeng, O. Faklaris, B.-M. Chang, Y. Kuo, J.-H. Hsu, and H.-C. Chang, "Super-resolution imaging of albumin-conjugated fluorescent nanodiamonds in cells by stimulated emission depletion," *Angewandte Chemie International Edition*, vol. 50, no. 10, pp. 2262–2265, 2011.

[73] B. Rothen-Rutishauser, D. A. Kuhn, Z. Ali, M. Gasser, F. Amin, W. J. Parak, D. Vanhecke, A. Fink, P. Gehr, and C. Brandenberger, "Quantification of gold nanoparticle cell uptake under controlled biological conditions and adequate resolution," *Nanomedicine*, vol. 9, no. 5, pp. 607–621, 2014.

[74] E. R. Griffis, S. Xu, and M. A. Powers, "Nup98 localizes to both nuclear and cytoplasmic sides of the nuclear pore and binds to two distinct nucleoporin subcomplexes," *Molecular Biology of the Cell*, vol. 14, no. 2, pp. 600–610, 2003.

[75] T. M. Mayhew, C. Mühlfeld, D. Vanhecke, and M. Ochs, "A review of recent methods for efficiently quantifying immunogold and other nanoparticles using tem sections through cells, tissues and organs," *Annals of Anatomy-Anatomischer Anzeiger*, vol. 191, no. 2, pp. 153–170, 2009.

[76] T. M. Mayhew, "Mapping the distributions and quantifying the labelling intensities of cell compartments by immunoelectron microscopy: Progress towards a coherent set of methods," *Journal of Anatomy*, vol. 219, no. 6, pp. 647–660, 2011.

[77] A. M. Derfus, W. C. Chan, and S. N. Bhatia, "Probing the cytotoxicity of semiconductor quantum dots," *Nano Letters*, vol. 4, no. 1, pp. 11–18, 2004.

[78] E. Oh, R. Liu, A. Nel, K. B. Gemill, M. Bilal, Y. Cohen, and I. L. Medintz, "Meta-analysis of cellular toxicity for cadmium-containing quantum dots," *Nature Nanotechnology*, vol. 11, no. 5, p. 479, 2016.

[79] P. Frantsuzov, M. Kuno, B. Janko, and R. A. Marcus, "Universal emission intermittency in quantum dots, nanorods and nanowires," *Nature Physics*, vol. 4, no. 7, p. 519, 2008.

[80] T. J. Deerinck, "The application of fluorescent quantum dots to confocal, multiphoton, and electron microscopic imaging," *Toxicologic Pathology*, vol. 36, no. 1, pp. 112–116, 2008.

[81] S. Guo and L. Huang, "Nanoparticles escaping res and endosome: Challenges for sirna delivery for cancer therapy," *Journal of Nanomaterials*, vol. 2011, p. 11, 2011.

[82] R. Levy, U. Shaheen, Y. Cesbron, and V. See, "Gold nanoparticles delivery in mammalian live cells: A critical review," *Nano Reviews*, vol. 1, no. 1, p. 4889, 2010.

[83] S. Thiberge, A. Nechushtan, D. Sprinzak, O. Gileadi, V. Behar, O. Zik, Y. Chowers, S. Michaeli, J. Schlessinger, and E. Moses, "Scanning electron microscopy of cells and tissues under fully hydrated conditions," *Proceedings of the National Academy of Sciences*, vol. 101, no. 10, pp. 3346–3351, 2004.

[84] S. J. Soenen, B. Manshian, J. M. Montenegro, F. Amin, B. Meermann, T. Thiron, M. Cornelissen, F. Vanhaecke, S. Doak, W. J. Parak, *et al.*, "Cytotoxic effects of gold nanoparticles: A multiparametric study," *ACS Nano*, vol. 6, no. 7, pp. 5767–5783, 2012.

[85] D. Zhang, O. Neumann, H. Wang, V. M. Yuwono, A. Barhoumi, M. Perham, J. D. Hartgerink, P. Wittung-Stafshede, and N. J. Halas, "Gold nanoparticles can induce the formation of protein-based aggregates at physiological ph," *Nano Letters*, vol. 9, no. 2, pp. 666–671, 2009.

[86] W. G. Kreyling, A. M. Abdelmonem, Z. Ali, F. Alves, M. Geiser, N. Haberl, R. Hartmann, S. Hirn, D. J. De Aberasturi, K. Kantner, *et al.*, "In vivo integrity of polymer-coated gold nanoparticles," *Nature Nanotechnology*, vol. 10, no. 7, p. 619, 2015.

[87] A. Ivask, T. Titma, M. Visnapuu, H. Vija, A. Kakinen, M. Sihtmae, S. Pokhrel, L. Madler, M. Heinlaan, V. Kisand, *et al.*, "Toxicity of 11 metal oxide nanoparticles to three mammalian cell types in vitro," *Current Topics in Medicinal Chemistry*, vol. 15, no. 18, pp. 1914–1929, 2015.

[88] C. J. Wingard, D. M. Walters, B. L. Cathey, S. C. Hilderbrand, P. Katwa, S. Lin, P. C. Ke, R. Podila, A. Rao, R. M. Lust, *et al.*, "Mast cells contribute to altered vascular reactivity and ischemia-reperfusion injury following cerium oxide nanoparticle instillation," *Nanotoxicology*, vol. 5, no. 4, pp. 531–545, 2011.

[89] W. Buchser, M. Collins, T. Garyantes, R. Guha, S. Haney, V. Lemmon, Z. Li, and O. J. Trask, "Assay development guidelines for image-based high content screening, high content analysis and high content imaging," 2014.

[90] K. R. Rodgers and R. C. Chou, "Therapeutic monoclonal antibodies and derivatives: Historical perspectives and future directions," *Biotechnology Advances*, vol. 34, no. 6, pp. 1149–1158, 2016.

[91] B. Ziemba, I. Franiak-Pietryga, M. Pion, D. Appelhans, M. A. Munoz-Fernandez, B. Voit, M. Bryszewska, and B. Klajnert-Maculewicz, "Toxicity and proapoptotic activity of poly(propylene imine) glycodendrimers in vitro: Considering their contrary potential as biocompatible entity and drug molecule in cancer," *International Journal of Pharmaceutics*, vol. 461, no. 1-2, pp. 391–402, 2014.

[92] I. Franiak-Pietryga, E. Ziolkowska, B. Ziemba, D. Appelhans, B. Voit, M. Szewczyk, J. Goora-Tybor, T. Robak, B. Klajnert, and M. Bryszewska, "The influence of maltotriose-modified poly(propylene imine) dendrimers on the chronic lymphocytic leukemia cells in vitro: Dense shell g4 ppi," *Molecular Pharmaceutics*, vol. 10, no. 6, pp. 2490–2501, 2013.

[93] Y.-A. Huang, C.-W. Kao, K.-K. Liu, H.-S. Huang, M.-H. Chiang, C.-R. Soo, H.-C. Chang, T.-W. Chiu, J.-I. Chao, and E. Hwang, "The effect of fluorescent nanodiamonds on neuronal survival and morphogenesis," *Scientific Reports*, vol. 4, p. 6919, 2014.

[94] M. Barok, H. Joensuu, and J. Isola, "Trastuzumab emtansine: Mechanisms of action and drug resistance," *Breast Cancer Research*, vol. 16, no. 2, p. 209, 2014.

[95] B. Grotz, M. V. Hauf, M. Dankerl, B. Naydenov, S. Pezzagna, J. Meijer, F. Jelezko, J. Wrachtrup, M. Stutzmann, F. Reinhard, *et al.*, "Charge state manipulation of qubits in diamond," *Nature communications*, vol. 3, p. 729, 2012.

[96] S. Karaveli, O. Gaathon, A. Wolcott, R. Sakakibara, O. A. Shemesh, D. S. Peterka, E. S. Boyden, J. S. Owen, R. Yuste, and D. Englund, "Modulation of nitrogen vacancy charge state and fluorescence in nanodiamonds using electrochemical potential," *Proceedings of the National Academy of Sciences*, vol. 113, no. 15, pp. 3938–3943, 2016.

[97] N. Aslam, G. Waldherr, P. Neumann, F. Jelezko, and J. Wrachtrup, "Photo-induced ionization dynamics of the nitrogen vacancy defect in diamond investigated by single-shot charge state detection," *New Journal of Physics*, vol. 15, no. 1, p. 013064, 2013.

[98] M. Pfender, N. Aslam, P. Simon, D. Antonov, G. Thiering, S. Burk, F. Favaro de Oliveira, A. Denisenko, H. Fedder, J. Meijer, *et al.*, "Protecting a diamond quantum memory by charge state control," *Nano letters*, vol. 17, no. 10, pp. 5931–5937, 2017.

[99] S. Bedut, C. Seminatore-Nole, V. Lamamy, S. Caignard, J. A. Boutin, O. Nosjean, J.-P. Stephan, and F. Coge, "High-throughput drug profiling with voltage-and calcium-sensitive fluorescent probes in human ipsc-derived cardiomyocytes," *American Journal of Physiology-Heart and Circulatory Physiology*, vol. 311, no. 1, pp. H44–H53, 2016.

[100] A. Arshi, Y. Nakashima, H. Nakano, S. Eaimkhong, D. Evseenko, J. Reed, A. Z. Stieg, J. K. Gimzewski, and A. Nakano, "Rigid microenvironments promote cardiac differentiation of mouse and human embryonic stem cells," *Science and technology of advanced materials*, vol. 14, no. 2, p. 025003, 2013.

[101] H. Nakano, I. Minami, D. Braas, H. Pappoe, X. Wu, A. Sagadevan, L. Vergnes, K. Fu, M. Morselli, C. Dunham, *et al.*, "Glucose inhibits cardiac muscle maturation through nucleotide biosynthesis," *Elife*, vol. 6, p. e29330, 2017.

[102] M. Börsch, R. Reuter, G. Balasubramanian, R. Erdmann, F. Jelezko, and J. Wrachtrup, "Fluorescent nanodiamonds for fret-based monitoring of a single biological nanomotor f o f 1-atp synthase," in *Multiphoton Microscopy in the Biomedical Sciences IX*, vol. 7183, p. 71832N, International Society for Optics and Photonics, 2009.

[103] A. Ahola, A. L. Kiviaho, K. Larsson, M. Honkanen, K. Aalto-Setälä, and J. Hyttinen, "Video image-based analysis of single human induced pluripotent stem cell derived cardiomyocyte beating dynamics using digital image correlation," *Biomedical engineering online*, vol. 13, no. 1, p. 39, 2014.

[104] L. Hacquebard and L. Childress, "Charge-state dynamics during excitation and depletion of the nitrogen-vacancy center in diamond," *Physical Review A*, vol. 97, no. 6, p. 063408, 2018.

[105] J. Chen, S. Lourette, K. Rezai, T. Hoelzer, M. Lake, M. Nesladek, L.-S. Bouchard, P. Hemmer, and D. Budker, "Optical quenching and recovery of photoconductivity in single-crystal diamond," *Applied Physics Letters*, vol. 110, no. 1, p. 011108, 2017.

[106] H. Jayakumar, S. Dhomkar, J. Henshaw, and C. A. Meriles, "Spin readout via spin-to-charge conversion in bulk diamond nitrogen-vacancy ensembles," *Applied Physics Letters*, vol. 113, no. 12, p. 122404, 2018.

[107] B. J. Shields, Q. Unterreithmeier, N. De Leon, H. Park, and M. D. Lukin, "Efficient readout of a single spin state in diamond via spin-to-charge conversion," *Physical review letters*, vol. 114, no. 13, p. 136402, 2015.

[108] S. Dhomkar, J. Henshaw, H. Jayakumar, and C. A. Meriles, "Long-term data storage in diamond," *Science advances*, vol. 2, no. 10, p. e1600911, 2016.